DENSIFICATION BEHAVIOR, NANOCRYSTALLIZATION, AND MECHANICAL PROPERTIES OF SPARK PLASMA SINTERED Fe-BASED BULK AMORPHOUS ALLOYS

By

ASHISH KUMAR SINGH

Bachelor of Science in Mechanical Engineering
Osmania University, College of Engineering
Hyderabad, Andhra Pradesh, India
2007

Master of Science in Mechanical Engineering
Oklahoma State University, Stillwater, Oklahoma
2010

Submitted to the Faculty of the
Graduate College of the
Oklahoma State University
in partial fulfillment of
the requirements for
the Degree of
DOCTOR OF PHILOSOPHY
July, 2014

DENSIFICATION BEHAVIOR, NANOCRYSTALLIZATION, AND MECHANICAL PROPERTIES OF SPARK PLASMA SINTERED Fe-BASED BULK AMORPHOUS ALLOYS

Dissertation Approved:

Dr. Sandip P. Harimkar

Dissertation Adviser

Dr. Jay C. Hanan

Dr. Raman P. Singh

Dr. Ranji Vaidyanathan

ACKNOWLEDGEMENTS

I would like to thank my advisor Dr. Sandip Harimkar, who has given me focused career objectives. He has always motivated me by providing both good challenges and opportunities. I also want to thank Dr. Raman Singh, Dr. Jay Hanan, and Dr. Ranji Vaidyanathan for being in my committee and giving their valuable advises throughout my research work. I am thankful to Dr. Jim Puckette who has allowed me to use his lab equipment for my research. I would also like to thank Dr. Narendra Dahotre for helping me performing DSC and TEM experiments. I would also like to thank Dr. Ken Littrell and Dr. Jinkui Zhao for helping me perform small angle neutron scattering experiments. I am grateful to Dr. Jan Ilavsky for guiding me through his wonderful software Irena and SANS analysis. I would like to thank National Science Foundation for partially funding this project. I would also like to acknowledge the financial support from EPSCoR neutron travel fellowship for performing experiments at Oak Ridge National Laboratory (ORNL). I would like to thank my father Ravinder Singh and my mom Munni Devi for being wonderful parents and my brother Manish who is always caring and supporting. I thank my lovely wife Pooja Singh for always encouraging and supporting me. I would also like to acknowledge my amazing friends Vineet Yadav and Glory Shrivastava, and little sister Sudha Sikha who have always added more fun to my life. I would also like to thank friends and colleagues Sudheer Bandla, Arif Rahman, Balaji Jaykumar, and Sree Harsha who were always there with all their support. I would like to thank Habib Alavi and Shravan Katakam who always helped me whenever I fell short. I would like to thank all my family members, friends, colleagues, and professors who always helped me in achieving my goal.

Name: ASHISH KUMAR SINGH

Date of Degree: JULY, 2014

Title of Study: DENSIFICATION BEHAVIOR, NANOCRYSTALLIZATION, AND MECHANICAL PROPERTIES OF SPARK PLASMA SINTERED Fe-BASED BULK AMORPHOUS ALLOYS

Major Field: MECHANICAL AND AEROSPACE ENGINEERING

Abstract: Fe-based amorphous alloys are gaining increasing attention due to their exceptional wear and corrosion resistance for potential structural applications. Two major challenges that are hindering the commercialization of these amorphous alloys are difficulty in processing of bulk shapes (diameter > 10 mm) and lack of ductility. Spark plasma sintering (SPS) is evolving as a promising technique for processing bulk shapes of amorphous and nanocrystalline materials. The objective of this work is to investigate densification behavior, nanocrystallization, and mechanical properties of SPS sintered Fe-based amorphous alloys of composition $Fe_{48}Cr_{15}Mo_{14}Y_2C_{15}B_6$.

SPS processing was performed in three distinct temperature ranges of amorphous alloys: (a) below glass transition temperature (T_g), (b) between T_g and crystallization temperature (T_x), and (c) above T_x. Punch displacement data obtained during SPS sintering was correlated with the SPS processing parameters such as temperature, pressure, and sintering time. Powder rearrangement, plastic deformation below T_g, and viscous flow of the material between T_g and T_x were observed as the main densification stages during SPS sintering. Micro-scale temperature distributions at the point of contact and macro-scale temperature distribution throughout the sample during SPS of amorphous alloys were modeled. The bulk amorphous alloys are expected to undergo structural relaxation and nanocrystallization during SPS sintering. X-ray diffraction (XRD), small angle neutron scattering (SANS), and transmission electron microscopy (TEM) was performed to investigate the evolution of nanocrystallites in SPS sintered Fe-based bulk amorphous alloys. The SANS analysis showed significant scattering for the samples sintered in the supercooled region indicating local structural and compositional changes with the profuse nucleation of nano-clusters (~4 nm).

Compression tests and microhardness were performed on the samples sintered at different temperatures ranging from 570 °C to 800 °C. Maximum compression strength (1.1±0.2 MPa) was obtained for the samples sintered in the supercooled region. Effects of crystallization on tribological behavior of sintered samples were also investigated where crystallization resulted in increase in wear resistance. Laser surface hardening of SPS sintered amorphous samples were performed. Depending on the processing parameters, the laser surface irradiation causes structural relaxation and nanocrystallization, resulting in surface hardening.

TABLE OF CONTENTS

List of Figures

List of Tables

CHAPTER I

INTRODUCTION

1.1 Introduction

Amorphous alloys or bulk metallic glasses (BMGs) have potential for use in high-strength structural applications due to properties, such as high hardness, elastic modulus/limit, and corrosion and wear resistance. These materials are formed by solidifying the liquid melt at high cooling rates (up to 10^6 K/s) to inhibit the nucleation of grains [1]. During solidification, the undercooled liquid becomes more viscous and finally solidifies into a structurally arrested amorphous state with a decrease in temperature. The first metallic glass, with the composition $Au_{75}Si_{25}$, was formed by Duwez *et al.* at Caltech, USA in 1960 [2]. This invention led to the use of melt quenching for the processing of metallic glasses of several compositions. Metallic glass ribbons and powders of various compositions were successfully processed using melt spinning and gas atomization techniques, respectively. Two major limitations that have inhibited the use of metallic glasses as structural materials are difficulty in processing bulk samples (diameter >10 mm) and lack of general ductility [3-5].

1.2 Processing of bulk amorphous alloys and composites

Inoue *et al.* proposed three empirical rules that, when followed, result in multicomponent amorphous structure at slow cooling rates [6]. These rules are: (1) alloy systems must contain at least three elements, (2) the differences in atomic sizes among the three main components must be greater than 12%, and (3) there must be a high negative heat of mixing of the main three elements. These rules led to the development of different multi-component alloy systems that retain amorphous structure even when solidification takes place at relatively slow cooling rates (0.1 K/s-100 K/s). Fig.1.1 shows the time-temperature-transformation (TTT) curves for bulk amorphous alloys and conventional metallic glasses. The onset time for crystallization of conventional metallic glasses is of the order 10^{-4}-10^{-3} s at the nose of the TTT curve, whereas for bulk metallic glasses it increases to about 10^{2}-10^{3} s. A few examples of multicomponent amorphous alloy systems recently developed are ZrTiCuNiBe, LaAlNi, FeAlGaPCB, and NbFeCoAl [1]. These bulk amorphous alloys have high glass forming ability and wide supercooled regions, leading to large temperature ranges for the processing. An alloy with the composition $(Zr_{82.5}Ti_{17.5})_{55}(Ni_{54}Cu_{46})_{18.75}Be_{26.25}$ has one of the widest reported supercooled regions of 135 K[7].

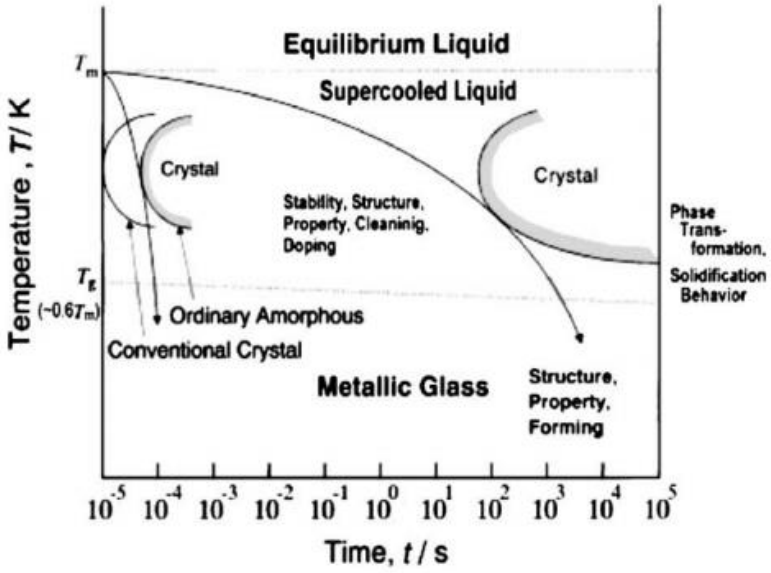

Fig.1.1 TTT diagram showing the high stability of the BMG forming supercooled liquid over several thousands of seconds [1].

Amorphous alloys can be processed using different techniques as classified in Fig.1.2 [1]. Amorphous alloys can be processed in the form of powders or ribbons using gas atomization and melt spinning, respectively. Gas atomization techniques such as centrifugal atomization, gas-water atomization, roller atomization, and water atomization have been used in the production of amorphous alloy powders [8-10]. A few examples of amorphous powders processed using these techniques are Fe-Si-B, Fe-P-C, Co-Si-B, Ni-Si-B, Ni-P-B, and Al-Y-Ni [11]. Melt spinning is also widely used to process metallic glass ribbons where the thicknesses of the ribbons are limited to ~50 μm [12-14]. A few amorphous alloy compositions have lower critical cooling rates (< 10 K/s), and they can be cast using conventional casting techniques such as direct casting and suction casting. An example of one such alloy composition is $Zr_{41}Ti_{14}Cu_{12.5}Ni_{10}Be_{22.5}$, which has a critical cooling rate of 0.1 K/s [1].

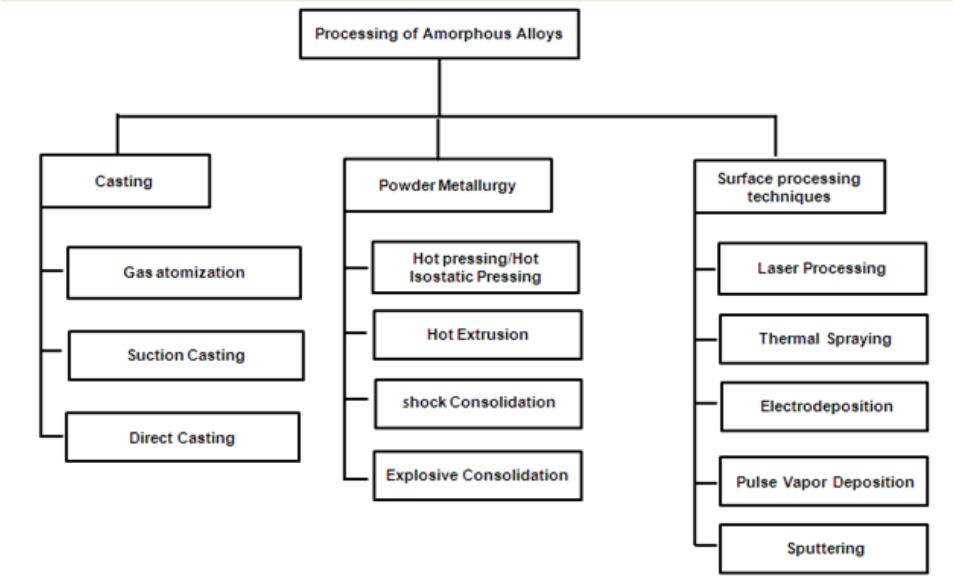

Fig.1.2 Schematic showing different approaches for processing amorphous alloy powders, ribbons, bulk shapes, and coatings.

1.2.1 Powder metallurgical processing

An alternative approach for the processing bulk amorphous alloys is through solid state sintering, where powders or ribbons of amorphous alloys are consolidated in bulk shapes such that the amorphous nature is retained. Several processing methods such as hot pressing (HP), hot isostatic pressing (HIP), hot extrusion, and spark plasma sintering (SPS) have been investigated for the processing of bulk amorphous alloys [15, 16]. Recently, efforts have been made to sinter Fe-based amorphous powder by conventional HP [17, 18]. Fig.1.3 shows a typical cross-sectional view of Fe-based amorphous materials sintered using HP in the temperature range of 440 °C with a pressure of 1.25 GPa. In this investigation, high pressure and glassy binders (phosphate glass) were required to obtain high densification. The processing of amorphous alloys using HP often results in crystallization and low relative density of the sintered compacts [17]. With such

limitations, these conventional processes are not optimal for the processing of Fe-based bulk amorphous alloys.

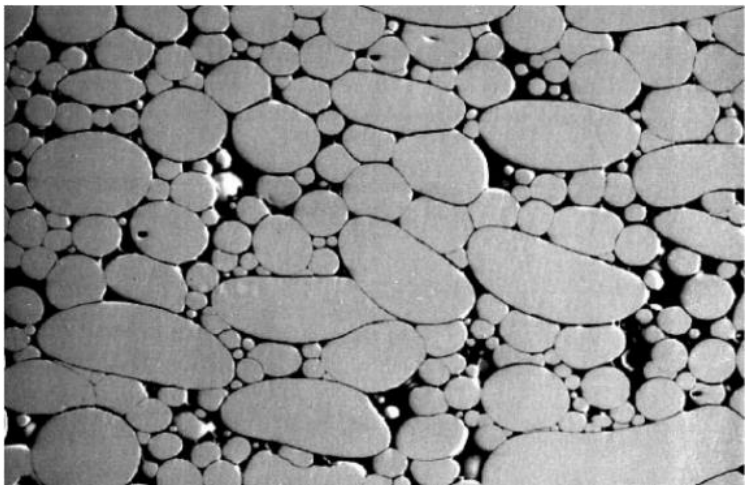

Fig.1.3 A cross-sectional view of hot pressed Fe-based amorphous alloy[17].

1.2.2 Spark plasma sintering (SPS)

SPS is a novel processing technique in which pulsed direct current and uniaxial pressure are applied simultaneously for the processing dense nanostructured and amorphous materials. The schematic of an SPS set up is shown in Fig 1.4 (a). SPS processing has many advantages compared to conventional casting and to other conventional sintering techniques. SPS capabilities allow high heating rates (up to 600 ºC/min.), short sintering times (less than 30 min.), and sintering done at lower temperatures (100-200 ºC less) compared to conventional techniques such as HP and HIP [19-21]. The mechanism of SPS involves a sequence of steps in which sintering starts with surface activation and rearrangement of powder. The activation is achieved by the passage of a direct current on the surface of the powders to remove surface oxide layers and other impurities; passage of the current favors the joining of particles by necking due

to diffusion and plastic deformation. Thereafter, current flows through the formed neck and generates heat due to the Joule effect as shown in Fig. 1.4 (b). The effect of pressure is optimum during neck formation and lead to densification.

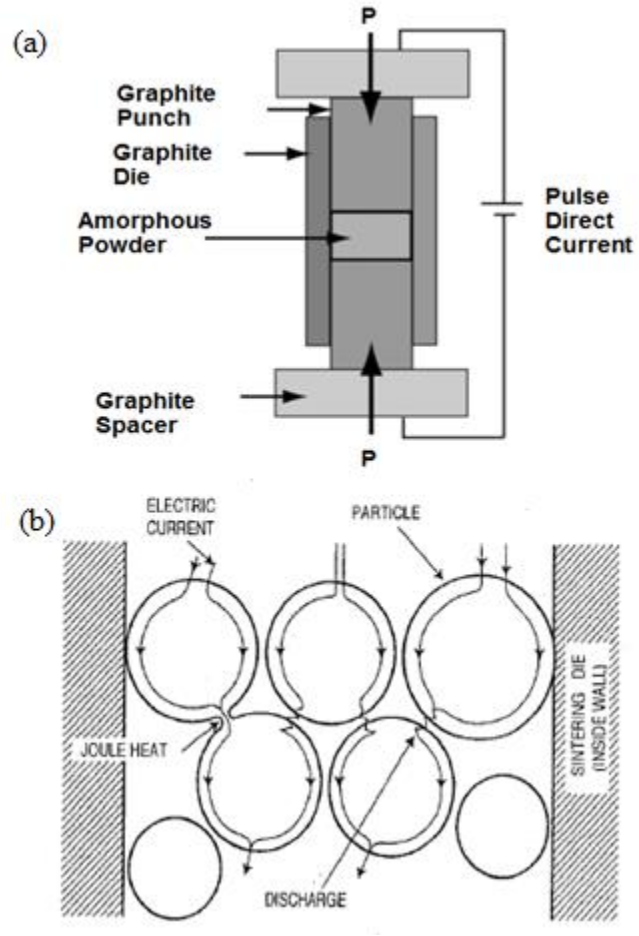

Fig.1.4 a) SPS setup for processing of bulk amorphous alloys, and b) current flowing through powder particles [22].

As the current passes through the surface of the powder, localized overheating may occur at particle contacts. The localized overheating results in localized melting and may enhance diffusion and promote strong inter-particle bonding on the surface and at the points of contact between the two particles. During this process, a steep temperature gradient is generated along the radius of the particle leaving the inner core of the powder

unaffected [21, 23, 24]. The role of direct current during sintering of amorphous alloys is still under investigation. Hulbert *et al.* demonstrated that plasma is not present during sintering using *in situ* atomic emission spectroscopy and ultrafast *in situ* voltage measurement. These experiments were performed on various types of powders, and the absence of spark was confirmed on all types of particles [25].

One of the challenges in SPS processing is the difficulty in measurement of the actual sample temperature during sintering. Typically, the temperature is measured by placing a thermocouple in the wall of the dies or in the punch. This leads to a difference between the sample temperature and measured temperature at the center of the die. The difference in temperature depends on thermo-physical properties, such as electrical and thermal conductivities of the sample and the die, and on the punch setup used during experiments. Temperature gradients also exist across the radial and axial directions of the samples, and these influence the uniformity of the properties of the sintered samples. Considering these experimental issues, computational efforts have been made to estimate the temperature gradient of die, punches, and the sample during SPS processing [26, 27]. Molenat *et al.* compared the measured temperature gradient at different radial positions of the die during SPS experiments to that of the temperatures obtained through computational methods. The computed temperature difference between the external wall of the die and sample was found to be 100 ºC. During sintering, the temperature difference is lower at lower temperatures than at higher temperatures [28, 29]. Investigating temperature distribution during SPS processing of amorphous alloys is necessary in order to facilitate design processing for fully dense amorphous or amorphous-nanocrystalline composite with controlled crystallization.

1.2.3 SPS of bulk amorphous alloys and composites

Recently, investigations were made on SPS of amorphous alloys and its composites. In order to retain the amorphous structure, it is essential to sinter the amorphous powder well below the crystallization temperature (T_x). Many investigations into SPS processing involve usage of tungsten carbide (WC) tooling; WC is extremely brittle, and therefore, unreliable and uneconomical when compared to graphite tooling [30, 31]. In most of the investigations involving SPS of bulk amorphous alloys and composites, processing parameters such as temperature, pressure, and sintering time were optimized to obtain dense samples and improved mechanical properties. This section reviews the processing conditions and various characterizations performed on SPS of amorphous alloys.

Kim *et al*. examined SPS of $Cu_{54}Ni_6Zr_{22}Ti_{18}$ amorphous alloy powder [30, 31]. Samples were processed at 743 K for 60 s using a uniaxial pressure of 280 MPa. A disc of 20 mm diameter and 5 mm thickness was obtained, and x-ray diffraction (XRD) confirmed the amorphous nature of the processed bulk amorphous alloys. The thermal stability of the sintered sample decreased compared to that of the initial powder due to partial devitrification of the amorphous alloy during sintering as demonstrated using differential scanning calorimetry (DSC). Kim *et al*. also investigated the dependency of hardness and compressive strength on particle size. A decrease in particle size of amorphous alloys resulted in better densification and an increase in glass forming ability of amorphous alloys; both improve the mechanical strength of the alloy. SPS of Mg-based amorphous alloys $Mg_{55}Cu_{30}Y_{15}$ and $Mg_{55}Cu_{30}Gd_{15}$ resulted in a fully dense bulk amorphous alloy. An SEM micrograph of indentation reveals pile ups and shear bands

indicating the characteristics of amorphous alloys. The lack of cracks indicate a high fracture toughness of sintered BMG; however, the effect of density on microhardness and fracture toughness was not evaluated [31, 32].

High pressure (500 MPa) SPS sintering of $Ti_{50}Cu_{23}Ni_{20}Sn_7$ amorphous powder was investigated by Li *et al.* [33]. Sintering was performed for a short time (1 min.) at a temperature of 763 K, between the glass transition temperature (T_g) and the crystallization temperature (T_x). The compressive strength of the sintered sample was low compared to the bulk amorphous alloy processed using the arc melting technique with the same composition. The low compressive strength was due to sintering defects such as porosities and high thermal residual stresses.

The microstructure and mechanical properties of Cu-based amorphous alloy was investigated by Kim *et al.* A 6% decrease in the compressive strength of SPS sintered samples compared to casted specimens was reported [34]. This reduction in compressive strength was due to the presence of pores, defects, and oxides. Porous bulk metallic glasses can be processed by varying SPS parameters such as pressure and temperature. Xie *et al*. investigated the processing of porous $Zr_{55}Cu_{30}Al_{10}Ni_5$ using SPS. It was demonstrated that porosity of the BMG can be varied from 4.7% to 33.5% by varying the sintering temperature and pressure [35]. The porous bulk amorphous alloy discs exhibited an increase in ductility; however, Young's modulus and fracture strength showed a lower value than as-cast alloy specimen.

Wang *et al*. developed an FEM model for analyzing temperature gradient during SPS processing. Modeling results showed that the temperature at the center was 10-20 ºC higher than that at the edge of the sample [36]. This shows that there is a temperature

gradient between the center and outer edge of the sample which leads to heterogeneous properties. It is likely that the central portion will have greater numbers of nanocrystallized particles than will the outer edge of the sample. Due to the increased number of nanocrystals, the center of the sample demonstrated higher hardness and elastic properties compared to the outer region. In summary, research has demonstrated that SPS is an efficient processing technique for bulk amorphous alloys. However, there are a number of challenges that remain to be addressed.

1.3 Amorphous alloys composites

Amorphous matrix composites are generally classified into two categories depending upon the processing history and microstructure of the composites: *ex situ* and *in situ* composites. *Ex situ* composites are formed by reinforcing crystalline particulates in the amorphous matrix during processing. Reinforcing the crystalline particles within the amorphous matrix hinders the brittle failure of the materials by impeding the growth of shear bands [37-39]. Lee *et al.* studied the ductility of a Ta-reinforced, Cu-based amorphous matrix composite [40]. An enhanced fracture strain of 15.3% was observed in the Cu-based amorphous composite compared to the monolithic amorphous alloy. It was also observed that crystalline particles act as barrier for the propagation of shear bands, which results in plasticity of the amorphous composite.

Formation of nanocrystallites in the amorphous matrix is thought to enhance the tribological properties of amorphous alloys. Maddala *et al.* investigated the response of sliding wear on crystallization of Cu-based amorphous alloys [41]. Formation of nanocrystallites in the amorphous matrix resulted in an increase of hardness and wear

properties of the materials. Annealing of bulk amorphous alloys resulted in the formation of precipitates of nanocrystallites. The nanocrystallites can act as initiation sites for shear bands and hence results in plasticity of amorphous alloys. Gloriant studied the effect of crystallization on properties of Zr, Pd, La, and Al-based metallic glasses and showed that nanocrystallization results in enhancement of hardness and wear resistance. This hardening was mainly due to the presence of high-strength, nano-phase particles and solute enrichment in the amorphous matrix [42]. Li *et al*. investigated the wear behavior of Zr-based BMG and observed that wear resistance of the crystallized sample was higher than the fully amorphous alloy; the least wear resistance was observed for the relaxed amorphous alloy [43].

1.4 Fe-based amorphous alloys

Fe-based amorphous alloys are attractive for structural applications due to their high hardness/strength and exceptional wear and corrosion resistance. It has been reported that the strengths of Fe-based amorphous alloys are about two to three times those of austenitic steels [44] . It is difficult, however, to form bulk useful shapes of these alloys using conventional casting processes [44-47]. Although significant efforts have been made to improve the formability of the alloys by compositional design (e.g., by addition of yttrium and lanthanide elements), the maximum attainable diameter for the best glass forming system is limited to 9-12 mm [45]. Table 1.1 presents a list of Fe-based amorphous alloys developed and some of their key thermal and mechanical properties. Micrometer-sized powder particles can be readily produced using inert gas atomization processes.

Table 1.1: Thermal properties, mechanical properties, and maximum attainable diameters (D) of Fe-based bulk amorphous alloys. σ_f is fracture strength, ε_{pl} is plastic strain, G is modulus of rigidity, and E is Young's modulus. Data from [44].

Alloy Compositions	**D (mm)**	**T_g (°C)**	**T_x (°C)**	**σ_f (GPa)**	**ε_{pl} (%)**	**G (GPa)**	**E (GPa)**
$Fe_{65}Mo_{14}C_{15}B_6$	1.5	516	570	3.8	0.6	73	195
$(Fe_{0.9}Co_{0.1})_{64.875}Mo_{14}C_{15}B_6Er_{0.125}$	2	508	569	3.95	0.5	73	193
$(Fe_{0.9}Co_{0.1})_{64.75}Mo_{14}C_{15}B_6Er_{0.25}$	3	509	570	3.9	0.45	73	193
$(Fe_{0.9}Co_{0.1})_{64.5}Mo_{14}C_{15}B_6Er_{0.5}$	4	517	572	4.1	0.55	73	192
$(Fe_{0.9}Co_{0.1})_{64.25}Mo_{14}C_{15}B_6Er_{0.75}$	4	508	565	4.0	0	73	193
$(Fe_{0.9}Co_{0.1})_{64}Mo_{14}C_{15}B_6Er_1$	3.5	503	557	4.0	0	73	196
$(Fe_{0.9}Co_{0.1})_{63}Mo_{14}C_{15}B_6Er_2$	1.5	494	536				
$(Fe_{0.7}Co_{0.3})_{64.5}Mo_{14}C_{15}B_6Er_{0.5}$	3	505	571				
$(Fe_{0.7}Co_{0.3})_{64}Mo_{14}C_{15}B_6Er_1$	3	497	553				
$Fe_{61}Cr_4Mo_{14}C_{15}B_6$	2	527	580				
$Fe_{59}Cr_6Mo_{14}C_{15}B_6$	1.5	533	585	4.4	0.8	77.4	204
$Fe_{50}Cr_{15}Mo_{14}C_{15}B_6$	1.5	556	601	4.17	0	82	217
$Fe_{60.5}Cr_4Mo_{14}C_{15}B_6Er_{0.5}$	3	530	586	4.0	0	76.6	202
$Fe_{63}Mo_{14}C_{15}B_6Er_2$	3	504	546	4.0	0	77.8	204
$Fe_{55}Cr_8Mo_{14}C_{15}B_6Er_2$	>4					80	209
$Fe_{48}Cr_{15}Mo_{14}C_{15}B_6Er_2$	12	570	620	4.2	0	81	213

Several efforts have been made to realize the potential of these alloys by forming bulk shapes using sintering processes (conventional and spark plasma sintering) or by

forming coatings using high energy processes (thermal spray and laser processing) [17, 48-52]. Most of these processes result in nanocrystallization in the amorphous matrix [44-47].

Fe-based amorphous alloys that can be used for structural applications are popularly known as structurally amorphous metals (SAMs). SAMs are corrosion resistant [53, 54], and these alloys have been successfully coated on different substrates using thermal spray techniques. Fig.1.5 shows the high velocity oxy fuel coating of SAM1651 on half scale spent nuclear fuel prototypical waste package. These coatings perform better than steel components, as only running rust was formed on the SAM during the corrosion test, whereas an aggressive attack was observed on steel components [55]. These materials also have applications as neutron-absorbing components for long-term disposal of nuclear wastes packages due to their exceptional neutron absorption characteristics and stability at high doses of neutrons.

Fig.1.5 High-velocity oxy-fuel (HVOF) coating of SAM 1651 on half-scale spent nuclear fuel prototypical waste package [55].

1.5 Crystallization and thermal stability

As different non-conventional techniques are used to process amorphous alloys in bulk shape, it is essential to investigate the thermal stability and crystallization kinetics during these processes. The crystallization of amorphous alloys involves a combination of phase separation, decomposition, nucleation of crystallites, and growth. Investigations have been performed to understand these processes using different characterization methods to isolate one crystallization mechanism from another [56, 57]. Transmission electron microscopy (TEM), DSC, XRD, and small angle neutron scattering (SANS) have been used in different combinations to investigate the phase transformations in amorphous alloys.

Pekarskaya *et al*. investigated the crystallization path of Zr-based bulk metallic glass using DSC, TEM, and SANS. An interference maximum was observed in the *in situ* SANS experiments during isothermal annealing in the supercooled liquid state due to the decomposition of the metallic glass. TEM of the annealed samples in the supercooled region showed the formation of inhomogeneity in the amorphous composition in agreement with the SANS results [58]. The crystallization of Vit-105 and Vit-106 bulk amorphous alloys was studied by Loffler *et al.* using SANS and TEM. SANS results showed no scattering for the as-received sample, whereas an interference maximum was observed in samples annealed near the glass transition temperature. This interference maximum shifted towards lower Q-range with increases in annealing time mainly due to chemical redistribution and an increase in the crystallite size. In this investigation, the Guinier approximation was used to calculate the effective crystal diameter, and the calculated value agreed well with the TEM results [58, 59]. Holland *et al*. studied the

effects of direct current on the crystallization of Zr-based and Pd-based metallic glasses using *in situ* SANS experiments. It was observed that, for the same annealing temperature, the presence of a direct current resulted in a stronger scattering than in the absence of a direct current. A direct current has a larger impact on volume fraction as well as crystallite size during the crystallization of amorphous alloys [60].

1.6 Laser surface modification of bulk amorphous alloys

The tailoring of amorphous alloy surfaces without affecting the bulk is equally important for various wear and scratch resistant applications. Owing to their ability to attain high cooling rates (~10^5-10^8 K/s) during solidifications, lasers have been used to process bulk amorphous alloys and modify their structural properties [61-64]. Lasers are used to induce amorphous coatings on different substrates, to modify the residual stress distribution, to induce surface melting, and to heat or anneal bulk amorphous alloys. Chen *et al.* investigated the effects of Nd:YAG laser surface treatment on the mechanical properties of Zr-based bulk amorphous alloys. Laser-induced surface melting resulted in an increase in plastic strain (5.3%) mainly due to the redistribution of residual stress and increase in the free volume of the laser melted surface. Residual stress distribution and increase in the free volume may lead to an increase in initiation of multiple shear bands that can further increase the plasticity [64].

Hoekstra *et al.* investigated pulsed excimer laser surface modification of crystalline Al-Co-Ce. Results show the formation of an amorphous composite phase ($Al_{84}Co_{7.5}Ce_{8.5}$) with an embedded nanocrystalline phase of Al_4Ce [65]. Enhancement in corrosion resistance was also observed due to the formation of an amorphous composite

layer after laser treatment. Jing *et al.* investigated the crystallization and thermal fatigue response of Zr-based amorphous alloys after CO_2 laser pulse heating. Cracks were observed after cyclic laser heating of the bulk amorphous alloy surfaces due to the generation of internal stresses between heated and unheated regions. Cracks were observed after a low number of cycles and well below the crystallization temperature. This indicated the low crack resistant nature of these alloys under thermal loading. The structural changes induced by thermal relaxation played a significant role in the formation of cracks [66].

CHAPTER II

OBJECTIVES AND PROPOSED WORK

Amorphous alloys exhibit high microhardness, fracture toughness, and fracture strength at ambient temperature. These outstanding properties are mainly due to the disordered atomic arrangements and absence of grain boundaries and defects in the microstructure of these amorphous alloys. Despite these exceptional properties, utilization of amorphous materials for structural applications has been limited; this is primarily due to difficulties in fabrication of large (bulk) samples using conventional casting techniques. However, the amorphous powder of various glass forming compositions can be readily prepared using gas atomization process. Recently, SPS has evolved as a novel technique for sintering amorphous powder into bulk shapes without undesirable phase transformations. SPS involves combined application of pulsed direct current and uniaxial pressure to consolidate difficult-to-sinter materials [19, 26].

Development of Fe-based bulk amorphous alloys having composition $Fe_{48}Cr_{15}Mo_{14}Y_2C_{15}B_6$ is considered important due to its excellent corrosion and wear resistant properties [55]. With the overarching objective of processing fully dense Fe-based bulk amorphous alloys using spark plasma sintering, many fundamental effects were investigated during this research for this dissertation such as: (1) densification behavior under the influence of current; (2) thermal effects at the micro- (at

Particle contacts) and macro-scales (in bulk samples); (3) effects of SPS processing on structural relaxation, crystallization, and evolution of nanocrystallite size distribution; and (4) effect of partial crystallization (thermal annealing and laser treatment) on tribological behavior of bulk amorphous alloys and their modified surfaces.

2.1 Processing, densification, and temperature distribution of SPS of Fe-based bulk amorphous alloys

A few studies have been performed on SPS of bulk amorphous alloys; however, little emphasis was given to the densification behavior or the characterization of amorphous/partial crystallized phases [67]. In the present investigation, SPS of Fe-based bulk amorphous alloys was performed at different temperatures below T_g ranging from 475 ºC to 575 ºC at a pressure of ~225 MPa for different soaking times. Densification behavior and phase transformations of SPS-sintered samples were analyzed, and these results were correlated to microhardness and fracture toughness.

Fe-based amorphous alloys can be sintered in the supercooled region above T_g and below T_{x1}, where viscous flow of the material enhances sinterability. Processing of bulk amorphous alloys in the supercooled region was previously investigated by Schroers *et al.* using thermoplastic forming (TPF), where bulk amorphous alloys are reheated in the supercooled region to obtain required shapes [3]. SPS was performed at 630 ºC (within T_g and T_x), 70 MPa, and a sintering time of 10 min. Densification behavior during SPS was investigated using punch displacement data and was correlated to the DSC of the as-received Fe-based amorphous powder. Experiments were performed to separate

the effects of pressure, temperature, and change in viscosity in the supercooled region during SPS sintering.

Due to the narrow supercooled region, the accuracy of measurement of sintering temperatures and the temperature distribution play a crucial role in obtaining fully dense amorphous alloys or amorphous alloy composites with controlled crystallization. Thermal models are also important for the analysis of scalability of SPS process for making bulk samples. Analytical and thermal models were developed for the SPS sintering of Fe-based bulk amorphous alloys. Many investigators have proposed that the presence of localized heating and melting at the surface contact of the amorphous powder allow the core of the powder to remain at lower temperatures [23, 24, 68]. Fundamental analytical calculations were made to investigate temperature distribution along the diameter of the particle with the resistivity of the amorphous alloy and electric current as input parameters. A three dimensional finite element thermo-electric model for the SPS processing was developed. This model was used to predict the temperature distribution in the tooling and also in the amorphous sample during various stages of sintering.

2.2 Effects of SPS processing on structural relaxation, crystallization, and evolution of nanocrystallites size distribution

Fe-based amorphous alloys are expected to undergo structural relaxation due to thermal processing. The mechanisms of structural relaxation on crystallization behavior of amorphous materials are not well understood. Some studies indicate that the crystallization initiates at the separation of two or more amorphous phases. In addition, in order to relate crystallization behavior with the mechanical properties of bulk amorphous

alloys, it is essential to obtain crystallite size distribution of the partially crystallized samples. Our current knowledge of phase transformations in amorphous materials is mostly built upon patterns obtained from *ex situ* x-ray diffraction on samples that had undergone such transformations. The lack of *in situ* time-resolved data collected at different stages of crystallization leaves many unresolved questions, particularly related to mechanisms of nucleation and growth. In this investigation, phase separation, crystallization, and grain growth mechanisms in structurally relaxed Fe-based amorphous materials were investigated using both *ex situ* and *in situ* SANS. In addition, these experiments facilitated quantification of crystallites present in bulk amorphous samples, which further were related to the mechanical behavior of these alloys.

In this investigation, SANS experiments on SPS-sintered Fe-based amorphous alloys were conducted at the extended Q-range SANS at the Spallation Neutron Source at the Oak Ridge National Laboratory (ORNL). *In situ* SANS experiments at elevated temperatures (up to 800 °C) were conducted using a general-purpose small angle neutron scattering diffractometer (CG-2) available at the high flux isotope reactor (HFIR) facility at ORNL. The objective of SANS experiments on different spark plasma sintered Fe-based bulk amorphous alloys was to investigate any cluster formation in the supercooled region that was not detectable by XRD. SANS data can also be fitted to obtain particle size distribution of the crystallites, which is crucial for relating it to crystallization mechanisms and mechanical properties.

Scattering intensity data at various Q values [variation of scattering intensity S ($cm^{-1}sr^{-1}$) with scattering vector Q-values ($Å^{-1}$)] were obtained. Any spatially correlated inhomogeneities at nanometer scale were indicated by the changes in the scattering

intensity. Such *in situ* SANS results were used in combination with TEM and DSC data to investigate the crystallization pathways. Possible pathways include crystallization triggered by "quenched-in" nuclei acting as heterogeneous nucleation sites or the crystallization triggered by separation of amorphous matrix into two amorphous phases.

2.3 Effects of nanocrystallization (thermal annealing and laser treatment) on the mechanical and tribological properties

The effect of annealing at two different temperatures, 700 °C and 800 °C, was performed on SPS-sintered bulk amorphous alloys to investigate the effect of partial crystallization on microhardness and wear behavior. Detailed investigations were also performed on the effect of indentation loads on microhardness. In theory, the hardness of bulk amorphous alloys should be independent of applied loads; however, a dependence on applied load was observed during experiments. Reasons for this dependence are discussed below. Wear behavior was analyzed for SPS-sintered and annealed samples, and the likely mechanisms involved in wearing of the Fe-based bulk amorphous alloys are presented. Wear track and wear debris characterization were used to investigate the wear behavior of amorphous and partially crystallized bulk samples. Mechanical tests such as microhardness and compression tests were performed on the sintered samples. Microhardness and compression test data were correlated with the densities, crystallite size, and degree of crystallization.

CHAPTER III

EXPERIMENTAL DETAILS

3.1 Materials

A Fe-based amorphous alloy having composition $Fe_{48}Cr_{15}Mo_{14}Y_2C_{15}B_6$ was used in this investigation. Fe-based amorphous powders were prepared using a high pressure gas atomization technique. A mixture of pure elemental powders Fe, Cr, Mo, Y, B, and C, with the nominal chemical composition of $Fe_{48}Cr_{15}Mo_{14}Y_2C_{15}B_6$, were melted under a high purity Ar atmosphere and then atomized using high purity inert gas. This powder was prepared under program name DARPA Structural Amorphous Metals (SAM), where amorphous alloys based on iron, magnesium, titanium and aluminum were fabricated [45, 69].

3.2 SPS of Fe-based amorphous powder

The SPS technique was used to consolidate the Fe-based amorphous powder. Two different toolings were used for the consolidation of the amorphous powder. In the first set of experiments, WC dies and punches were used for high pressure (225 MPa) experiments, and temperatures were varied from 475 °C to 575 °C. Temperature during sintering was measured using a K-type thermocouple. Simultaneous uniaxial pressure up

to 225 MPa was applied during the sintering process experiments. Experiments were performed using, graphite dies and punches and sintering temperatures were varied from 570 ºC to 800 ºC at a uniaxial pressure of 70 MPa. A typical processing cycle consisted of three steps: (1) rapid heating at a rate of 100 ℃/min., (2) holding for 15 min. at the processing temperature, and (3) rapid cooling using nitrogen purging (cooling rate ~150 ℃/min.). All the samples were sintered in a closed furnace in a vacuum of 10^{-2} Torr. The diameters and thicknesses of the discs obtained were 20 mm and 1 mm, respectively. Punch displacement data were collected with respect to sintering temperature, pressure, and time during the SPS processing.

3.3 Laser surface modification

A 2.5 kW continuous wave ytterbium-doped Nd:YAG laser beam at a wavelength of 1.064 μm was used to perform laser-induced surface modification. The laser system was equipped with a fiber optic beam delivery system. The laser power was 100 W, and scan speeds from 80 mm/s to 120 mm/s were used to process the bulk amorphous alloys.

3.4 X-ray diffraction (XRD)

XRD analysis of the processed bulk amorphous alloys was carried out using a Philips Norelco X-ray diffractometer operating with Cu (K_α = 1.54178 Å) radiation at 45 kV and 40 mA. The diffraction angle was varied between 30° and 70° at a step increment of 0.02° with a count time of 1 s. The crystallite size for SPS-sintered partially crystallized Fe-based amorphous samples was calculated using the Scherrer equation:

$$FWHM = \frac{K\lambda}{Dcos\theta}\frac{180}{\pi} \quad (3.1)$$

where *FWHM* is full width, half maxima in 2θ degrees, *D* is the crystallite size in nm, *K* is constant (0.94), and λ is the wavelength of Cu K_α radiation [70].

3.5 Extended Q-range small angle neutron scattering (EQ-SANS)

EQ-SANS experiments were performed at beam line 6, Spallation Neutron Source at the ORNL, Tennessee, USA. This newly designed facility is known for its wide Q-coverage, high neutron beam intensity, and excellent wavelength resolution [27]. Experiments were performed using a Q-range of 0.004 $Å^{-1}$ to 0.5 $Å^{-1}$ where Q is $4\pi Sin\theta/\lambda$ and θ is half of the scattering angle. The sample to detector distance was 4 m, and the detector to source distance was 1.8 m. SANS scans were performed on as-received amorphous powder as well as sintered samples of thickness ~1 mm. Experiments were performed with a starting wavelength of 1.96 Å. Data collection time lasted for 1 hour per sample. Appropriate data reductions were performed using a data processing program developed by Zhao *et al*. to accommodate factors such as transmission and thickness of the samples [27]. Irena software was used for modeling and analysis of the EQ-SANS results. A size distribution analysis tool available in the Irena analysis package was used to determine the crystallite size [71].

3.6 Scanning electron microscopy (SEM) and energy dispersive spectroscopy (EDS)

The characterization of microstructure of sintered discs was conducted using a Joel JSM-6360 SEM. The chemical characterization of the constituents in the amorphous alloys was conducted using EDS. An FEI Quanta 600 field-emission gun environmental

scanning electron microscope with an Evex EDS X-ray microanalysis system and a HKL EBSD system was used for EDS analysis.

3.7 Transmission electron microscope (TEM)

Sintered bulk amorphous alloys were polished using SiC polishing papers to a few microns. TEM samples were prepared using an FEI Nova 200 Nano Lab dual beam focused ion beam (FIB) technique. A detailed microstructure analysis was conducted using an FEI Tecnai F20 field emission gun TEM operated at 200 KV.

3.8 Differential scanning calorimetry (DSC)

DSC analysis of the samples was conducted using an SDT Q600 V8.2 Build 100 instrument at a heating rate of 20 ºC/min. Alumina crucibles were used for the experiments and Ar was used as protective gas. A sample mass of 10 mg was used for the experiments.

3.9 Microhardness and fracture toughness

A Clark's microhardness tester was used for measuring hardness by performing indentations at a load of 2.94 N and a holding time of 12 s. About 15 microhardness readings were taken on each sample, and an average value was reported. Fracture toughness (K_{IC}) was obtained using a direct crack measurement method. The fracture toughness, K_{IC}, is given by

$$K_{IC} = 0.016\left(\frac{E}{H}\right)^{\frac{1}{2}} \frac{P}{c^{\frac{3}{2}}} \tag{3.2}$$

where E is the Young's modulus (GPa), H is the Vickers hardness (GPa), P is the applied load (N), and c is the diagonal crack length (m). The literature value of 200 GPa for the Young's modulus of Fe-based amorphous alloys was used for fracture toughness calculations. The fracture toughness was obtained for 10 indentations on each sample, and the average value was reported [72].

3.10 Wear test

The wear tests were performed on the polished bulk amorphous samples using a ball-on-disc tribometer at a load of 10 N and 136.3 rpm disc rotation. A 3-mm diameter alumina (Al_2O_3) ball was used as a counter body to create a wear track of 6 mm in diameter on the sample surface. The weight loss was recorded as a function of linear sliding distance. The sample surfaces before and after wear were analyzed using an SEM equipped with an EDS detector. Depth profiles of the wear scars obtained after the wear test were measured using a non-contact optical profilometer.

3.11 Compression test

Compression tests of the Fe-based BMG samples having a diameter to length ratio of 1:2 were performed using an Instron 5582 series Universal testing machine. Three samples were tested for each processing condition, and the average compressive strength value was reported.

3.12 Laser thermal modeling

A three-dimensional thermo-physical model using COMSOL was developed to investigate temperature distribution, heating and cooling rates, and thermal gradient along the thickness of the material during laser-induced surface modification of the Fe-based bulk amorphous alloys. A disc of diameter 20 mm and thickness 1 mm was considered as the sample dimension for the analysis. Equation 3.3 presents energy balance between the total heat flux and the temperature rise within the sample:

$$C_p = \frac{\partial T(x,y,z,T)}{\partial t} = k\left[\left(\frac{\partial T(x,y,z,T)}{\partial x}\right) + \left(\frac{\partial T(x,y,z,T)}{\partial y}\right) + \left(\frac{\partial T(x,y,z,T)}{\partial z}\right)\right] \quad (3.3)$$

Appropriate boundary conditions such as conduction, convection, and radiation were applied using equation 3.4:

$$-k\left[\left(\frac{\partial T}{\partial x}\right) + \left(\frac{\partial T)}{\partial y}\right) + \left(\frac{\partial T)}{\partial z}\right)\right] = P-\epsilon\sigma\left[T^4-T_0^4\right]-h[T-T_0] \quad (3.4)$$

Tables 3.1 and 3.2 present laser parameters and thermo-physical material properties, respectively, used in the modeling of laser-induced surface modification of bulk amorphous alloys.

Table 3.1: Parameters involved in laser surface treatment of Fe-based amorphous alloys

Name	**Value**	**Unit**
Total laser power (P)	100	W
Laser velocity (U)	90	mm/s
Spot radius (r)	0.3	mm
Irradiation time (t_p)	10	Mm/U
Boltzmann const. (σ)	$5.67x10^{-8}$	$W/(m^2.K^4)$
Emissivity (E)	0.4	

Name	Value	Unit
Absorption coef. (A_c)	6.7	1/cm
Heat transfer coef. (F)	2500	W/((m^2).K)
Initial temp. (T_o)	298	K

Table 3.2: Materials properties used in laser surface modeling of Fe-based bulk amorphous alloys [52]

Name	Value	Unit
Heat capacity at constant pressure (C_p)	750	J/(kg.K)
Density (ρ)	7500	kg/m^3
Thermal conductivity (k)	40	W/(m.K)
Thermal convectivity (h)	2500	(W/m^2K)

CHAPTER IV

RESULTS AND DISCUSSIONS

4.1 Characterization of as-received amorphous alloy powder

A Fe-based amorphous alloy having composition $Fe_{48}Cr_{15}Mo_{14}Y_2C_{15}B_6$ was used in the investigation. Fig 4.1 (a) shows a SEM image of amorphous particles and their morphologies. The amorphous alloy particles were mostly spherical and elliptical in shape. Fig. 4.1 (b) shows particle size distribution of amorphous alloys obtained using a sieving machine. The size of the particles varied from less than 20 µm to greater than 200 µm. The amorphous powder particles of size less than 100 µm amounted to about 82 % by weight of the as-received powder. The particle size distribution plays a significant role in the densification and sintering of amorphous powders. German demonstrated that wide distribution of particle size results in high packing and sintering densities[73]. For wide particle size distribution, the sintering is dominated by densification of the larger particles, whereas the smaller particles help in attaining high packing density [73].

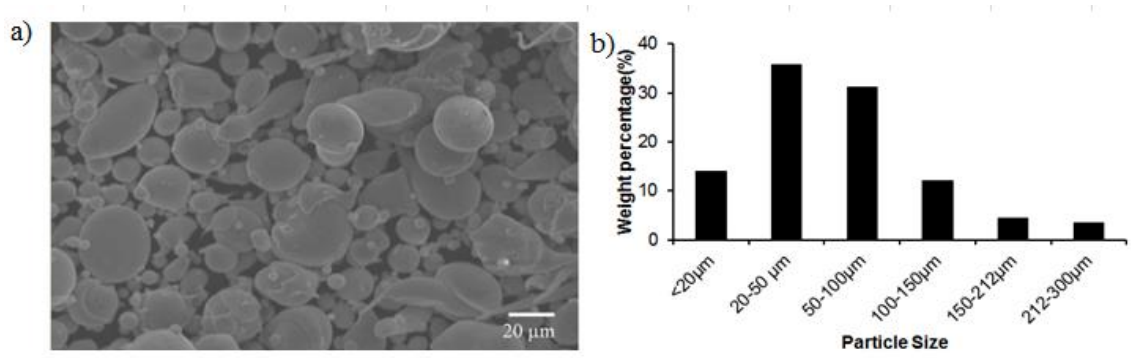

Fig 4.1 a) SEM image, and b) particle size distribution obtained by sieving of as-received Fe-based amorphous powder.

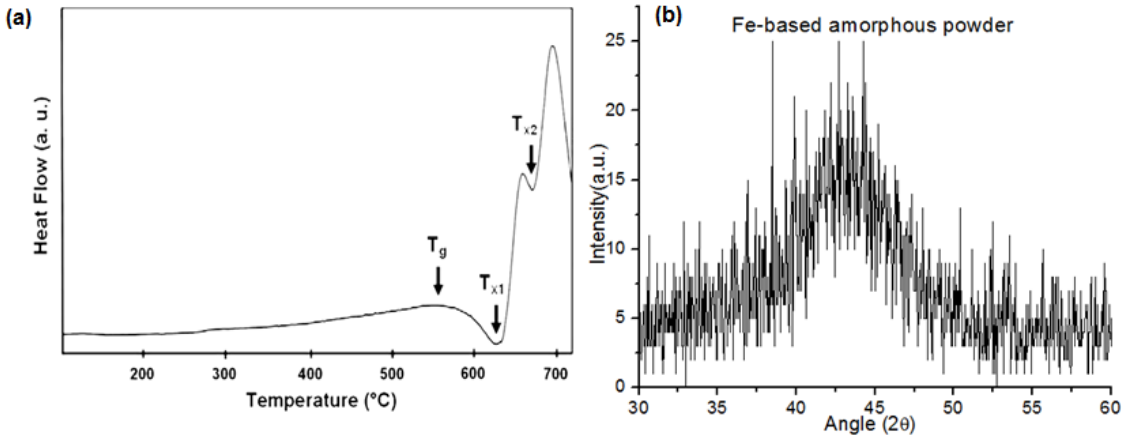

Fig 4.2 a) DSC scan, and b) XRD of as-received Fe-based amorphous powder [49].

DSC scan of the as-received amorphous powder is presented in Fig 4.2 (a). The powder exhibited characteristic behavior associated with amorphous materials with distinct glass transition temperature at 575 °C followed by double exothermic peaks corresponding to crystallization temperatures, T_{x1} and T_{x2}. The results confirmed the glassy structure of the alloy powder prior to SPS. XRD of the amorphous powder is shown in Fig 4.2 (b). A broad halo diffused peak which is characteristic of the amorphous

phase was formed between the 2Theta positions between 35º and 55º having maximum peak position at 42º.

4.2 SPS of Fe-based bulk amorphous alloys below glass transition temperature

In an attempt to maximize the density and retain the amorphous composition, various combinations of SPS processing parameters (sintering temperature, pressure, and holding time) were explored. A summary of SPS processing parameters used in present investigations is presented in Table 4.1. Initial sintering experiments were conducted at 475 °C, the temperature almost 100 °C lower than glass transition temperature to maximize the chances of retaining amorphous composition. The vertical force of 225 MPa was used in all the sintering experiments.

Table 4.1: Processing conditions, crystallite size, and properties of SPS sintered Fe-based bulk amorphous alloys.

Sample ID	Sintering Temperature (ºC)	Holding Time (min.)	Relative Density (%)	Crystallite size (nm)	Hardness (HV)	Fracture toughness MPa-$m^{1/2}$
A	475	5	92.76	-	-	
B	475	10	94.13	-	-	
C	550	20	98.86	9.9	1341±60	1.67±0.3
D	575	20	99.07	11.7	1230±57	1.58±0.3

The sintering experiments were conducted using a WC die with a thermocouple placed inside the wall of the die for temperature measurement. Around 7 g of amorphous powder was used to sinter each disc specimen of 12 mm diameter and 10 mm height.

4.2.1 Phase analysis

Fig 4.3 presents the XRD patterns obtained from as-received amorphous powder and compacts sintered with various processing parameters (sintering temperature and holding time). As-received powder exhibits a characteristic broad halo with diffused intensity indicating a fully amorphous structure. The SPS sintered compacts at a temperature lower than the glass transition temperature also exhibit fully amorphous structure (samples A and B). To understand the influence of sintering temperature on the phase evolution, two specimens were sintered at temperatures close to the glass transition temperature of the amorphous alloy (samples C and D). XRD patterns from these samples exhibit predominantly amorphous background with superimposed crystalline peaks corresponding to $Fe_{23}(C, B)_6$ indicating formation of an amorphous matrix containing crystalline phases.

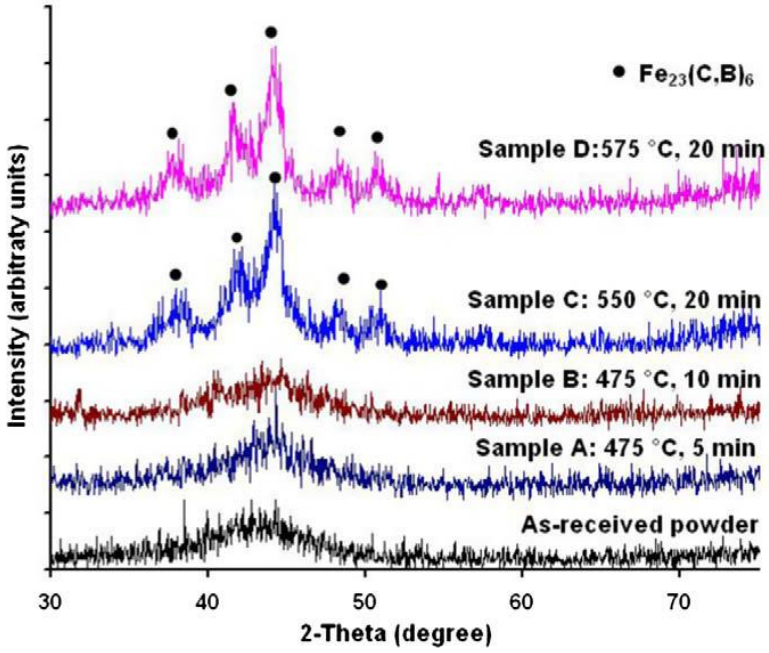

Fig 4.3 XRD of SPS sintered Fe-based amorphous alloys at different processing conditions [49].

Table 4.1 also presents the average crystallite size of the crystalline phases determined from the peak broadening in XRD pattern using Scherer's equation. It is clear that the crystallite size increases from 9.9 to 11.7 nm with an increase in sintering temperature from 550 to 575 °C. It should be noted that the sintering temperatures reported in these studies were measured using a thermocouple placed inside the die wall during sintering. The actual temperature inside the specimen may be significantly higher than temperature at the die wall. In view of this, the appearance of superimposed crystalline peaks in XRD patterns of samples sintered at temperatures well below the crystallization temperatures (T_{x1} and T_{x2}) may be attributed to the local overheating of the particle surfaces during sintering.

4.2.2 Densification behavior

Relative densities of the sintered compacts sintered at various processing conditions are presented in Table 4.1. At sintering temperature 100 °C lower than glass transition temperature (samples A and B), increasing sintering time improves the densification while retaining bulk amorphous composition. Thus, highly dense (95%) fully amorphous compositions can be obtained within a short sintering time (5–10 min.) by SPS. Fig. 4.4 presents the representative microstructures of the amorphous powder sintered at 475 ºC and 550 ºC. The microstructure of the compacts sintered at 475 ºC clearly indicates the porous structure in the sintered samples (Fig 4.4 a). The amorphous powders achieve nearly 99% relative density in the compacts after sintering in the range of 550–575 ºC. The featureless microstructure of the polished surface in the compact sintered at 550 ºC indicates primarily amorphous structure (Fig 4.4 b).

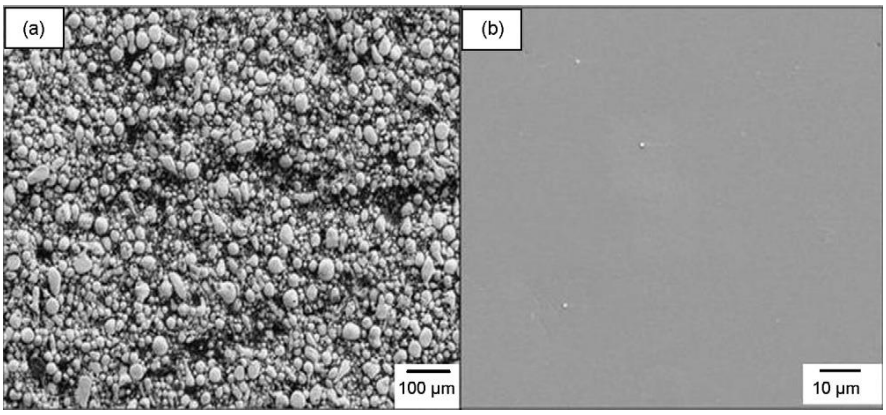

Fig 4.4 Microstructures of amorphous compacts SPS sintered at: a) 475 ºC, and b) 550 ºC [49].

To gain more insight into the densification behavior of the amorphous materials during SPS, the displacement of the punch was monitored during the sintering process. Fig. 4.5 presents the typical variation of actual temperature and punch displacement over

time during sintering of the amorphous powder. The figure indicates that almost all of the total punch displacement takes place during the heating stage of the sintering cycle with negligible punch displacement during the holding stage. This suggests that the heating stage of sintering cycle plays an important role in the densification of the compacts while the holding stage of the sintering cycle is primarily characterized by structural transformations such as devitrification of amorphous phases.

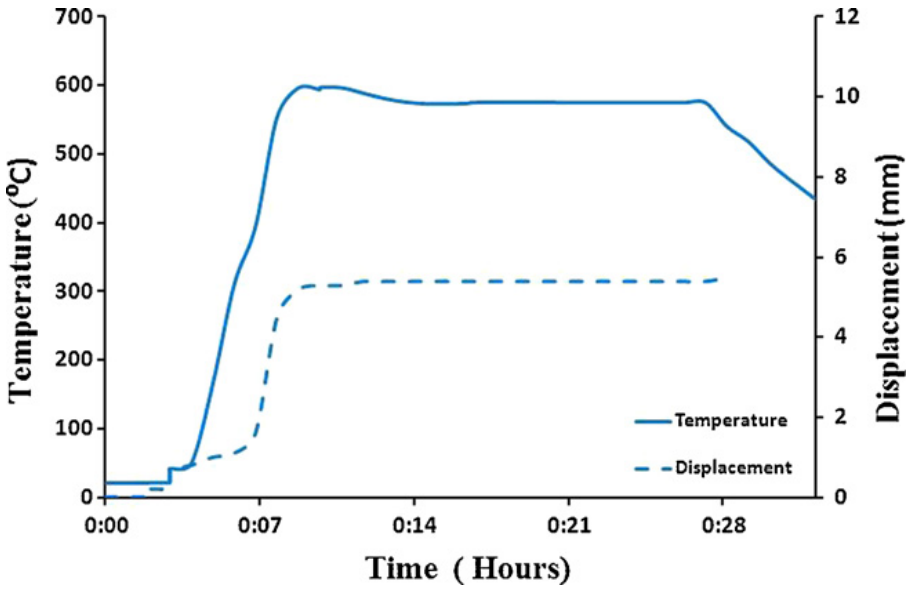

Fig 4.5 Typical variation of temperature and punch displacement during SPS of amorphous powder (sintering temperature: 575 °C, holding time: 20 min.) [74].

4.2.3 Microhardness and fracture toughness

Table 4.1 also presents the microhardness and indentation fracture toughness of SPS sintered samples C and D. Note that due to porous structure in the samples sintered at low temperature (samples A and B), reliable/repeatable readings of the microhardness and fracture toughness could not be obtained. As indicated in the table, near-fully sintered samples exhibit very high Vickers hardness (1200–1400 HV). A slight decrease

(100 HV) in hardness with an increase in sintering temperature from 550 to 575 ºC may be associated with the enhanced nucleation/growth of crystalline phases in the amorphous matrix. As discussed earlier, the change in sintering temperature is associated with increase in crystallite size. Fig. 4.6 presents the SEM micrograph of a Vickers hardness indentation made on polished the surface of a spark plasma sintered compact (sample C: 550 ºC, 20 min.). The polished surface does not show any surface porosity, indicating full densification of the amorphous powder under prevailing SPS processing conditions. The micrograph clearly indicates the cracks emanating from the corners of indentation. The formation of slip markings adjacent to some of the faces of the indentation is consistent with the earlier reports on indentation of amorphous alloys [75]. The fracture toughness of the near-fully sintered compacts is found to be in the range of 1.2–2.0 MPa $m^{1/2}$. Such low values of fracture toughness represent the brittle nature of amorphous compacts. Since Vickers hardness of the amorphous compacts decreased with the increased sintering temperature (550–575 ºC), a slight decrease in indentation fracture toughness (0.1 MPa $m^{1/2}$) with increasing sintering temperature seems unexpected. This may be due to combined effect of porosity, embedded crystalline phases, and residual stresses in the sintered compacts. In summary, SPS of amorphous powder ($Fe_{48}Cr_{15}Mo_{14}Y_2C_{15}B_6$) at sintering temperature of about 100 °C lower than glass transition temperature results in highly dense (~95%) fully amorphous compacts. Formation of crystalline $Fe_{23}(C, B)_6$ phases within a near-fully dense (~99%) amorphous matrix is observed at a sintering temperature close to the glass transition temperature (which is significantly less than the crystallization temperatures: T_{x1} and T_{x2}).

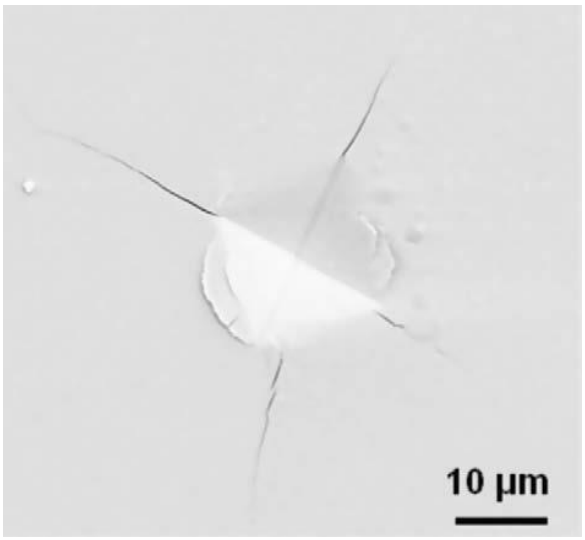

Fig 4.6 SEM micrograph of a Vickers hardness indentation made on a polished surface of a SPS sintered compact (sample C: 550 °C, 20 min.) [49].

Microstructure evolution in the sintered compacts indicated that density, degree of crystallinity, and mechanical properties can be effectively controlled by optimizing SPS processing parameters. Thus, SPS presents tremendous potential for fabrication of 'bulk' amorphous and amorphous matrix composites at significantly lower temperatures and shorter times.

4.3 SPS of Fe-based bulk amorphous alloys in the supercooled region

Fe-based amorphous powder having composition $Fe_{48}Cr_{15}Mo_{14}Y_2C_{15}B_6$ (at. %) was used in this investigation. SPS technique was used to consolidate the Fe-based amorphous powder at 630 ºC, 70 MPa, and for 10 min. The sintering was performed using graphite dies and punches. About 3 g of powder was sintered to produce disc-shaped samples of diameter 20 mm and thickness 1 mm.

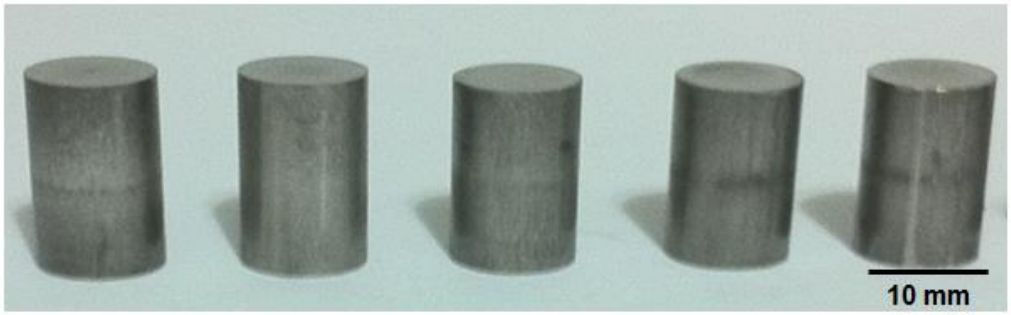

Fig 4.7 Typical shapes of Fe-based bulk amorphous alloy samples SPS sintered in supercooled region.

Similarly, higher thickness samples were also processed in the supercooled region. Samples of diameter 10 mm and 15 mm thickness are shown in Fig. 4.7.

4.3.1 Densification behavior

An SEM micrograph from the polished surface of a Fe-based amorphous alloy SPS sintered at 630 °C (with uniaxial pressure of 70 MPa and hold time of 10 min.) is shown in Fig. 4.8. The micrograph shows dense microstructure with little open porosity. The relative density of the SPS sintered samples was measured to be ~98.5% using the Archimedes principle. Fig 4.9 shows EDS elemental mapping of polished surface of SPS sintered Fe-based amorphous alloy at 630 °C. EDS experiments were performed at different magnifications (500–15,000X). No significant changes were observed in the elemental distributions at high magnification SEM images when compared to low magnification images.

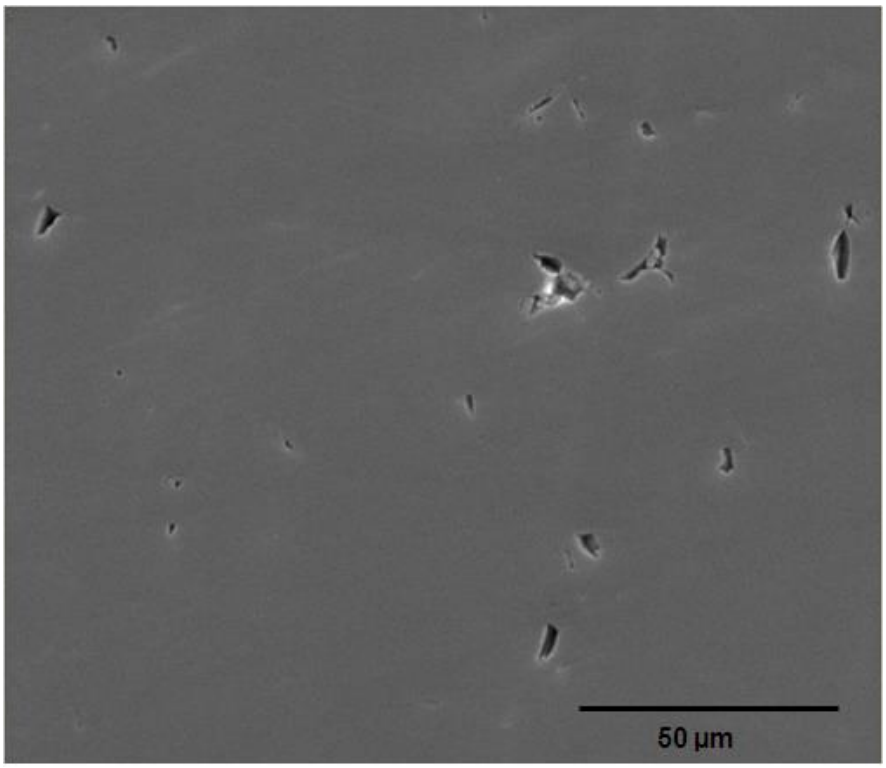

Fig 4.8 SEM micrograph of the polished surface of SPS sintered Fe-based amorphous alloy at 630 °C, 70 MPa, and 10 min. [76].

Note that SEM/EDS cannot resolve the elemental redistribution at nanometer length scale associated with nanocrystallization effects. Similar high magnification EDS analysis was followed by Bakkal *et al.* to demonstrate compositional changes in Zr-based bulk metallic glass during machining [77]. Elemental composition appears homogenous without any localized high concentrations of any elements.

Fig. 4.10 (a) presents the typical variation of punch displacement during SPS with temperature. The DSC pattern from the starting amorphous powder is also plotted in the same figure. Note that the pressure was also increased from 5 to 70 MPa with a temperature increase from 25 to 630 °C. The figure indicates a punch displacement of ~0.4 mm in the early stage of the sintering cycle (25 to 200 °C).

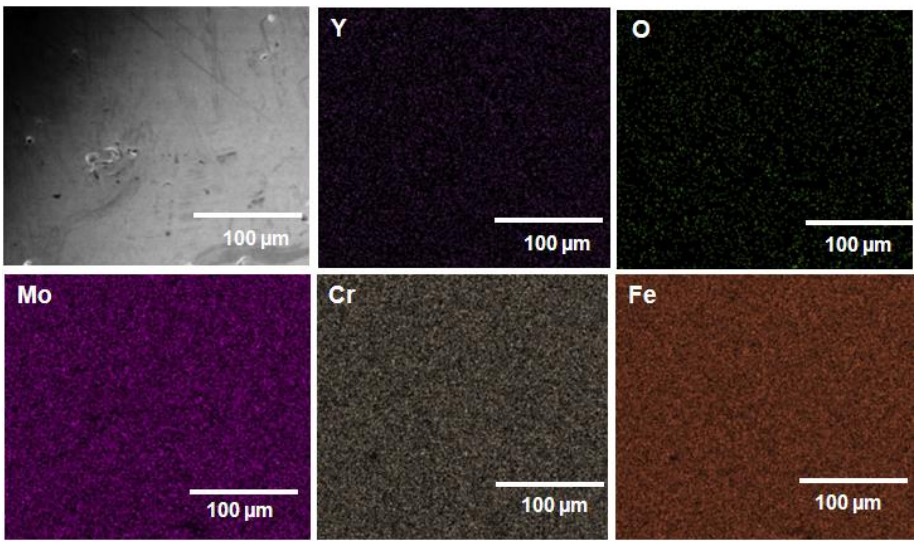

Fig 4.9 EDS of the surface of Fe-based amorphous alloy SPS sintered at 630 °C and 70 MPa [76].

This initial punch displacement is primarily due to re-arrangement of amorphous particles. Negligible punch displacement (<0.1 mm) was observed from 200 to 500 °C. Out of total punch displacement of 1.3 mm, about 0.5 mm was observed in the temperature range of 25 to 500 °C. The remaining ~0.8 mm of punch displacement was observed in the temperature range of 500 to 630 °C. It can be seen from the DSC pattern that this range of SPS processing temperature covers the supercooled liquid region ($\Delta T=T_x-T_g$) for the given composition of bulk metallic glass. It is well known that amorphous alloys are in a highly viscous liquid state in this temperature range [3]. This property of the amorphous alloys has been extensively utilized for superplastic forming of these materials. The sintering of amorphous powder in the supercooled liquid range also seems to enhance densification as indicated by the large punch displacement in this relatively narrow temperature range. To investigate the effect of hold time on the densification behavior, the variation of temperature and punch displacement with SPS

processing time was also analyzed (Fig 4.10 b). It can be clearly seen that almost no punch displacement occurred during the hold time. For these observations, it seems that densification of amorphous powder during SPS sintering is dominated by particle re-arrangement at lower temperature (25-200 °C) and particle deformation in supercooled region at higher temperature (500-630 °C) during heating. However, hold time is important for solid state diffusion across the particle interfaces. Due to the amorphous nature of the powders, it is difficult to trace the original interfaces between the adjacent particles (Fig. 4.8). In the polycrystalline materials, the original particle interfaces often evolve as grain boundaries.

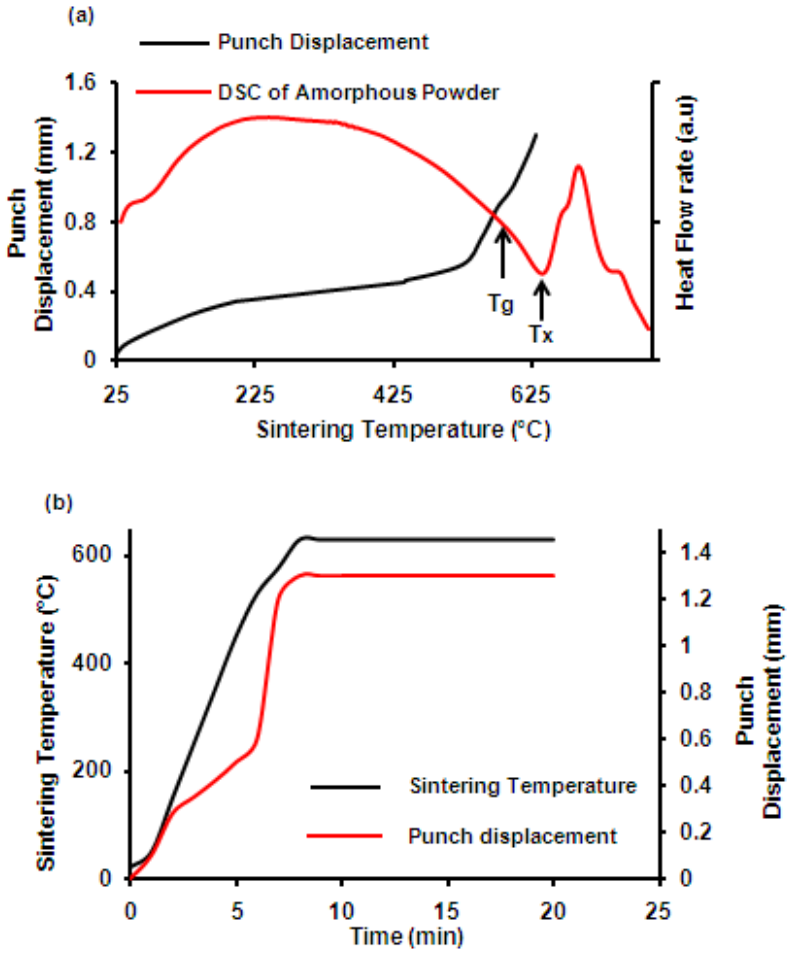

Fig 4.10 a) Typical variation of punch displacement with temperature during SPS of amorphous alloy (DSC pattern for the given alloy is also shown), and b) variation of temperature and punch displacement with SPS processing time [76].

To delineate the effects of temperature and pressure on the densification behavior, the pressure was increased from 5 to 70 MPa at a constant temperature of 25 °C followed by an increase in temperature from 25 to 630 °C at a constant pressure of 70 MPa. The sample was then held at 630 °C at 70 MPa for 10 min. The variation of punch displacement over time indicating various stages of the SPS processing cycle is presented in Fig. 4.11.

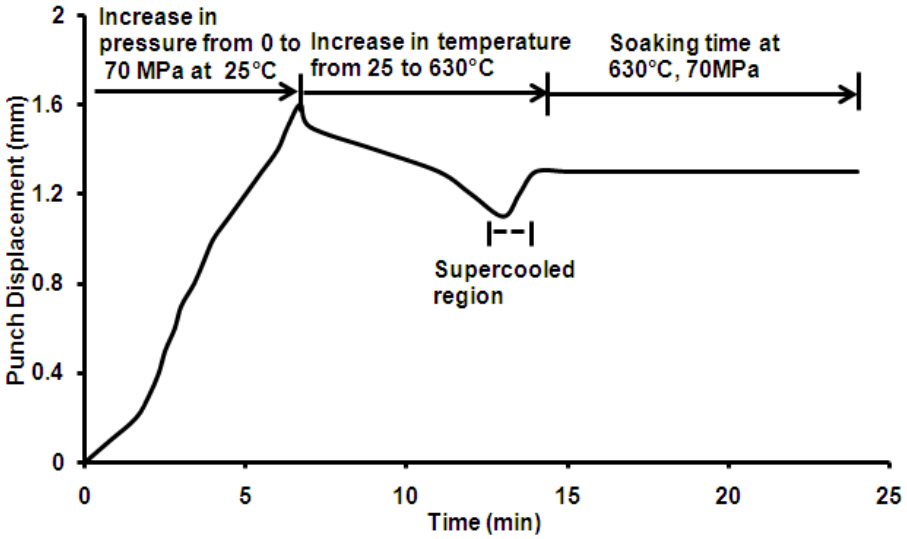

Fig.4.11 Punch displacement of Fe-based amorphous alloy during SPS, where pressure and temperature were increased separately [76].

The punch displacement of about 1.6 mm was observed with the increase in pressure from 5 to 70 MPa at a constant temperature of 25 °C. Further increase in temperature up to 575 °C (at constant pressure of 70 MPa) resulted in a decrease in punch displacement by about 0.6 mm, indicating thermal expansion of the powder. When the temperature reached the supercooled liquid region, a positive punch displacement of 0.3

mm was observed resulting in the total resultant punch displacement of 1.3 mm. When Fe-based amorphous alloys and composites were sintered below supercooled liquid region (550-575 °C), high pressure (~225 MPa) and longer sintering time (20 min.) were needed to achieve relative density of ~99% in these alloys. Clearly, sintering of amorphous powder in the supercooled liquid range accelerates the viscous flow and densification of the powder at relatively lower uniaxial pressure and shorter sintering time.

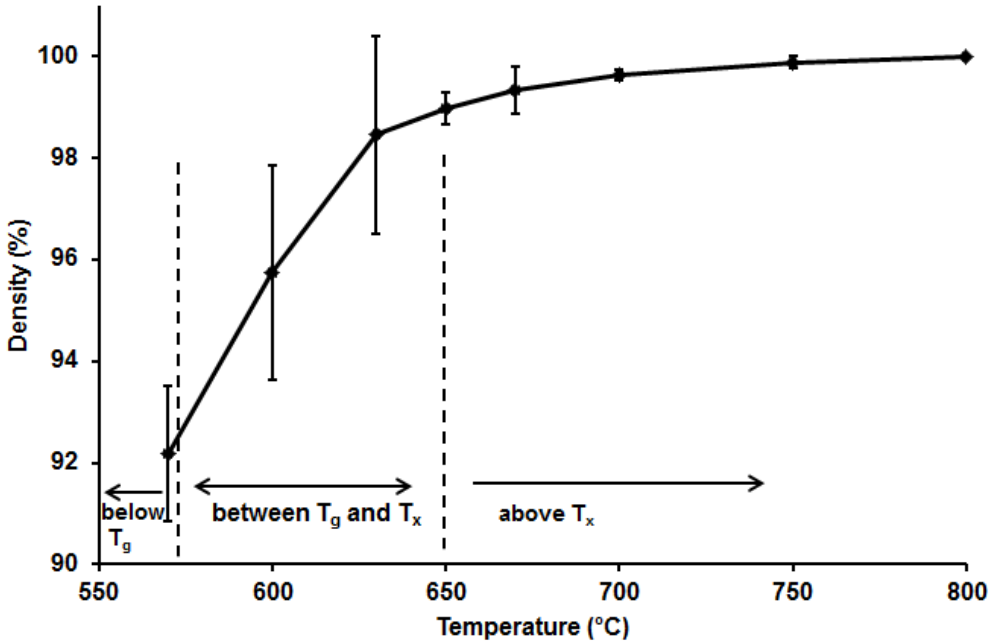

Fig.4.12 Density of SPS sintered Fe-based bulk amorphous alloys at different temperatures at a uniaxial pressure of 70 MPa and soaking time of 10 min.

Fig. 4.12 presents relative densities of the SPS sintered samples at sintering temperatures 570, 600, 630, 650, 700, 800 ºC with a uniaxial pressure of 70 MPa. The density of the samples increased from 92% (7.12 g/cm^3) to 99.99 % (7.75 g/cm^3: theoretical density) when sintering temperature was increased from 570 °C to 800 °C, keeping pressure and soaking time constant. Rate of change of density with respect to sintering temperature

was 0.1 percent per Celsius from 570 ºC to 630 ºC whereas density rate slowed down to 0.006 percent per Celsius from 650 ºC to 800 ºC. This shows maximum densification occurred in the supercooled region and densification rate slowed down once the sintering temperature reached crystallization temperature (T_{x1}). This clearly indicates sintering in the supercooled region leads to densification at lower sintering pressures (less than 100 MPa) and shorter sintering time.

Fig. 4.13 (a) shows punch displacements at different temperatures ranging from 600 °C to 700 °C. Three different regions were observed in the punch displacement graph. In the first region (25 ºC to 200 ºC), an average punch displacement of 0.4 mm was observed which is mainly due to the particle rearrangement in the initial stage of sintering. Particle rearrangement is due to sliding and rotation of the amorphous particles wherein the small amorphous particles fill the gaps between large size particles. The second region in the punch displacement graph (from 200 ºC to 570 ºC) is due to the combined effect of temperature and pressure (region 2) and a displacement of 0.2 mm was observed indicating no significant sintering in this region. An average punch displacement of 1 mm was observed in region 3. The large displacement in region 3 was mainly due to superplastic deformation in the supercooled region. Viscosity of the amorphous alloys decreases by approximately 10^6 Pas from glass transition temperature to crystallization temperature [3]. The superplastic deformation was observed for all the samples sintered from 570 °C to 800 °C. Diffusion kinetics also increases in the supercooled liquid region which plays a major role in fast densification. During diffusion studies in the supercooled region a kink in the Arrhenius plot was reported near the glass transition temperature which may be due to a change in the diffusion kinetics. Below the

kink temperature, the diffusion is assumed to be through single atom hopping, whereas above the glass transition temperature, the collective atom diffusion becomes predominant resulting in an increase in diffusion rate [78]. This may result in higher mass transport through the necks of the amorphous powder in the supercooled region; hence, faster densification can be attained.

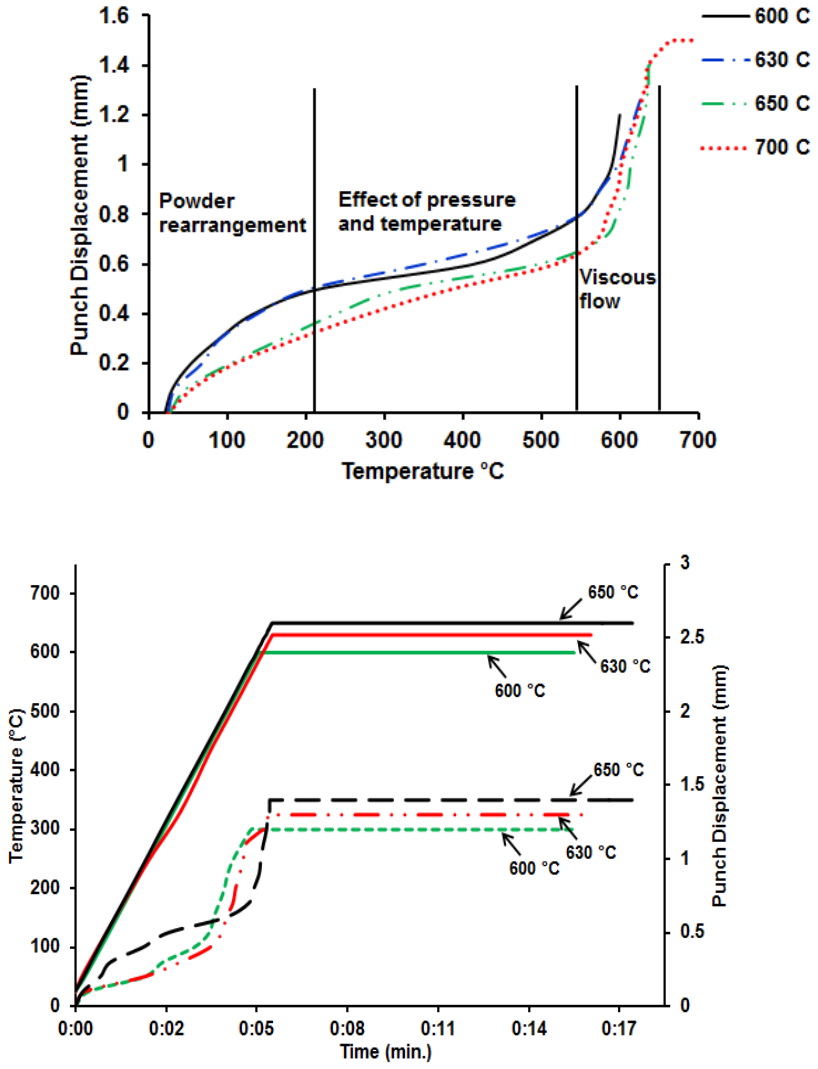

Fig.4.13 a) Punch displacement vs. sintering temperature for the samples sintered at 550, 600, 630, 650, and 700 °C; and b) temperature and punch displacement vs. time for the samples sintered in the supercooled region.

Higher mass transport through diffusion is also enhanced by the presence of the direct current on the surface of amorphous powders during SPS sintering [79, 80]. In order to evaluate any punch displacement during soaking time, temperature and punch displacement were plotted against time (Fig. 4.13 b). Punch displacement of 1.2 mm, 1.3 mm, and 1.4 mm were observed for the samples sintered at 600, 630, and 650 °C at the end of the heating cycle. No punch displacement was observed during soaking time in any of the sintering temperatures. It is to be noted that any displacement less than 100 μm cannot be recorded due to the limited resolution of the equipment. Even during the soaking cycle the samples were in supercooled region where viscosity of the amorphous alloys was less but no punch displacement was observed. This clearly indicates that heating rate and change in uniaxial pressure are the two driving forces which lead to faster densification.

Fig. 4.14 shows SEM images of fractured surfaces of samples sintered at different temperatures ranging from 570 ºC to 800 ºC. At 570 ºC the powders were densely packed and smaller size particles (< 20 μm) filled the space between the bigger particles (40 to 100 μm). Particle boundaries are clearly observed up to 600 ºC; thereafter an increase in sintering temperature resulted in the absence of particle boundaries and the removal of pores. Large deformation of the amorphous powders in the supercooled region was observed due to viscous flow of the amorphous alloy. Samples sintered at 650 ºC and above show a fully dense microstructure. Sintering in the supercooled region is also advantageous as amorphous powders undergo homogeneous deformation when compared to inhomogeneous deformation below T_g.

In summary, spark plasma sintering of Fe-based amorphous alloys in the supercooled region (630 ºC) resulted in near full densification of alloys (98.5% relative density). An increase in sintering temperature resulted in an increase in the density of the bulk sample. A decrease in viscosity during SPS sintering helps in attaining faster densification where most of the densification was achieved in the supercooled region.

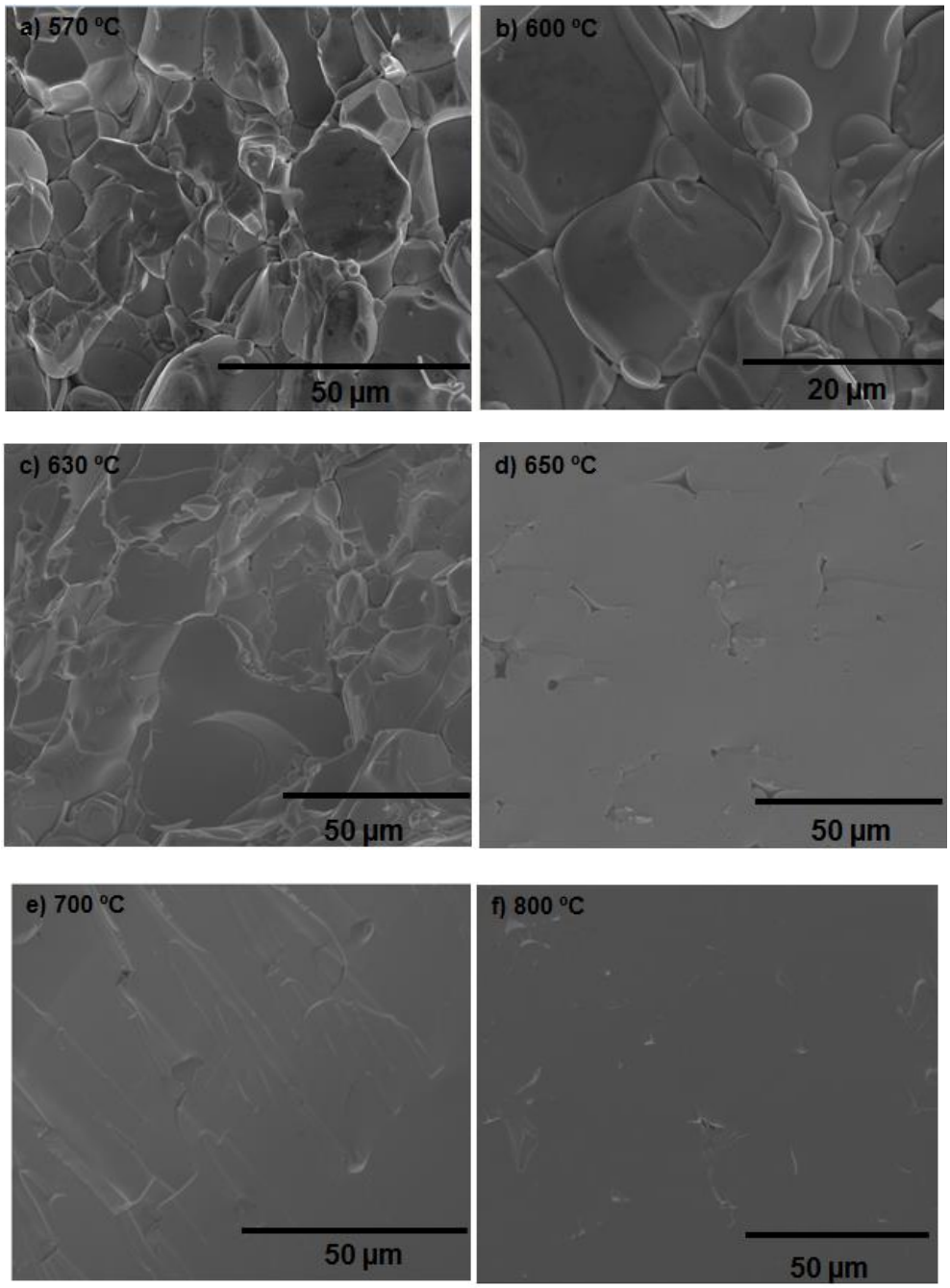

Fig.4.14 SEM micrographs of fractured surface of SPS sintered Fe-based bulk amorphous alloys.

4.3.2 Thermal effects during processing of bulk amorphous alloys

In order to better understand the SPS sintering and densification mechanisms of Fe-based bulk amorphous alloys, it is crucial to investigate the distribution of temperature inside the particles and at the point of contact between the particles. Song *et al.* proposed an analytical model for the determination of temperature along the radius of the particles based on energy conservation between electrical energy passed through the particle and the heat generated due to joule heating [23]. An equivalent model was applied to the SPS sintering of Fe-based amorphous alloys and sintering mechanisms were explained based on the modelling results. Total current passing through the upper punch is denoted as I_t. This current is further divided between the graphite die (I_d) and the amorphous alloy sample (I_s) based on the resistance. Therefore,

$$I_s = \frac{R_s}{R_s + R_d} I_t \tag{4.1}$$

R_s and R_d are the resistance of the sample and the die which can be calculated as

$$R_s = \rho_s \frac{x_s}{A_s} \tag{4.2}$$

$$R_s = \rho_d \frac{x_d}{A_d} \tag{4.3}$$

Here A_s and A_d are the area of the sample and the die. x_s and x_d are the thickness of the sample and the die. x_s can be obtained from the punch displacement data and the final

thickness of the sample. ρ_s and ρ_d are the resistivity of the sample and the die. I_p is the current passing through the particles and can be obtained using the following equation:

$$I_p = \frac{r_p^2}{r_d^2} I_s \tag{4.4}$$

I_s is the current passing through the bulk sample, and r_p, and r_d are the radii of the amorphous particles and sintered sample, respectively.

The electrical resistivity *(ρ)* for graphite is 1.4 x 10^{-5} Ω-m. Resistivity of the sample remains low at the start of the sintering process and increases with an increase in density of the sample. Variation in resistivity of graphite and the amorphous alloys with temperature and density is neglected in this analysis. Using law of conservation of energy, heat generated at the point of contact of the two particles is equal to the electrical energy due to the passage of direct current through the point of contact as shown in equation 4.5.

$$I_p^2 dR\Delta t = C_v dV\Delta T \tag{4.5}$$

Here C_v = 39.12 J/Kmol is the heat capacity, ρ_m = 7.5 g/cm^3 is the mass density, and ΔT = rise in temperature. As derived by Song *et al*., temperature increase of any particle is given by equation 4.6.

$$\Delta T = \frac{16}{\pi^2} \frac{I_p^2 \rho \Delta t}{C_v \rho_m ((r^2 - (r-x)^2))^2} \tag{4.6}$$

Here, r is the particle radius and x is any distance from the surface of the particle.

Fig. 4.15 (a) presents temperature distribution at different direct current magnitudes. As the magnitude of the current increases, temperature at the point of contact

of the particles increases. An increase in temperature at the point of contact with an increase in direct current represents the heating stage in SPS cycle. Fig 4.15 (b) presents temperature distribution inside a particle at a current magnitude of 800 A. Larger size particles draw higher magnitude of current due to their larger surface area and higher magnitude of current passes through a point of contact resulting in high current density at the point of contact and hence high temperature. Fig. 4.15 (c) presents a plot of temperatures at different distances from the contacting surface of the particle at a current magnitude of 800 A for a particle size of 40 μm. A temperature of 650 ºC was calculated at 1 μm away from the point of contact of two particles whereas a temperature of less than 100 ºC was observed at the center of the particle. Temperature drops from 650 ºC to less than 100 ºC within 2.5 μm from the surface of the particle. When current passes through the particles in contact, the temperature at the contacts increases to the supercooled region (570 ºC to 653 ºC), then crystallization temperature (653 ºC) and finally melting (1135 ºC) takes place. As the temperature at the point of contact of two amorphous particles reaches above glass transition temperature, viscosity at the contacts decreases by several thousand degrees. This decrease in viscosity results in localized flow of amorphous particles which increases the overall point of contact between the particles. Increase in point of contact is dynamic in nature and keeps increasing with the sintering time. Several impingement/dimples were observed on the particle surface on the SEM image of samples sintered at 570 °C (Fig. 4.16). It is to be noted that superplastic deformation in the amorphous alloys starts well below the glass transition temperature ($0.7T_g$). Multiple impingements on the single particle indicate multiple points of contact between particles during sintering.

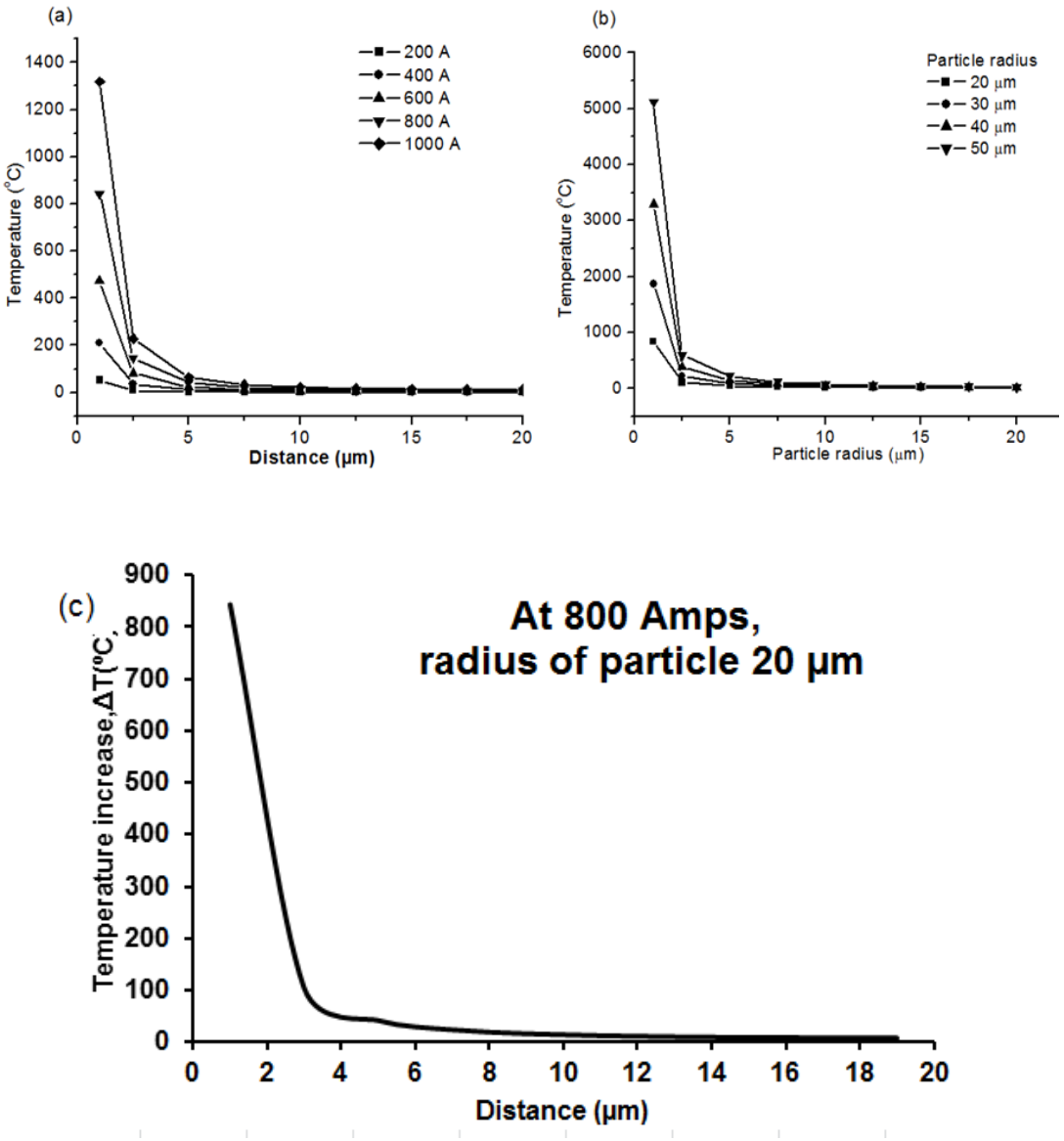

Fig.4.15 a) Effect of different current magnitudes on the temperature distribution in a particle, b) Effect of different particle size on temperature distribution in an amorphous particle, c) Temperature distribution from the outer edge towards the center at a current of 800 A and particle size of 40 μm during SPS of Fe-based amorphous powder.

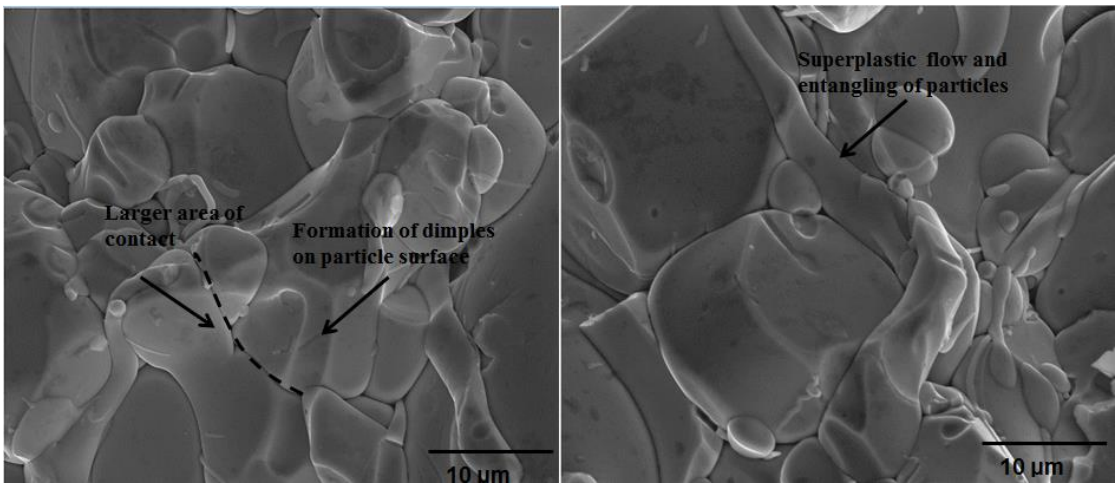

Fig.4.16 Fracture surfaces of the Fe-based bulk amorphous alloys sintered at 570 °C.

Some of the particles show excessive superplastic deformation mainly due to an increase in points of contact of particles during sintering. Free flow and entangling of some particles show a decrease in the viscosity of the amorphous alloys. Amorphous alloy powders undergo superplastic deformation before melting. This increase in deformation increases the area of contact between two particles which results in homogenous distribution of current during sintering [23]. Yodoshi *et al.* investigated spark plasma sintering of Fe-based bulk amorphous alloys and performed TEM on the interface of the sintered particles. A crystallized phase of 50 nm was observed at the interface and the core of the particles remained amorphous. This observation clearly indicates higher temperature at the interface of the particle whereas the core of the particle remained below crystallization temperature during SPS sintering [81]. As shown by Song *et al.*, in the case of metallic crystalline alloys, sintering mechanisms involved localized melting and the formation of necks at the point of contact. The size of these necks increased with the increase in sintering time. Whereas in the case of amorphous

alloys, when the point of contact between two particles reaches above T_g, free flow of material occurs which results in an increase in area of contact. Also in the supercooled region, collective hopping based diffusion of atoms takes place between two particles which results in sintering at a higher rate [79, 80].

Fig. 4.17 presents temperature profile of the axisymmetric sample and die-punch set up during SPS sintering. A temperature ranging between 27 ºC to 200 ºC was observed at the upper and bottom graphite rams; spacers reached a temperature between 200 ºC to 400 ºC for a current of 700 A. As the cross-sectional area decreases between spacers and the punch, current density increases thus resulting in higher temperatures at the punch. The highest temperature of 651.4 ºC was observed on the upper punch just below the center of the punch. Similar trends were observed for all different magnitudes of current ranging from 550 A to 900 A.

Fig 4.18 presents temperature distribution for the Fe-based sintered amorphous alloy sample with a current of 700 A. Maximum temperature was observed at the surface center of the sample whereas, minimum temperature was observed at the center of the edge. Similar trends were observed for different current magnitudes ranging from 550 A to 900 A. A temperature difference of 12 ºC was observed between the center and the edge of the sample, whereas a temperature difference of 2 ºC was observed along the axial direction. In order to evaluate the temperature difference between the center and edge of the sample, thermal modeling was performed at different current magnitudes ranging from 550 A to 900 A. The difference between the center and the edge is plotted in Fig. 4.19. In the supercooled region (575 °C to 653 °C) of Fe-based bulk amorphous alloys, a temperature difference of 8 to 12 °C was observed. It is to be noted that

temperature difference in the sample is a function of sintering temperature, heating rate, and also the electrical and thermal conductivity of the material. High sintering temperature and high heating rates for non-conductive materials lead to larger temperature difference [27, 82-84]. Wang *et al.* demonstrated that the temperature between the center of the sample, edge of the sample, and the die can be as high as 450 °C at a sintering temperature of 1700 °C.

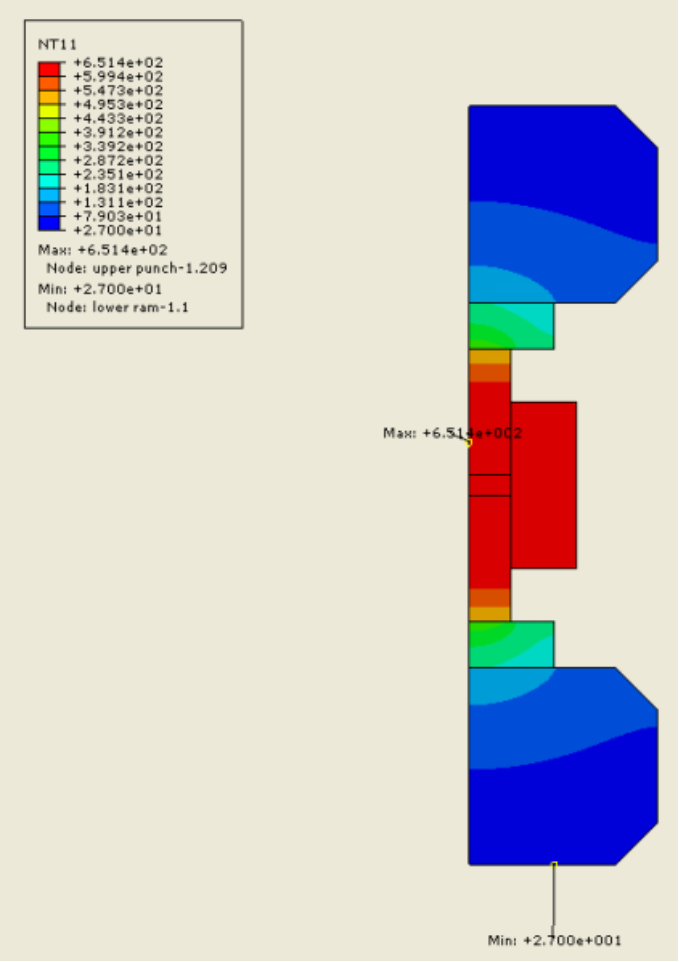

Fig.4.17 Temperature distribution during SPS sintering of Fe-based bulk amorphous alloys.

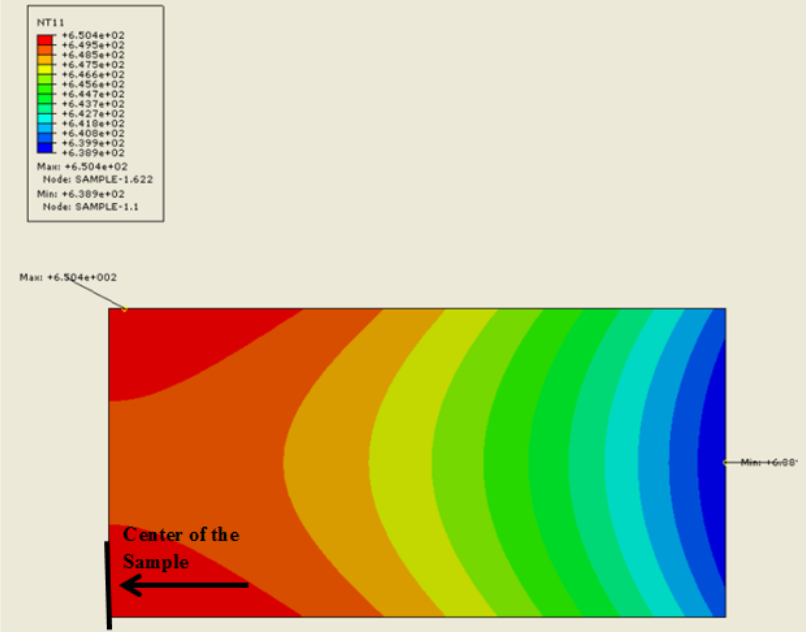

Fig.4.18 Temperature distribution inside the Fe-based bulk amorphous alloy disc during SPS sintering with a current of 700 A.

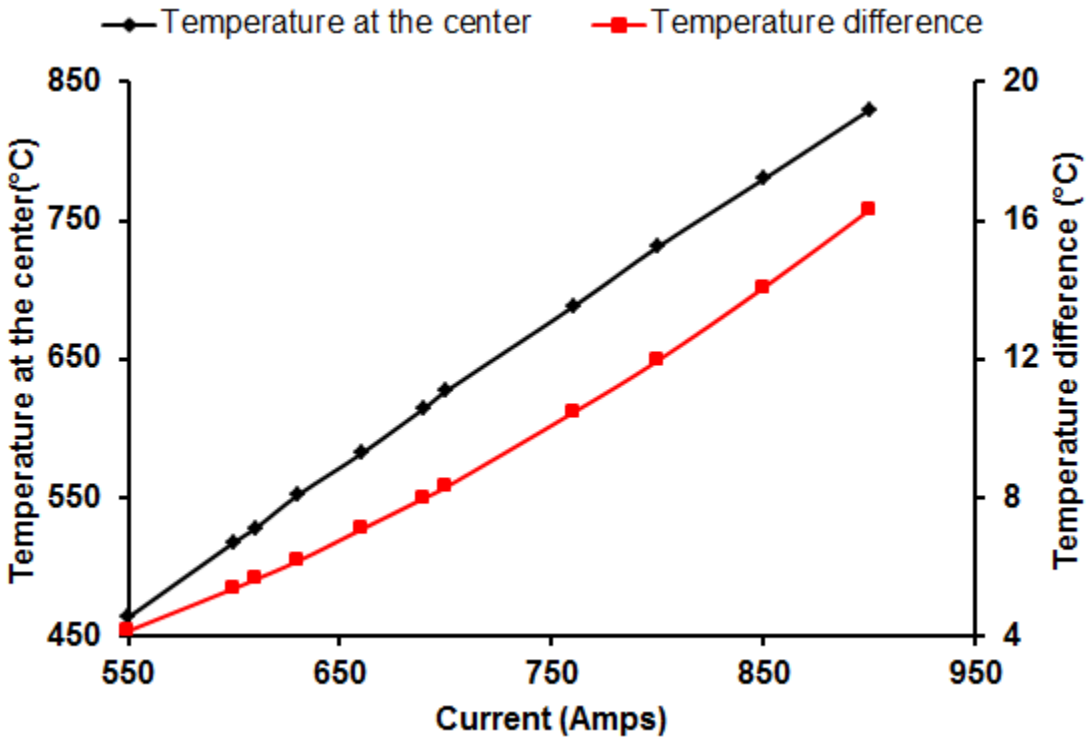

Fig.4.19 Effect of different current magnitudes on temperature at the center and temperature difference between center and edge of the amorphous samples.

It is interesting to correlate the temperature difference and the microstructural and phase transformation behavior of the sintered amorphous alloy samples. Micro XRD analysis was carried out along the diameter of the sintered discs for the samples sintered at 600 ºC, 630 ºC, 650 ºC, and 700 ºC (Fig 4.20). XRD analysis was performed at three different locations: (1) at the center, (2) at 4.5 mm away from the center, and (3) at the edge of the sample (9 mm away from the center).

For the sample sintered at 600 ºC and 630 ºC crystalline peaks were observed at the center and at 4.5 mm away from the center. No crystalline peaks were observed at the edge of the disc for either 600 ºC or 630 ºC. This can be explained using the temperature distribution along the sample as shown in Fig 18. . For the samples sintered at 650 ºC and 700 ºC, no such differences in XRD results were observed.

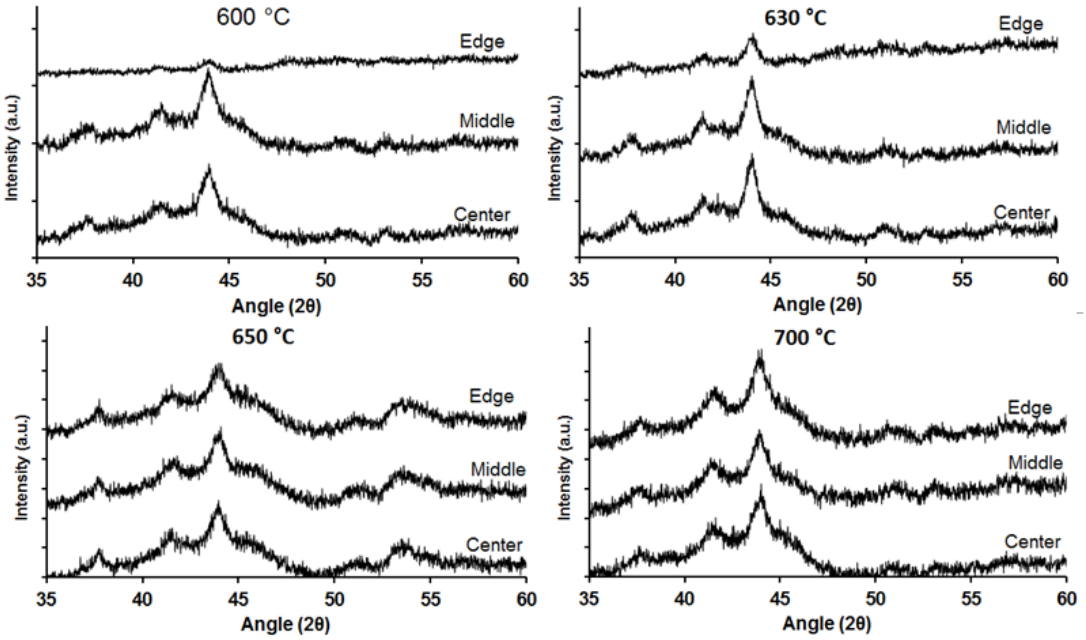

Fig.4.20 Micro XRD of Fe-based bulk amorphous alloys at three different locations (center, middle, and edge) of the SPS sintered discs at 600 °C, 630 °C, 650 °C, and 700 °C.

It is to be noted that during the SPS process temperature is measured at the center of the die. As shown in the simulation results, the difference between the temperature at the outer edge and at the center of the sample can be up to 40 ºC. This is further confirmed by the micro XRD results. The outer edge of the sample is amorphous as the temperature in that region was close to 600 ºC. For the sample sintered at 650 ºC and 700 ºC no such difference in micro XRD data was observed, as shown in the Fig. 4.20. As the thermocouple measured 650 °C, every position in the sample was above 650 °C. So throughout the sample, temperature was above crystallization temperature (both at the edge and at the center).

The effects of temperature gradient during SPS sintering on the microstructure were investigated using microscopic images of the mirror polished sintered samples. SEM images were taken at the center, 3 mm, 6 mm, and 9 mm away from the center of the sintered samples (Fig. 4.21). For the sample sintered at 600 ºC, the image at the center showed less porosity when compared to other regions of the sample. Porosity gradually increased from the center towards the edge of the sample when observed radially. At the edge of the sample, pores of size ~100 μm were also observed, whereas at the center of the sample pore sizes were ~10 μm. Similar observations were also made for the samples sintered at 630 ºC. Maximum size of the pores decreased to ~50 μm at the edge of the sample and less than ~10 μm at the center of the sample. For the samples sintered at 650 ºC, there was no significant difference between the center and edge microstructure. Additionally, few pores of less than 10 μm were observed at the edge of the sample sintered at 650 ºC, whereas no pores were observed at the center of the sample. In case of sintering temperature of 630 ºC, the temperature at the edge of the samples was at 630 ºC

but at the center it was close to the crystallization temperature. This difference in temperature results in higher hardness at the center and lower hardness at the edge of the samples. For all the sintered samples, maximum hardness was observed at the center of the sample and minimum hardness at the edge of the samples.

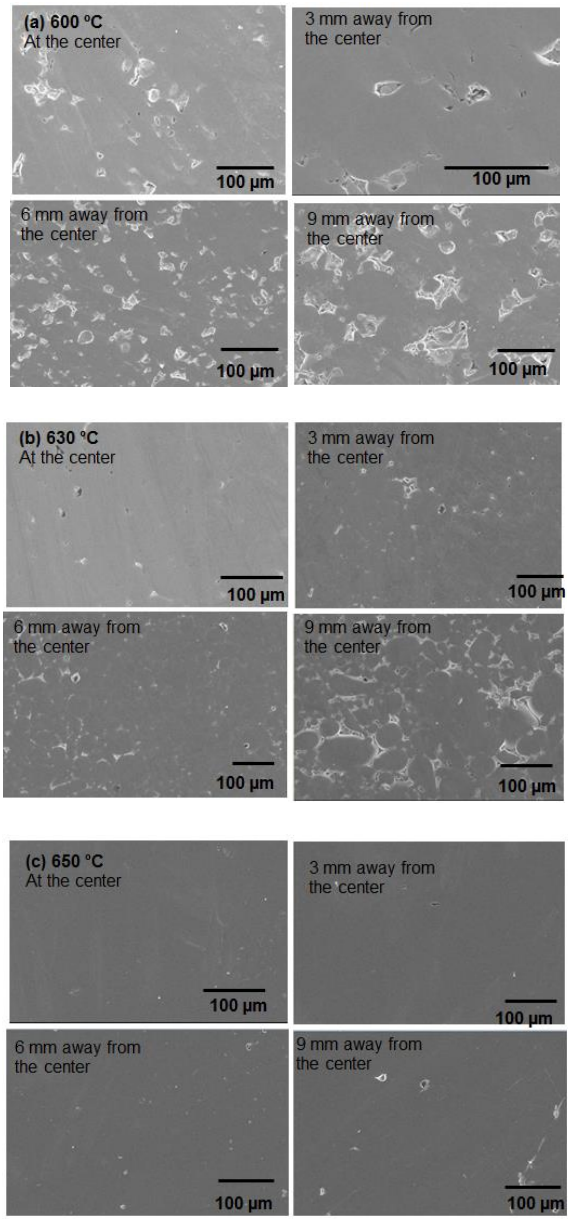

Fig.4.21 SEM images of Fe-based bulk amorphous alloys sintered at 600 °C, 630 °C, and 650 °C at different locations along the radius of the sample.

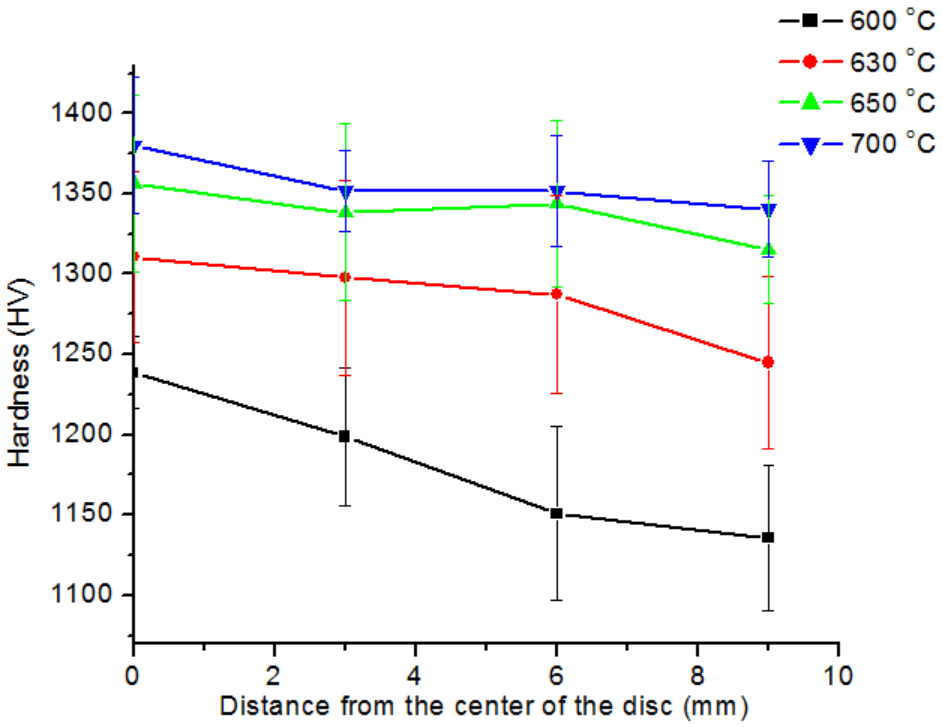

Fig.4.22 Microhardness of the SPS sintered Fe-based bulk amorphous alloys at different distance from the center of the disc.

The hardness values are in good agreement with the modeling and phase analysis results. Maizza *et al.* investigated hardness along SPS sintered WC samples at three different sintering temperatures. At lower sintering temperatures, higher hardness was observed at the center due to the small size of the nanoparticles. Whereas at the outer surface of the sample lower hardness was observed mainly due to lower density at the surface when compared to the center of the sample. At high sintering temperatures hardness was low at the center due to high grain growth and higher at the edge due to lower grain size. Thus, temperature gradients along the sample can introduce subtle microstructural effects that results in significant variation in mechanical properties [85].

4.3.3 Crystallization behavior of Fe-based amorphous alloys

4.3.3.1 Phase analysis using x-ray diffraction

The glass transition temperature (T_g), first crystallization temperature ((T_{x1}), and second crystallization temperature (T_{x2}) of the Fe-based amorphous alloy used in this investigation are 575 °C, 653 °C, and 684 °C, respectively. The wider supercooled region (ΔT= 78°C) indicates the excellent glass forming ability of this composition of the Fe-based amorphous alloy. Fig. 4.23 shows the XRD patterns from as-received amorphous powder and bulk amorphous alloy samples spark plasma sintered at temperatures ranging from 570 °C to 800 °C (with uniaxial sintering pressure of 70 MPa and a holding time of 10 min.). Although, in general, the characteristic halo peak was observed in the XRD spectra from samples sintered up to 630 °C, TEM analysis was performed to explore any possibility of formation of nano-scale crystalline phases in any of these samples (discussed in further details in the later section). The presence of such a halo peak is indicative of retention of mostly an amorphous structure of the samples sintered up to a temperature of 630 °C, which is relatively lower than the reported primary crystallization temperature (T_{x1}, 653°C) of the amorphous alloy [49]. Profuse crystallization with the formation of complex $(Fe,Cr)_{23}C_6$ carbides was observed for samples sintered in the temperature range of 650-800 °C. The crystalline phase $(Fe,Cr)_{23}C_6$ belongs to a cubic crystal system (a: 10.5910 Å, space group: Fm-3m, space group number: 225, and density: 7.48 g/cm^3) [86]. The calculations performed using the Scherer equation indicated that estimated crystallite size increased from ~8 nm at 650 °C to ~12 nm at 800 ºC sintering temperatures.

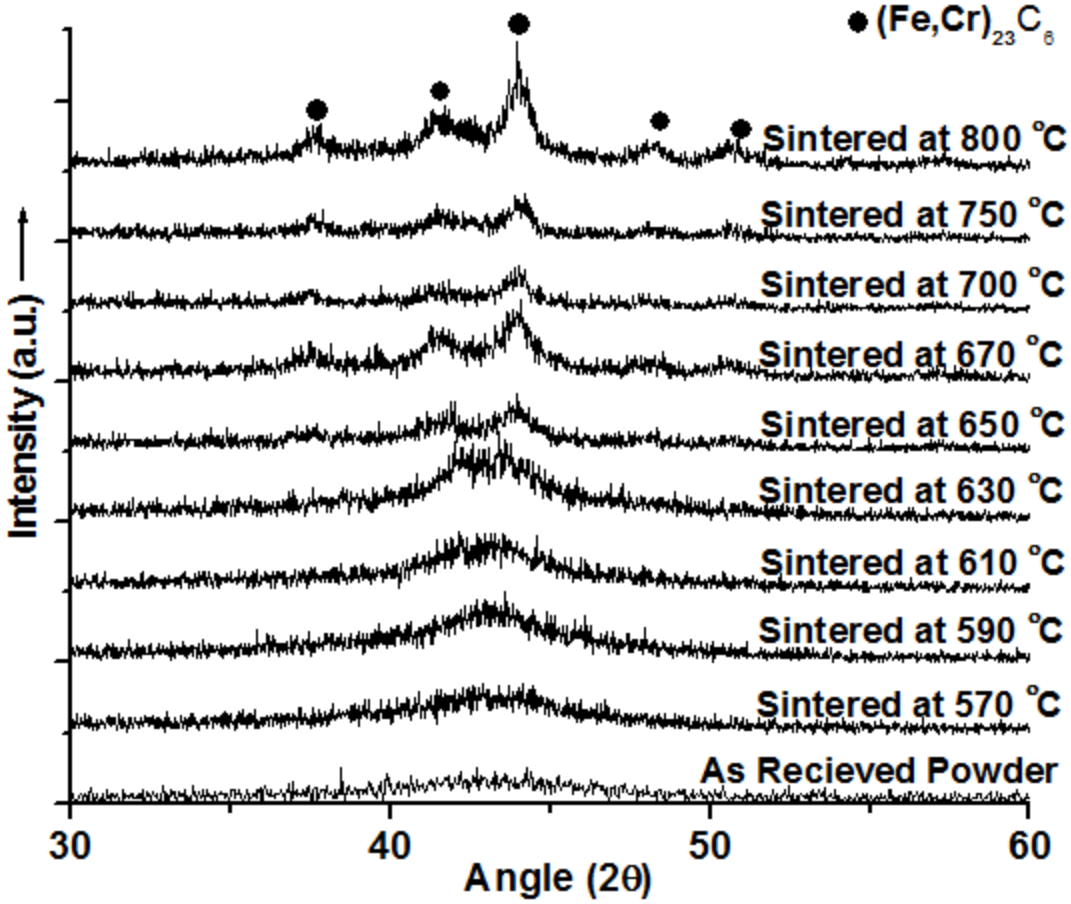

Fig.4.23 XRD patterns from Fe-based amorphous alloys sintered at temperatures ranging from 570 °C to 800 °C at 70 MPa for a soaking time of 10 min. [87].

4.3.3.2 Crystallite size distribution using small angle neutron scattering

To further understand the crystallization path and crystallite size distribution, SANS experiments were conducted. Fig. 4.24 shows EQ-SANS results for as-received powder and Fe-based bulk amorphous samples (sintered at temperatures ranging from 570 to 800 °C) in a log-log plot of scattering intensity, *I(Q)*, as a function of scattering vector, *Q*.

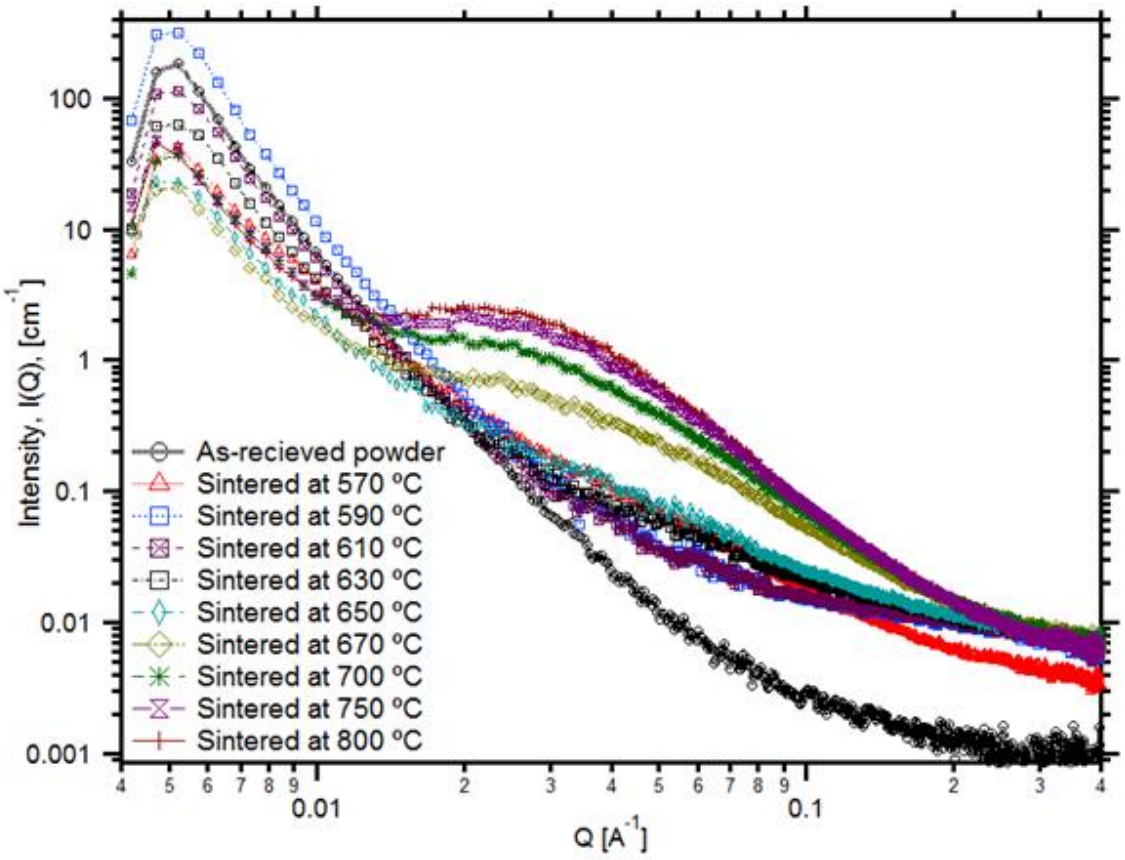

Fig.4.24 EQ-SANS intensity data of Fe-based amorphous powder, sample sintered at temperatures ranging from 570 °C to 800 °C at 70 MPa for 10 min. [87].

In the higher Q-range (0.2-0.4 Å^{-1}), the scattering was mainly observed due to chemical inhomogeneities at the atomic scale. The scattering intensity increased for the sample sintered at 570 °C and 590 °C and thereafter it remained constant. Hung *et al.* has previously observed chemical inhomogeneities (clustering of Y and Mo elements) in the fully amorphous Fe-based alloy [88]. The inhomogeneities due to clustering of elements are possible during SPS sintering of Fe-based amorphous alloys below crystallization temperature. In the Q-range of 0.02-0.2 Å^{-1}, very low scattering intensity was observed for the as-received amorphous powder indicating uniform glassy structure, which is in good agreement with the XRD results. An increase in scattering intensity *I(Q)* was observed for the samples sintered in the temperature range of 570-650 °C, even though

these temperatures are below the crystallization temperature. The scattering below the crystallization temperature is mainly due to the nucleation and growth of clusters in the supercooled region. The formation of short- or medium-range nano-sized clusters in the supercooled region of metallic glasses has previously been observed during thermal annealing [89]. The scattering in the temperature range of 590 °C to 630 °C indicates that stable clusters are formed in this temperature range. These stable clusters of critical size eventually transform into crystallites as sintering temperature reaches T_{x1}. On the contrary, in spite of the observance of recognizable scattering in EQ-SANS data as stated earlier, the XRD analysis (Fig. 4.23), due to its inferior resolution, indicated the presence of halo peak for samples annealed up to 630°C that is associated mostly with the amorphous nature. Similar observations were made by Tang *et al.*, where interference peaks were formed in the scattering data and no crystallization was observed in the XRD pattern [78]. Hung *et al.* also observed the characteristic signature (halo peak) in the XRD patterns of the Fe-based amorphous alloys annealed at a temperature of 600 °C, (*i.e.*, annealing temperature well below the crystallization temperature of 653 °C) while the crystallites of size less than 10 nm were observed in the TEM [88]. Nouri *et al.* also observed the presence of nanocrystallites (size less than 10 nm) using *in situ* TEM at temperatures well below the crystallization temperature [90].

The scattering intensity begins increasing significantly from the sample sintered at 650 °C and become significant for the samples sintered at and above 670 °C, indicating the formation of crystallites near and above the crystallization temperature (653°C). The interference maximum in the Q-range of 0.015 to 0.1 is due to the formation of $(Fe,Cr)_{23}C_6$ crystallites. In this temperature range (670 °C to 800 °C), the scattering

intensity increases faster at lower temperatures (near first crystallization temperature $T_{x1,}$ 653°C) and then slows down as the temperature increases above the second crystallization temperature (T_{x2} at 683 °C). Such reduction in crystallization growth rate can also be attributed to annihilation of free volume that will have an effect on the diffusion [79]. These trends are common in evolution studies of metallic glasses where spinodal decompositions were observed and crystallization growth rate decreases significantly after initial rapid growth. [91]. A shift of the maximum interference scattering intensity towards the lower Q-range is an indication of a change in composition and increase in crystallite size associated with the crystallization of the second phase at temperatures above T_{x1}. Often times for bulk metallic glasses, phase separation precedes crystallization [78]. For those cases, interference maximum was formed below crystallization temperatures [58, 59]. The phase separation was not observed in the supercooled region for this composition as no interference maximum was observed before crystallization temperature (T_{x1}). The mechanism for crystallization seems to be primary crystallization, where a crystalline phase is formed directly from the amorphous matrix. The $M_{23}(C,B)_6$ phase has also been identified as the principal phase in early stage crystallization during thermal annealing [48, 88]. This is primarily due to similar metals-to-metalloid ratios for the $M_{23}(CB)_6$ phase [23/6=3.833] and the overall amorphous alloy composition [79/21=3.762].

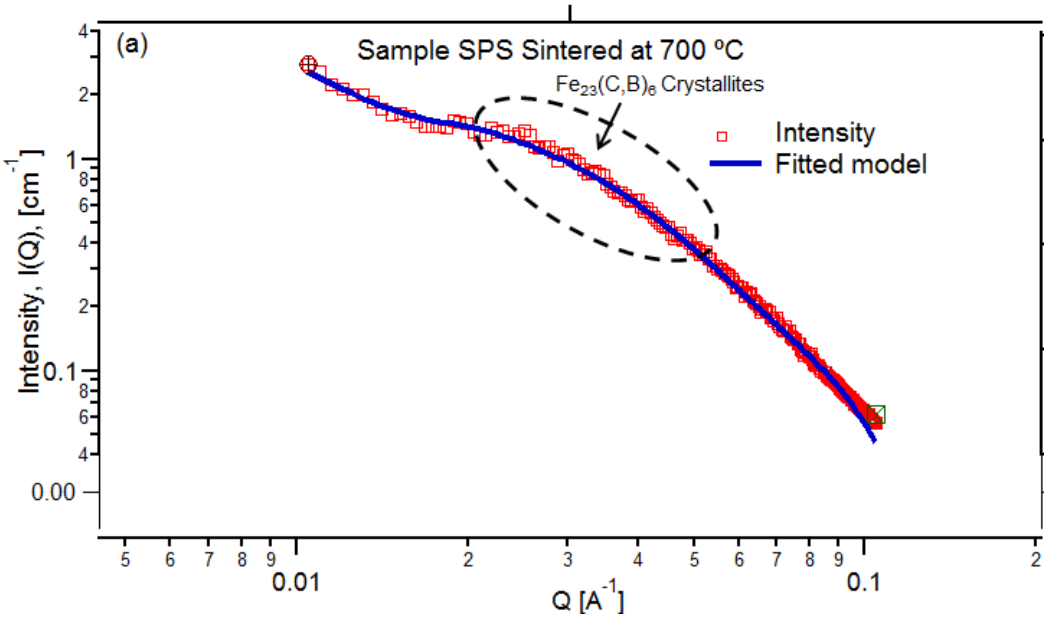

Fig.4.25 Measured and fitted absolute intensities of Fe-based bulk amorphous alloys sintered at 700 °C [87].

The size distribution analysis was performed in the Q-range of 0.02-02 $Å^{-1}$ using the maximum entropy method available in IRENA software [71]. Fig. 4.25 shows the intensity of the measured data for the sample sintered at 700 °C and computational results indicate a good fit with the experimental data. In order to calculate scattering contrast, the amorphous phase was considered as a matrix and $(Fe,Cr)_{23}C_6$ as particles. Fig. 4.26 presents the particle volume distribution for the samples sintered at temperatures ranging from 590 °C to 800 °C. The cluster size in the samples sintered at 590 °C was up to 16 nm with clusters of size 4 nm present in abundance. These clusters are mainly the local structural/compositional changes which eventually grow into crystallites. The volume fraction of clusters increases with increasing sintering temperature up to 630 °C without change in their size distribution. The clusters of size 1 to 5 nm have previously been reported in metallic glasses near glass transition temperature [92].

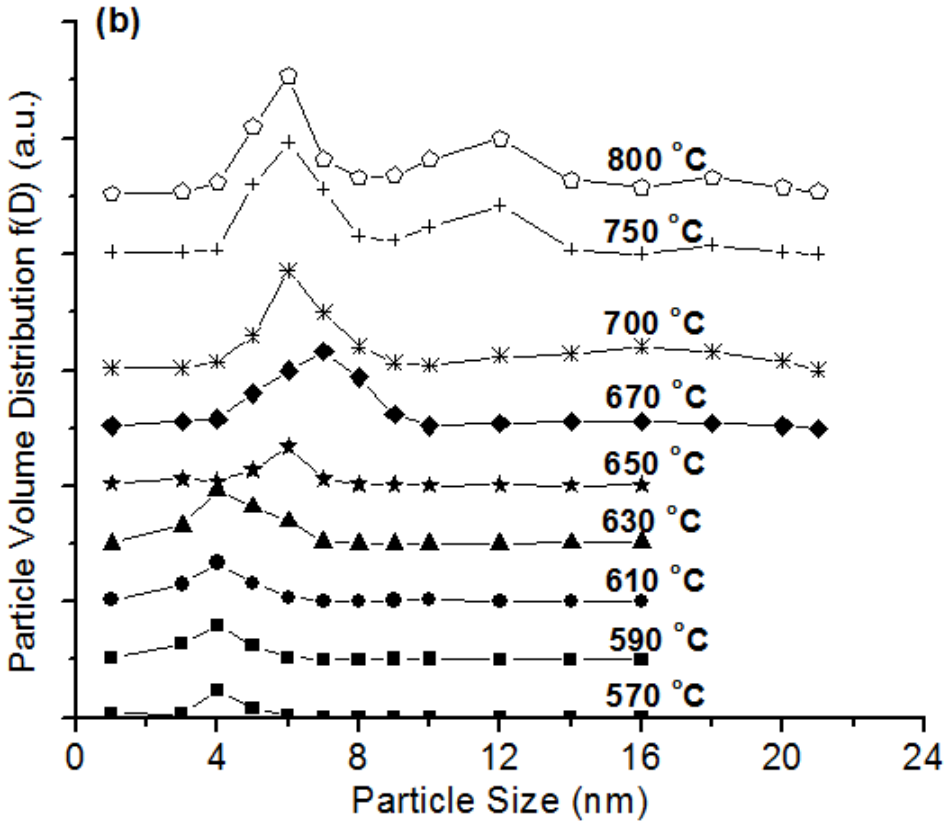

Fig.4.26 Particle size distribution of crystallites of Fe-based amorphous alloys SPS sintered at different temperatures [87].

A shift in the peak of size distribution to 6 nm was observed for the sintering temperature of 650 °C without significant increase in volume fraction. This shift can be mainly due to the growth of these clusters into crystallites as the sintering temperature nears T_{x1}. Above 650 °C, the crystallite size distribution spreads up to 21 nm, and the volume fraction of 6 nm crystallites increases rapidly. The formation of nano-scale crystallites dispersed in amorphous matrix is mainly due to the primary crystallization for this amorphous composition. The crystallite growth during primary crystallization is governed by diffusion fields/concentration gradients around the crystalline phase, where the crystallite growth is reduced and eventually ceased by impingement of surrounding

concentration gradients [93]. This effect has been recognized as the soft impingement (SI) effect and is mainly due to the interaction between two or more concentration gradient fields which form due to change in the composition of the amorphous matrix composite after formation of nanocrystallites. Thus, the change in composition of the residual amorphous phase reduces the stability and these regions become prone to crystallization. This process leads to non-random nucleation (NRN), where more crystallites are formed near the existing crystallites. Such concentration gradients were also observed in crystallization studies performed by Hung *et al.* on Fe-based amorphous alloys where Cr depleted regions were observed near the formed crystallites [88]. A bimodal distribution of crystallite size was observed for the sintering temperature of 750 °C and 800 °C.

The bimodal distribution can be attributed to either simultaneous nucleation of new crystals and growth of existing nanocrystallites or the second crystallization event (T_{x2}, 683°C). Nevertheless, the observed bimodal distribution of crystallite size seems to be the direct effect of non-random nucleation (NRN) from the regions of concentration gradients. The scattering was also observed in the lower Q-range (0.004 $Å^{-1}$ to 0.02 $Å^{-1}$) which is mainly due to the formation of residual amorphous phases around the crystallites. In this Q-range, the scattering intensity decreased with an increase in sintering temperatures. Even though a regular trend was not observed in the SANS results, the scattering intensities of the samples sintered below crystallization temperature were higher than that for the samples sintered above crystallization temperature. This indicates that the number and size distribution of these residual amorphous phases tends to diminish with an increase in crystallites' size at higher sintering temperatures [88].

Extensive efforts are required to model and characterize the size distribution of these residual amorphous phases for multi-component amorphous alloys, for which the major challenge is to determine the composition of the residual amorphous phases surrounding nanocrystallites. Imhoff *et al.* modeled such a residual amorphous phase of binary Al-Sm metallic glass after precipitation of Al nanoparticles using small angle x-ray scattering [94].

4.3.3.3 Transmission electron microscopy

The observations and explanations associated the XRD and EQ-SANS analyses are further complemented by TEM analysis. The TEM images of the samples sintered at 570°C, 650 °C, 700 °C, and 800 ºC are presented in Fig. 4.27. The samples sintered at 570 °C (Fig. 4.27 a) indicate the formation of the nanocrystallined phase with crystallite size of approximately 6 nm (indicated for one of the crystallites in the micrograph). The size of the nanocrystallined phase is in agreement with the crystallite size predicted by SANS results (6 nm). Furthermore, the selected area diffraction (SAD) analysis indicated the formation of $(Fe,Cr_{23})C_{6.}$ A contrast in the bright field imaging is mainly due to diffraction contrast; the darker regions are observed due to the diffraction of the electron beam as imaging was done in the direct beam mode. When sintered at 650 ºC, these clusters develop into well-formed crystallites as observed in the Fig. 4.27 (b). A ring pattern from the TEM-SAD pattern confirmed the formation of the nanocrystallined phase $(Fe,Cr_{23})C_6$, and the corresponding micrograph shows the formation of crystals with a majority of crystallites in the range of 6-8 nm (Fig. 4.27 b), which is in agreement with the SANS data. A similar agreement is observed between the crystallite sizes for the

samples sintered at higher temperatures. However, the diffraction analysis for the samples sintered above the second crystallization temperature (700 °C and 800 °C) revealed the formation of α-Fe phase along with $(Fe,Cr_{23})C_6$. The TEM dark field image of sample sintered at 700 °C clearly indicated the formation of crystallite sizes in the range of 16 nm as highlighted in the micrograph (Fig. 4.27 c) that is in agreement with the SANS data. Nonetheless, it was difficult to isolate the phases in the dark field image as the high intensity diffraction rings of Fe and $Cr_{23}C_6$ nearly overlap each other. Although similar phases were observed for the sample sintered at 800 °C, a clear change in crystallite size (>20 nm) can be observed from the TEM micrograph (Fig. 4.27 d) and also as indicated in the EQ-SANS results.

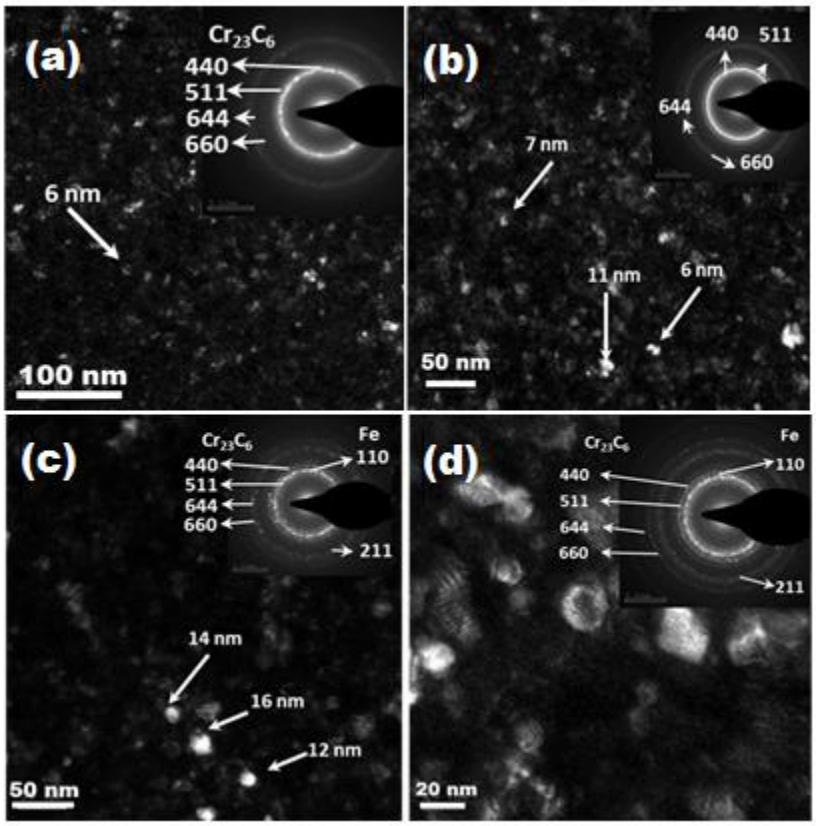

Fig.4.27 TEM images of SPS sintered samples at a) 570 ºC, b) 630 ºC, c) 650 ºC, and 800 ºC [87].

Earlier it was observed that the maximum interference scattering intensity shifted towards the lower Q-range for the samples sintered at temperatures higher than the second crystallization temperature, T_{x2} (Fig. 4.24), and this can be attributed to the formation of α-Fe phase indicated by the TEM-SAD pattern (Fig. 4.27 (c,d)). The depletion of Cr with the increase in volume fraction and growth of the precipitates seems to result in the variation in composition of the amorphous phase leading to the second crystallization event.

Bright field TEM micrographs of SPS sintered Fe-based bulk amorphous samples are presented in Fig. 4.28. Crystallites of size less than 10 nm were observed in the samples sintered at 570 ºC and 650 ºC and crystallites up to 25 nm were observed for the samples sintered at 800 °C.

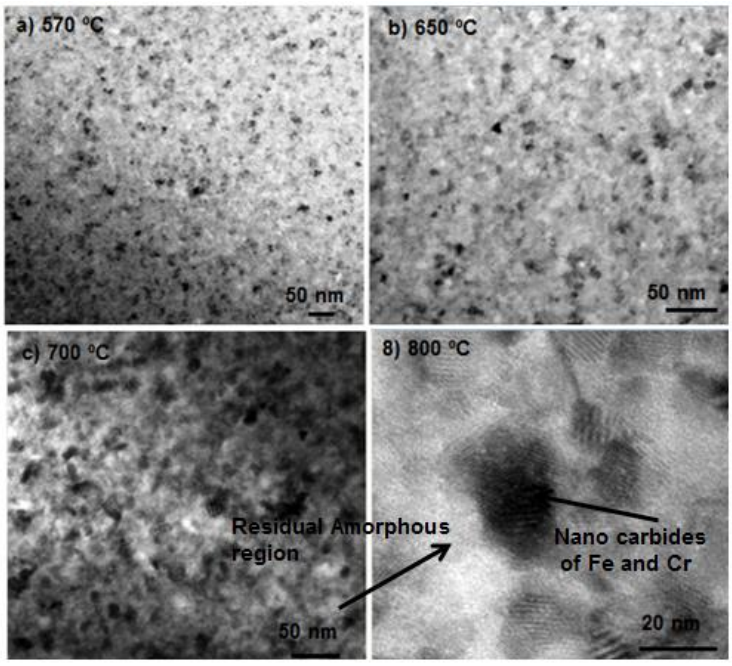

Fig.4.28 Bright field TEM images of SPS sintered Fe-based bulk amorphous alloys a) 570 ºC, b) 650 ºC, c) 700 ºC, and 800 ºC

For the samples sintered at 700 ºC and 800 ºC, crystal and an amorphous residual region around the crystals can be identified in the bright field TEM image. Similar element deficient amorphous regions were also observed by Nouri *et al.* and Ha *et al.* in the crystallization studies of Fe-based bulk amorphous alloys [88, 90].

4.3.4 Mechanical behavior

In order to evaluate the effects of densification and crystallization on mechanical strength of sintered Fe-based bulk amorphous alloys, microhardness and compression tests were performed (Fig. 4.29). Average microhardness of the sample sintered at 570 °C was 11.31±0.45 GPa. Microhardness increased with increase in sintering temperature mainly, due to embrittlement caused by the presence of nanocrystallites of Fe and Cr. Average microhardness of the sample sintered at 800 °C was 13.45±0.28 GPa. Increase in microhardness due to nanocrystallization was also observed in our previous investigation when sintered Fe-based amorphous alloys were annealed at 700 ºC and 800 ºC. Fig. 4.29 also presents the compressive strength of sintered Fe-based bulk amorphous alloys at different sintering temperatures. Compressive strength increased up to a sintering temperature of 630 °C and then decreased up to 800 °C. Enhanced compressive strength in the supercooled region was mainly due to the combined effect of increase in density and controlled nanocrystallization during SPS sintering. It is difficult to delineate the effect of density and crystallization in the strengthening of SPS sintered Fe-based amorphous alloys. Density of the sintered samples increased from 90 % to 98 % when sintering temperature was increased from 570 ºC to 630 ºC which played a significant

role in the enhancement of both microhardness and compressive strength. Formation of nanocrystallites was also evident from the XRD results and TEM images which grow in number and size with an increase in sintering temperature.

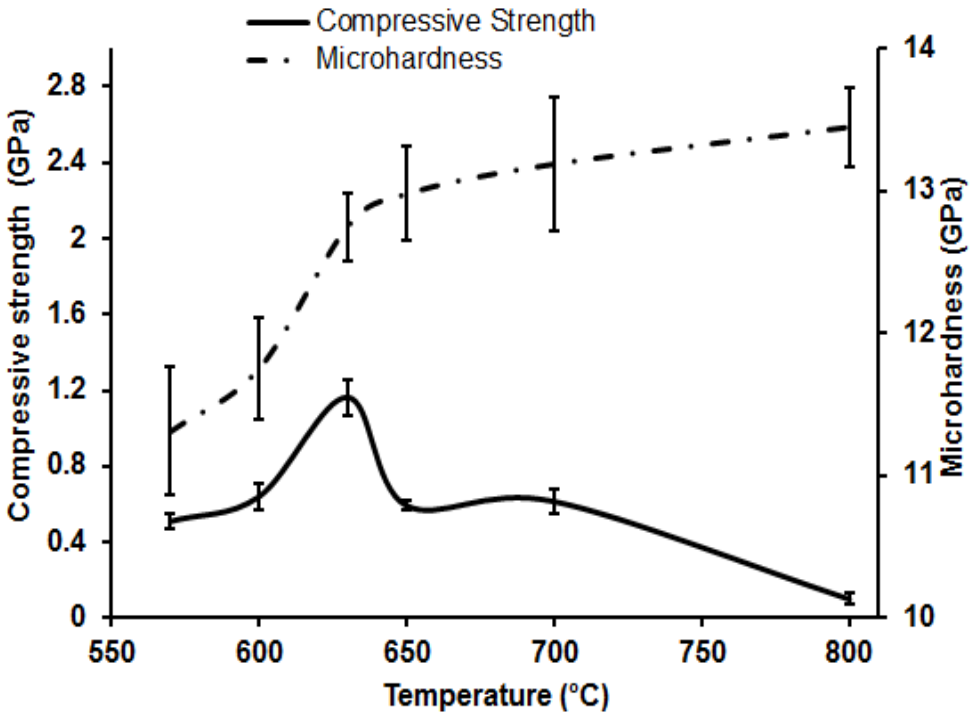

Fig.4.29 Comparison of microhardness and compressive strength of SPS sintered Fe-based bulk amorphous alloys.

Crystallite size as well as volume fraction of crystallite size play significant roles in the mechanical strength of Fe-based bulk amorphous alloys. Maximum compressive strength was observed when the peak of the size distribution was at 4 nm at 630 °C. A significant decrease in the compressive strength was observed when the size distribution peak shifted to 6 nm. Size distribution analysis and compression testing also indicates the possibility of having an optimum volume fraction of crystallites above which compressive strength decreases significantly.

Fig. 4.30 shows stress-strain curves of the Fe-based bulk amorphous alloys SPS sintered at 600 °C, 650 °C, 700 °C, and 800 °C. No plastic strain was observed during compression testing of the SPS sintered Fe-based bulk amorphous alloys at any sintering temperature. Even though the formed crystallites (< 25 nm) were in the same size range of shear bands (10-20 nm), it seems these nanocrystallites were ineffective in hindering the propagation of shear bands. A decrease in strength was observed for the samples sintered at 650 °C, 700 °C, and 800 °C, mainly due to weak interfacial bonding between the amorphous phase and the *in situ* formed crystallite $Fe_{23}(C, B)_6$. Our previous study indicated a nano scale element deficient region forms around the nanocrystallites in the Fe-based amorphous matrix when SPS sintering was performed above 630 °C [87]. These element deficient regions can play two significant roles during compression loading: (1) they can act as weak points where load cannot be effectively transferred to the *in situ* nanocrystalline reinforcement which can lead to stress concentration in the interfacial region and hence brittle failure, (2) when shear bands propagate through amorphous matrix they reach this elemental deficient region before reaching the nanocrystallites which can lead to the formation of cracks before the these shear bands are arrested by the nanocrystallites.

Step like behavior was observed in the stress strain curves for the samples sintered at 650 °C and 700 °C, which indicates crack arresting due to the presence of nanocrystallites. However, these nanocrystallites surrounded by elemental deficient regions were unable to induce any plastic strain during compressive loading.

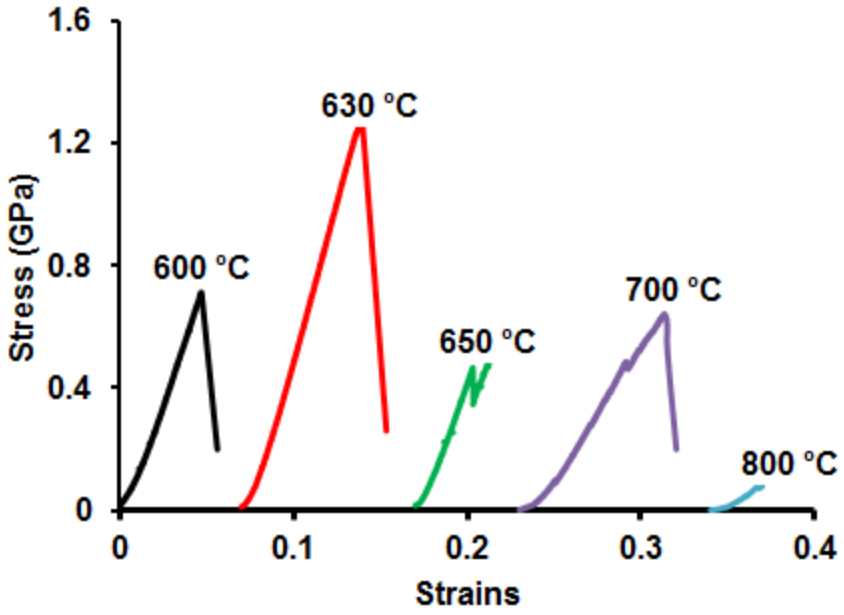

Fig.4.30 Stress strain curves obtained from SPS sintered Fe-based bulk amorphous alloys.

4.4 Effect of crystallization on tribological behavior of SPS sintered Fe-based bulk amorphous alloys

4.4.1 Phase analysis

XRD patterns from samples SPS sintered at 630 °C and samples annealed at two temperatures (700 and 800 °C) are presented in Fig. 4.31 The SPS sintered sample shows a broad halo peak with diffused intensity characteristic of amorphous alloys. No sharp peaks can be seen in the XRD pattern from sintered samples, indicating a fully amorphous structure without any crystalline phases. For the samples annealed at 700 and 800 °C, crystalline peaks of iron and chromium carbides can be clearly identified.

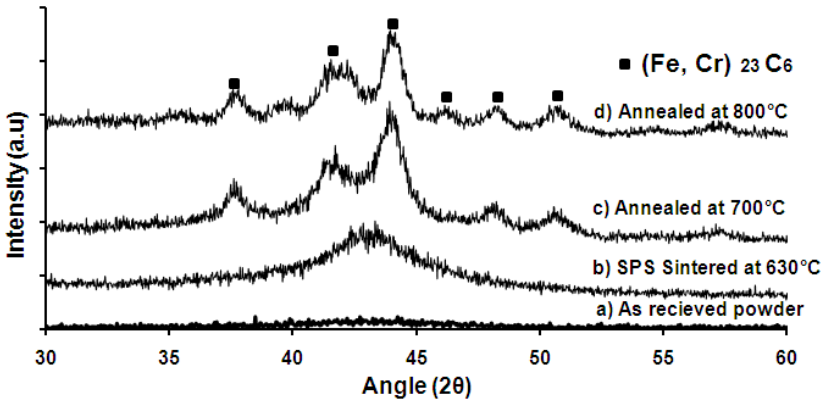

Fig.4.31 XRD of a) Fe-based BMG sintered at 630 °C, b) annealed at 700 °C for 20 min., c) annealed at 800 °C for 20 min.[48].

The crystallite size calculated from XRD peak broadening (using the Scherrer equation) for the samples annealed at 700 °C was found to be 15 nm. The crystallite size increased to 23 nm for the samples annealed at 800 °C. Clearly, annealing of SPS sintered Fe-based amorphous alloys above crystallization temperature resulted in the formation of a bulk amorphous matrix reinforced with nanocrystallined complex carbide phases.

The DSC traces from the starting amorphous powder, SPS sintered sample, and annealed sample are presented in Fig. 4.32. For the starting amorphous powder, glass transition temperature (T_g), crystallization onset temperature (T_x), and crystallization peak temperatures (T_{p1} and T_{p2}), can be clearly observed. Also, it can be seen that the first crystallization peak disappeared and the second crystallization peak shifted to a higher temperature after SPS sintering at 630 °C indicating partial crystallization. This crystallization event could not be detected by XRD which showed only broad diffused peak for the sintered samples. The crystallization proceeds further with annealing at 700 °C as indicated by a further shift of the second crystallization peak to higher temperatures.

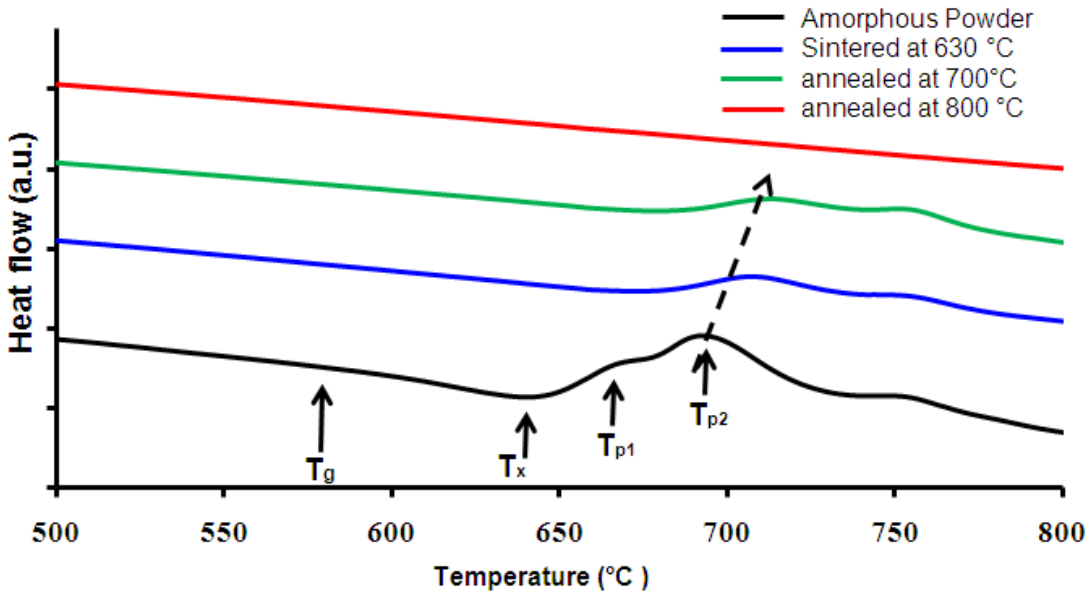

Fig.4.32 DSC of as-received powder, Fe-based BMG sintered at 630 °C, annealed at 700 °C for 20 min., annealed at 800 °C for 20 min. [48].

Both the primary and secondary crystallization peaks disappear after annealing at 800 °C, indicating profuse crystallization.

4.4.2 Microhardness

The variation of microhardness of SPS sintered and annealed samples as a function of indentation load is presented in Fig. 4.33. At lower indentation load, the microhardness of SPS sintered samples was about 1250-1350 HV. The annealed samples exhibited relatively higher hardness compared to sintered samples. At lower loads (<1 N), the microhardness of samples annealed at 700 and 800 °C were about 1375-1450 HV and 1450-1550 HV, respectively. The higher hardness of the annealed samples is primarily due to embrittlement caused by crystallization of complex carbide phases in the amorphous matrix during annealing. For all the samples, microhardness decreases with increasing indentation load (*i.e.*, increasing impression size). The hardness drops to about 1075-1200 HV for the indentation load of 9.8 N. Clearly, the SPS sintered samples and

annealed samples exhibit indentation size effects (ISE). According to concepts of continuum plasticity, in which there is no inherent material length scale, the hardness measured using geometrically self-similar indenters should be independent of impression size. However, the indentation size effects, where hardness decreases with increasing indentation depth, have been observed in several crystalline materials [95]. The earliest model to explain the ISE was proposed by Nix and Gao considering the density of geometrically necessary dislocations and Taylor's dislocation strengthening model[96]. The model was successfully used to predict the ISE in many crystalline materials. The observation of indentation size effects in the amorphous and partially crystalline samples in the present case cannot be explained using conventional theories based on dislocation strengthening. This is primarily due to unique deformation mechanisms involving shear bands which are localized regions of extensive plastic deformation in amorphous materials. While the ISE is well documented for crystalline materials, very few publications reported similar effects in bulk amorphous materials. Recently, Jang *et al.* summarized various mechanisms based on non-crystalline flow defects (shear bands, free volume), strain softening, and surface effects (residual stresses), for ISE effects in bulk metallic glasses[97]. However, significant efforts are needed to verify these models for explaining the ISE effects observed for amorphous and partially crystalline materials in present investigations.

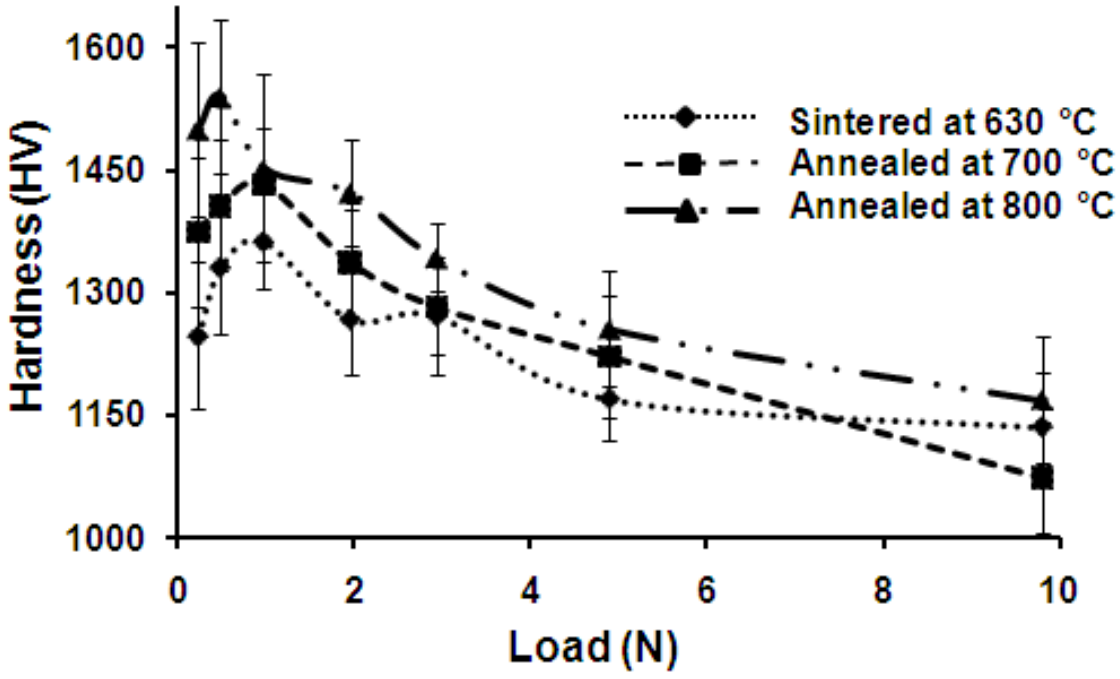

Fig.4.33 Microhardness at different loads of a) Fe-based BMG sintered at 630 °C, b) annealed at 700 °C for 20 min., and c) annealed at 800 °C for 20 min.[48].

4.4.3 Wear behavior

Fig. 4.34 presents the variation of cumulative weight loss as a function of sliding time during ball-on-disc wear test for samples SPS sintered at 630 °C and samples annealed at 700 and 800 °C. The maximum weight loss was observed for the sintered sample. Note that this sample exhibited fully amorphous structure based on XRD analysis. The samples annealed at 700 and 800 °C, which exhibited partially crystalline structure, showed significantly decreased weight loss. The decrease in total weight loss was about 67% and 75% for samples annealed at 700 and 800 °C, respectively. The minimum weight loss was observed for samples annealed at 800 °C, indicating better wear resistance compared to SPS sintered amorphous samples.

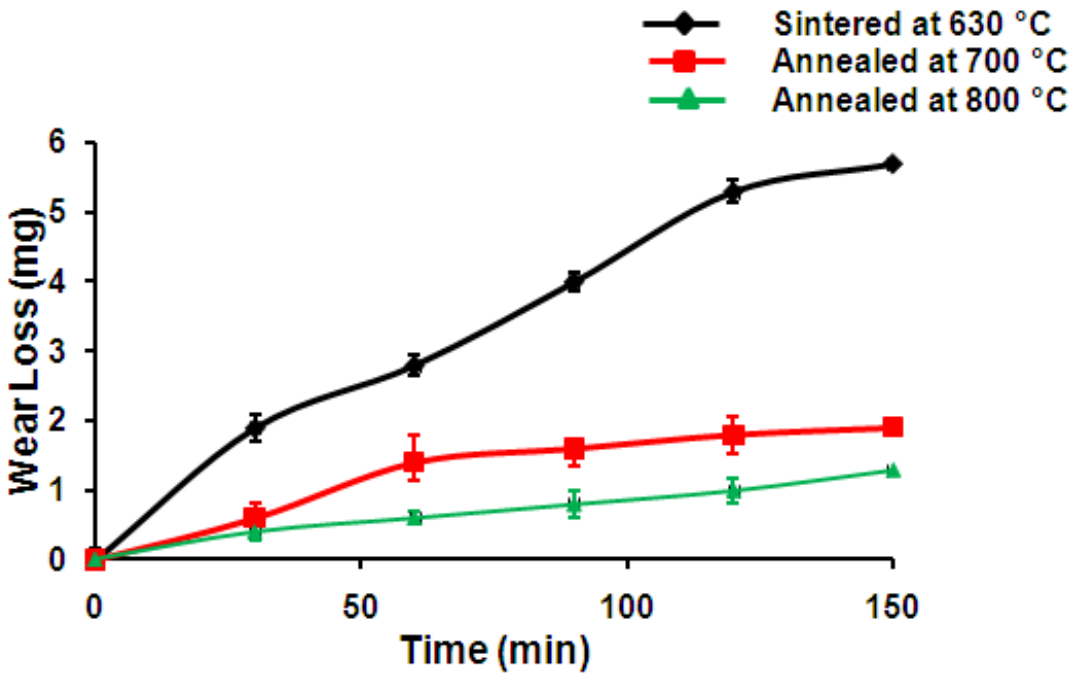

Fig.4.34 Weight loss as a function of time during wear test Fe-based BMG, a) sintered at 630 °C, 70 MPa, b) annealed at 700 °C for 20 min., and c) annealed at 800 °C for 20 min. [48].

The annealed samples exhibited relatively higher hardness compared to SPS sintered samples due to the presence of nanocrystallined complex carbide phases. Clearly, the weight loss behavior is in general agreement with Archard's rule suggesting an inverse relationship between wear volume loss and hardness. The depth profiles across the wear tracks for SPS sintered and annealed samples are also presented in Fig. 4.35. The SPS sintered samples showed wider wear track with average depth of about 22 μm. The depths of wear track for the samples annealed at 700 and 800 °C were about 14 and 3.5 μm, respectively. The weight loss behavior and wear track profile clearly establish that thermal annealing resulted in improvement in wear resistance. The variation of the coefficient of friction with sliding time is also shown in Fig. 4.36.

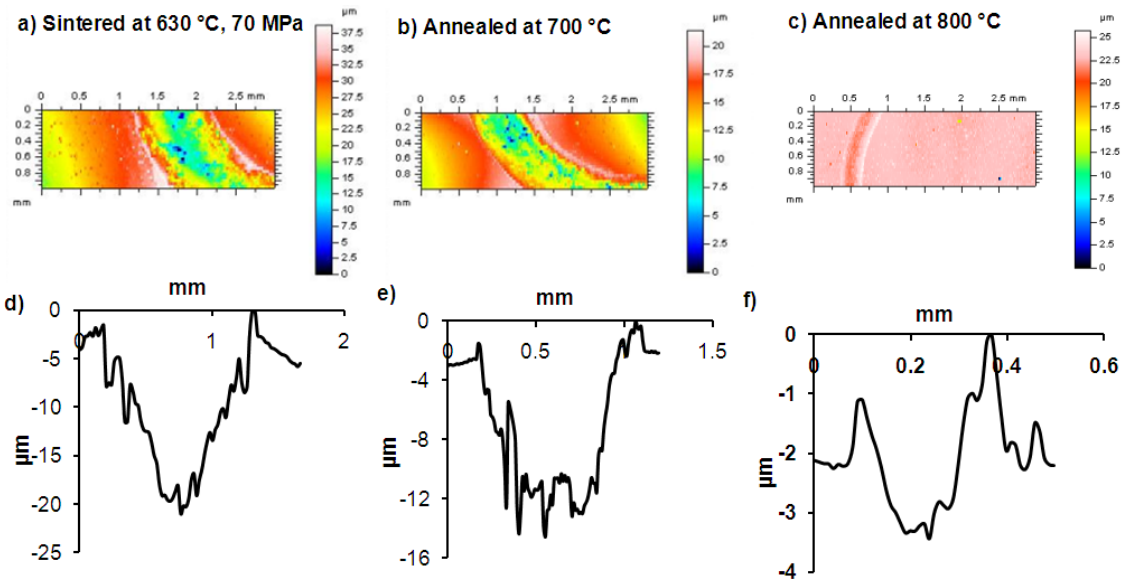

Fig.4.35 Wear profile of a, d) Fe-based BMG sintered at 630 °C, 70 MPa b, e) annealed at 700 °C for 20 min., c, f) annealed at 800 °C for 20 min.[48].

The average coefficient of friction (COF) for the sintered amorphous sample was 0.5; whereas the COF for annealed samples increased to about 0.6. The increase in COF for annealed samples may be due to a heterogeneous microstructure consisting of an amorphous matrix and nanocrystallined hard carbide phases.

To investigate any micro structural and compositional changes due to wear tests, detailed XRD and SEM/EDS analysis of the worn surfaces and wear debris was conducted. Fig. 4.37 presents XRD patterns from the worn surfaces of sintered and annealed samples. The XRD pattern from worn sintered sample exhibits broad diffused peak characteristic of amorphous material. This indicates that wear tests conducted in the present investigation did not induce any devitrification of amorphous sample during sliding wear. Note that these sintered samples showed the maximum wear loss.

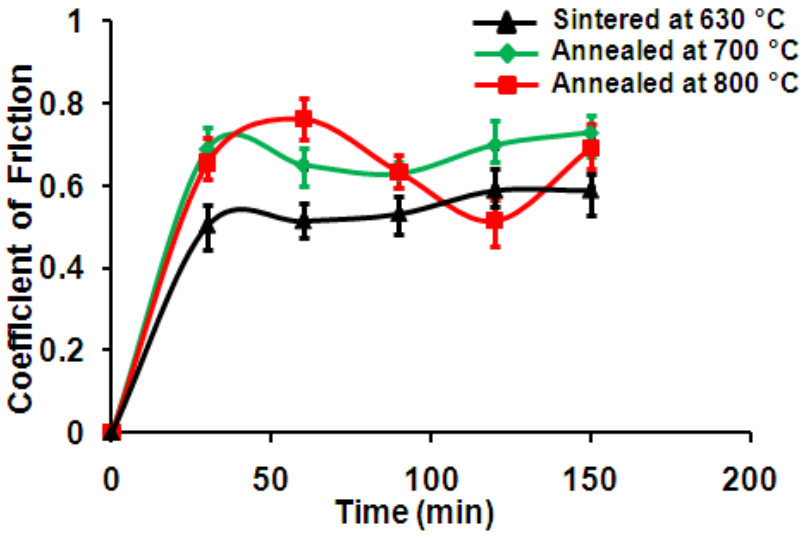

Fig.4.36 Coefficient of friction a) Fe-based BMG sintered at 630 °C, 70 MPa, b) annealed at 700 °C for 20 min., and c) annealed at 800 °C for 20 min. [48].

The XRD patterns from worn-out surfaces of annealed samples retained the amorphous background and superimposed peaks corresponding to complex carbide phases. No new phases were detected in these annealed samples. Several previous investigations on wear behavior of bulk amorphous materials indicated devitrification of the samples upon wear testing due to mechanical (stress-induced) and thermal mechanisms. However, the wear testing parameters investigated in this study did not result in any structural transformations.

The EDS elemental maps from the worn surfaces of sintered and annealed samples are presented in Fig. 4.38. For the SPS sintered samples, the worn-out surface consisted of two distinct regions: relatively flatter featureless regions and regions filled with coarse wear debris. The featureless regions showed uniform distribution of major constituent elements (Fe, Cr, Mo, Y, and C) of amorphous material. The regions filled with coarse wear debris were rich in oxygen indicating oxidation during wear tests.

Similar observations were made for samples annealed at 700 and 800 °C. For the sample annealed at 800 °C, the oxygen-rich regions appear cracked and relatively flatter without heaps of coarse debris particles. This sample exhibited the best wear response among the samples due to highest hardness. This sample also showed some distributed aluminum-rich regions possibly due to adhesive material transport from the surfaces' alumina counter-body balls. Clearly, the oxidative wear mechanism dominated during the sliding wear of sintered and annealed samples. It appears that the wear proceeds with the formation of debris due to abrasion between contacting surfaces, followed by oxidation of debris due to continued rubbing action.

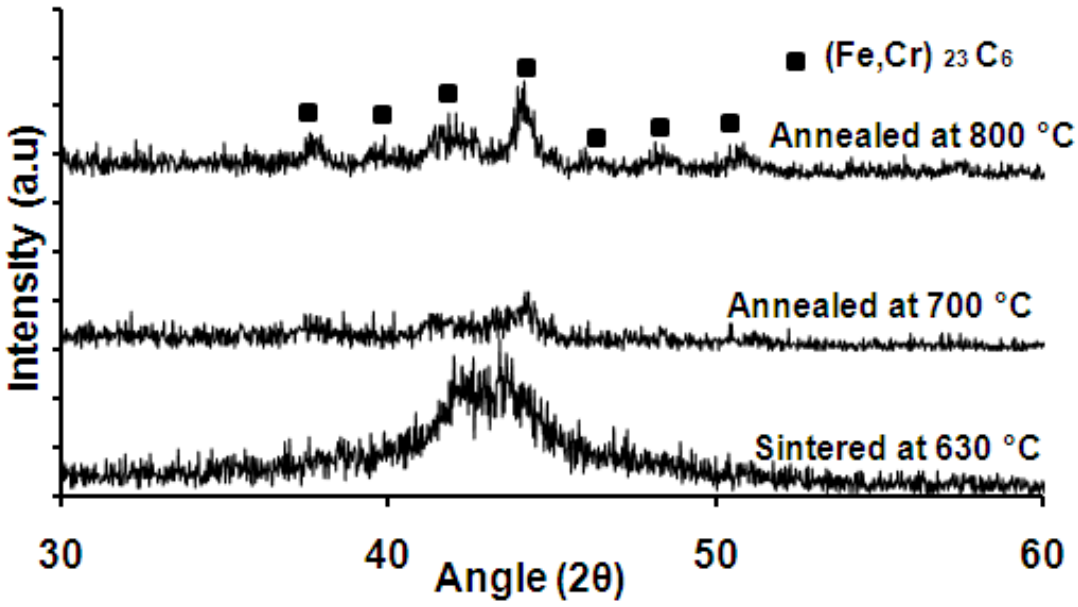

Fig.4.37 XRD of the wear track of SPS sintered Fe-based amorphous alloy at 630 °C, annealed at 700 °C, annealed at 800 °C [48].

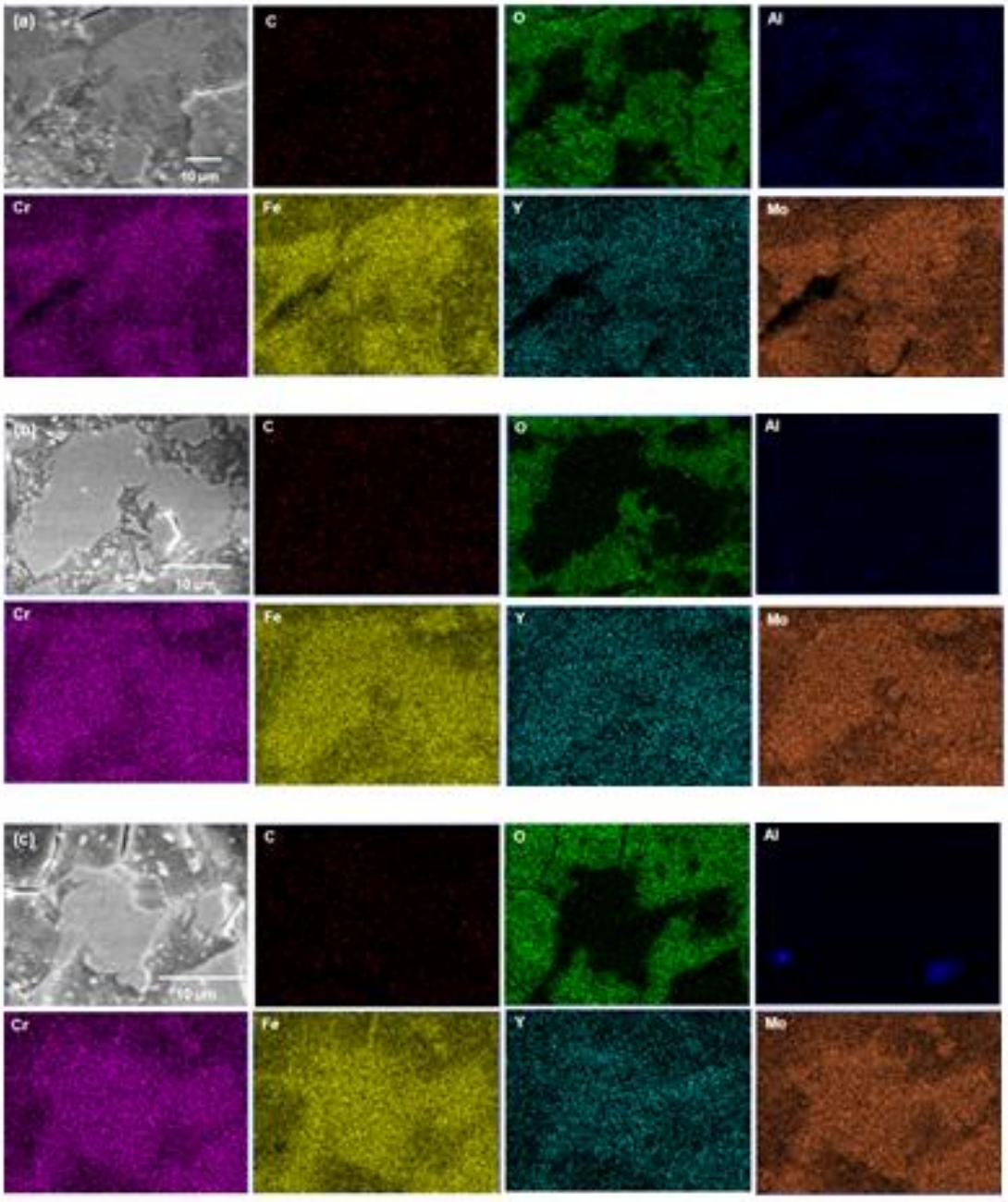

Fig.4.38 EDS of the wear surface of SPS sintered bulk amorphous alloy at a) 630 °C, 70 MPa, 10 min., b) annealed at 700 °C, c) annealed at 800 °C [48].

Fig. 4.39 presents the SEM micrographs of the wear debris. The wear debris from the sintered samples showed distribution of both fine and coarser particles. The high

magnification image of a coarser particle show sharp edges indicating abrasive fracture of the particles.

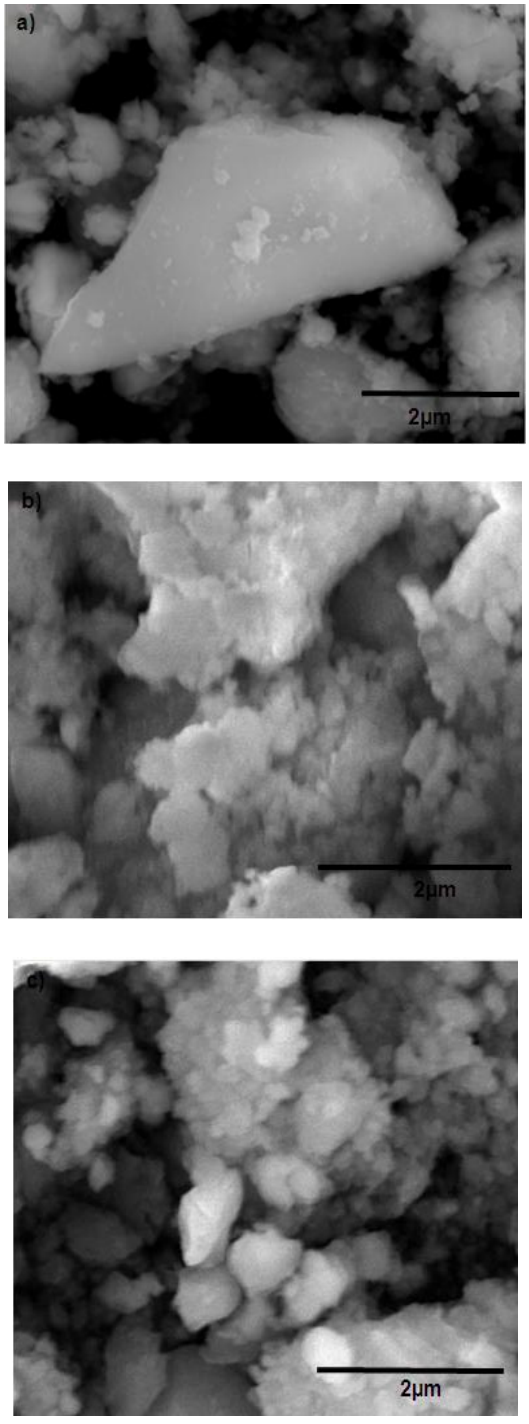

Fig.4.39 SEM image of wear debris of Fe-based amorphous alloy a) sintered at 600 °C, 70 MPa, 10 min., b) annealed at 700°C, and c) annealed at 800°C [48].

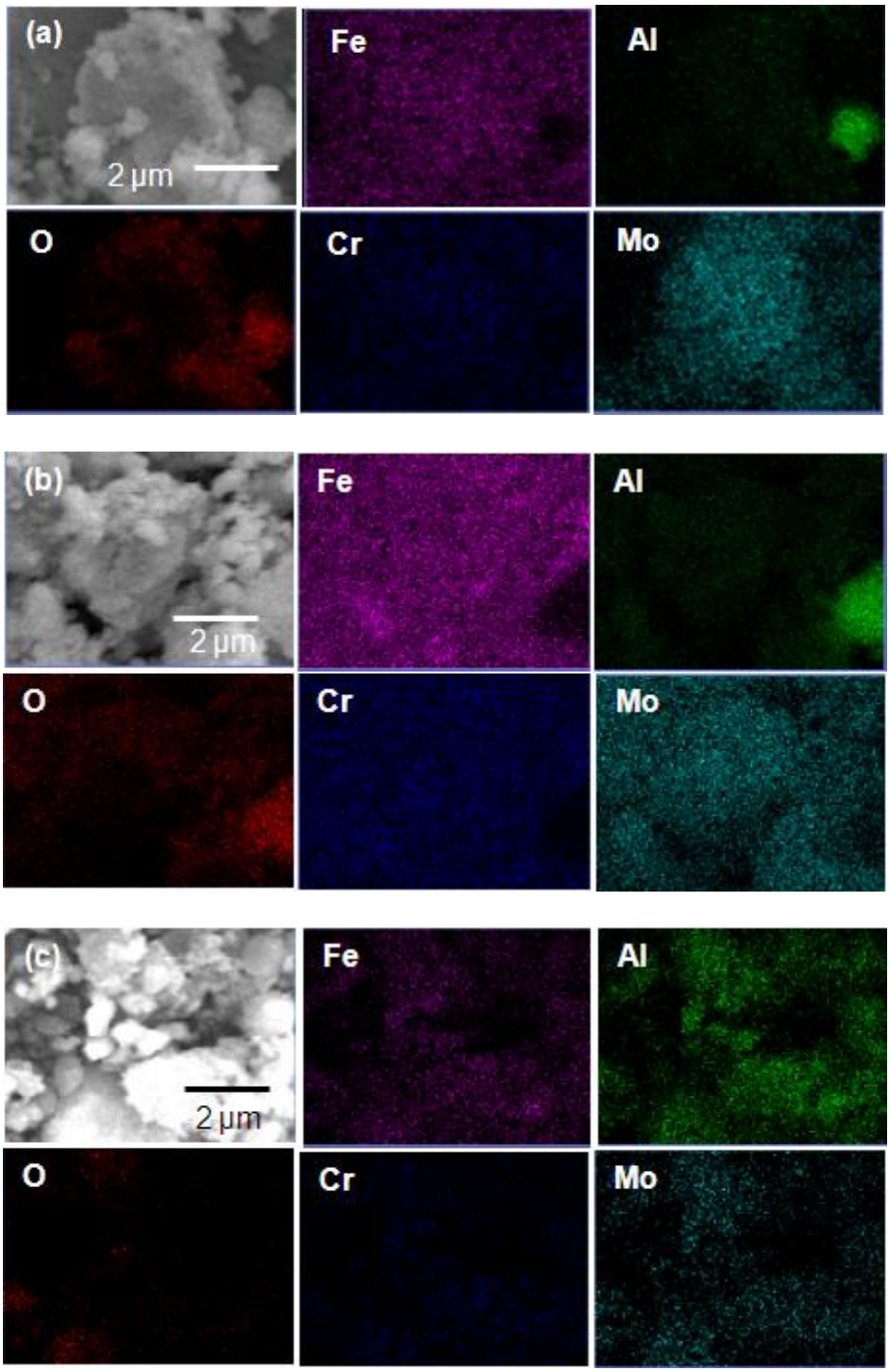

Fig.4.40 EDS analysis of wear debris of Fe-based amorphous alloy a) sintered at 630 °C, 70 MPa, 20 min., b)annealed at 700 °C, and c) annealed at 800 °C [48].

The wear debris from the annealed samples was mostly in the form of fine particles (in sub-micrometer range) and agglomerates in micrometer range. The EDS analysis of the wear debris from the sintered sample showed large oxygen-rich areas on and around the bigger debris particle (Fig. 4.40). The elemental distribution was fairly uniform in the remaining areas of the debris particle. This is probably due to accumulation of very fine oxide particles on bigger amorphous particles. An aluminum-rich region of about 2 μm can also be seen in the debris. Similar observations can be made for wear debris from samples annealed at 700 °C. The wear debris from the samples annealed at 800 °C show larger areas that are rich area in aluminum than in oxygen indicating accelerated adhesive transport of material from alumina counter-body balls to the wear surface. This is primarily due to the high hardness of samples annealed at 800 °C.

4.5 Laser surface treatment of Fe-based bulk amorphous alloys

Nd:YAG laser response of spark plasma sintered Fe-based bulk amorphous alloys was investigated at different laser processing parameters (Fig. 4.41). Two sets of samples: fully amorphous and partially crystallized, were laser treated at different scan speeds. Phase transformation, cross-section microstructure and microhardness of the laser treated surface were characterized. A thermal model using COMSOL was also developed to correlate laser thermal processing with microstructure and phase transformations.

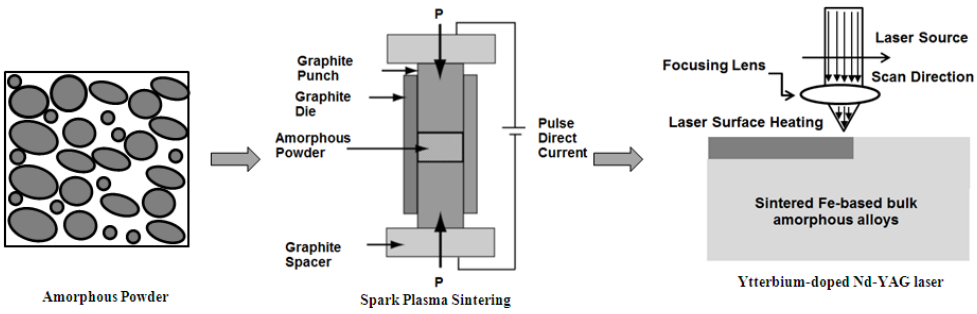

Fig.4.41 Schematic showing experimental steps involved in laser surface modified Fe-based bulk amorphous alloy.

A three dimensional thermo-physical model using COMSOL was developed to investigate temperature distribution and other thermal conditions during laser processing of Fe-based bulk amorphous alloys. A continuous laser beam having Gaussian energy distribution was used as the heat source for the model. Spot size of 0.6 mm at different laser velocities from 80 mm/s to 120 mm/s were considered. A disc of diameter 20 mm and thickness 1 mm was modelled to obtain the temperature distributions. Appropriate boundary conditions such as conduction, convection, and radiation were applied to the model. The governing equation for transient heat transfer based on Fourier's second law of heat transfer in solids used in the model is given by

$$\rho C_p \left[\frac{\partial T}{\partial t}\right] = k\left[\left(\frac{\partial^2 T}{\partial x^2}\right) + \left(\frac{\partial^2 T}{\partial y^2}\right) + \left(\frac{\partial^2 T}{\partial z^2}\right)\right] + Q \qquad (4.7)$$

where C_p is the specific heat, k is the thermal conductivity, and ρ is the density. Q is the total heat flux which consists of inward and outward heat fluxes. Inward heat flux which was caused by the laser beam and was applied to top surface of the disc is given by

$$Q_{in} = \left[\frac{P*A_c*(1-R_C)}{\pi*\sigma_x*\sigma_y}\right] * e^{-\left(\frac{(x-x_0)^2}{2\sigma_x^2}+\frac{(y-y_0)^2}{2\sigma_y^2}\right)} * e^{(-A_c*Z)} \quad (4.8)$$

Outward heat flux which includes natural convection and radiation to the surface and was applied to other boundaries is given by

$$Q_{out} = Q_{Conv} + Q_{Rad} \quad (4.9)$$

$$Q_{Conv} = h*[T-T_0] \quad (4.10)$$

$$Q_{rad} = \varepsilon*\sigma*[T^4-T_0^4] \quad (4.11)$$

Where h is the heat transfer coefficient, T_o is the ambient temperature, ε is the emissivity and σ is the Stefan-Boltzmann constant. Table 4.2 summarizes all the parameters which were used in the model. Maximum temperature reached due to laser heating depends on the laser power and the interaction time between the laser and material. The interaction time is calculated as residence time which is given by beam diameter (D)/laser scan speed (V).

Table 4.2: Interaction times and laser fluences for the experimental conditions used for the laser surface hardening of amorphous alloys.

Laser Power (W)	**Laser Scanning Speed (mm/s)**	**Interaction Time (ms)**	**Laser Fluence (J/mm^2)**
100	120	5.00	1.77
100	110	5.45	1.93
100	100	6.00	2.12
100	90	6.67	2.36

This model was used to predict the temperatures and cooling rates along the laser treated surface. The thermal interactions at the surface of a material during laser surface processing are generally determined by interaction time (t) and input laser fluence (F) [98]. For a continuous wave laser, these parameters are defined as:

$$t=d/V \tag{4.12}$$

$$F=Pt/A \tag{4.13}$$

where d is the diameter of the laser beam (mm), V is the laser scanning speed (mm/s), P is the laser power (W), and A is the area of laser beam. The laser interaction times and laser fluences for different laser scanning speeds used in this investigation are listed in Table 4.2.

4.5.1 Phase analysis

XRD patterns from as-sintered bulk Fe-based amorphous alloy and sintered alloy samples irradiated with Nd:YAG laser (laser fluences of 1.77, 1.93, 2.12, and 2.36 J/mm^2) are presented in Fig. 4.42. The XRD pattern from as-sintered alloy sample shows a characteristic broad halo peak indicating the amorphous structure of the alloy. This low intensity broad halo peak for the as-sintered samples was centered at about $2\theta=43°$. The broad halo peak with higher intensity was also observed for samples irradiated with laser fluence of 1.77 J/mm^2, indicating that the amorphous nature of the sample was retained with the laser heating. While the diffuse peak remained roughly at the same 2θ position, the samples laser irradiated with the laser fluence of 1.77 J/mm^2 exhibited relatively intense and narrower peaks compared to the diffuse peak from as-sintered amorphous sample. The increase in the intensity of the diffuse peak in these laser irradiated samples

(1.77 J/mm^2) is likely due to atomic level structural changes without affecting the general amorphous structure of the samples. In the case of metallic nano-glass with glass/glass interfaces, it has been reported that thermal annealing results in interface de-localization enhancing amorphization [99]. A decrease in intensity of the diffuse peak in XRD patterns with increasing annealing temperature indicating enhanced amorphization was observed for Zr-based nano-glass films [33]. In the present study, the intensity of the diffuse peak actually increased for the samples laser irradiated with laser fluence of 1.77 J/mm^2. This increase in intensity is most likely due to structural relaxation and associated enhanced atomic ordering and increase in density without changing the general amorphous structure of the sample. For the laser fluence of 1.77 J/mm^2, the interaction time is 5 ms. For such a short interaction time and lower energy fluence in this case, the thermal energy appears insufficient to raise the temperature above crystallization temperature of the Fe-based alloy, thereby retaining amorphous structure in the laser heated sample. Although the thermal energy due to laser irradiation appeared to initiate atomic-scale ordering, it was insufficient to initiate crystallization in these samples. The formation of such localized ordered regions due to structural relaxation in the amorphous matrix significantly influences the physical and mechanical properties of the amorphous solids [100].

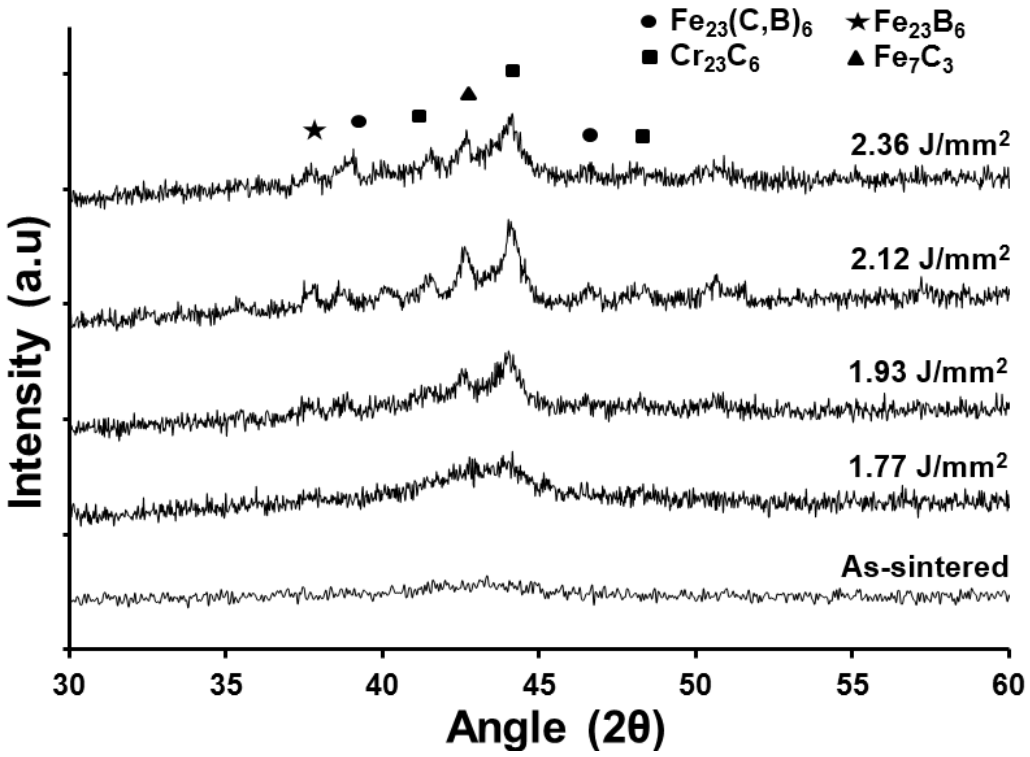

Fig.4.42 XRD patterns from as-sintered Fe-based amorphous alloy compacts and surfaces irradiated with laser fluences of 1.77, 1.93, 2.12, and 2.36 J/mm^2 [101].

The laser irradiation with higher laser fluences (1.93, 2.12, and 2.36 J/mm^2) resulted in partial crystallization, as indicated by the emergence of sharper peaks superimposed on background halo peaks in XRD patterns from these samples (Fig. 4.42). Most of these sharper peaks in XRD patterns correspond to $M_{23}(CB)_6$ phase and possibly M_7C_3 phase. The $M_{23}(CB_{)6}$ phase has also been identified as the principal phase in early stage crystallization during thermal annealing. This is primarily due to similar metals-to-metalloid ratios for the $M_{23}(CB)_6$ phase [23/6=3.833] and the overall amorphous alloy composition [79/21=3.762]. The samples irradiated with laser fluence of 1.93 J/mm^2 exhibited fewer and relatively broader peaks in the XRD pattern. The crystalline peaks became sharper and also new peaks appeared in the XRD patterns with increasing laser

fluence from 1.93 to 2.36 J/mm^2, indicating enhanced crystallization. The average crystallite sizes calculated using the Scherrer's equation were about 11, 19, and 21 nm for laser fluences of 1.93, 2.12, and 2.36 J/mm^2, respectively. It has been widely reported that the $Fe_{48}Cr_{15}Mo_{14}Y_2C_{15}B_6$ amorphous alloy devitrifies, forming $M_{23}(CB)_6$ nanocrystals of particle size up to 25 nm upon thermal processing [87]. The growth of nanocrystallites during primary crystallization of the amorphous alloys is governed by diffusion fields/concentration gradients around the crystallites. It has been observed that the crystallite growth ceases at a particle size of about 25 nm due to impingement of concentration gradients (soft impingement), resulting in non-random nucleation of crystallites in the residual amorphous phases around the primary crystallites [87]. While the interaction time in laser processing is much shorter than the holding time in thermal processing, the observed crystal size of 11-21 nm in the laser irradiated samples is consistent with these observations.

4.5.2 Microhardness

The distribution of hardness along the depth of laser irradiated amorphous samples is shown in Fig. 4.43. The average microhardness of the as-sintered amorphous samples was about 1200 HV. The laser treated samples recorded a significant increase in the surface hardness compared to untreated (as-sintered) samples. The microhardness of the laser treated samples decreased with the depth from the surface and reached the same microhardness as the as-sintered samples at about 250-500 μm below the surface. The surface hardness of about 1360 HV was observed for the samples irradiated with the laser fluence of 1.77 J/mm^2. Note that these samples appeared to have an amorphous structure

based on XRD analysis. The increase in hardness for these samples irradiated with relatively lower laser fluence (1.77 J/mm^2) appears to be due to structural relaxation caused by laser heating. It has been widely reported that heating of the amorphous alloy below crystallization temperature results in the formation of medium-range-ordering (MRO) clusters [102, 103]. The density of such MRO clusters increases with increasing thermal annealing temperature. Such MRO structures offer resistance to shear band propagation, increasing strength/hardness of the relaxed amorphous alloys. Such strengthening effects have been observed in Zr-Cu-Ti amorphous alloys by Chou *et al.* [104] . They also explained the strengthening based on free-volume theory [105]. Based on this theory, the extent of strengthening in the amorphous alloy has direct correlation with the reduction in free volume caused by thermal annealing below glass transition or crystallization temperature. The increase in nanohardness from 4.9 GPa for as-sputtered to 6.6. GPa for sub-Tg annealed (about 35% increase) Zr-Cu-Ti films has recently been reported [104]. In the present study, the increase in hardness due to structural relaxation (medium-range ordering and/or annihilation of free volume) was about 13% (from 1200 to 1360 HV) for the samples irradiated with laser fluence of 1.77 J/mm^2. The thermal effects during laser-material interactions diminish with the depth from the surface of the samples. The development of hardness profile seems to be directly related with the diminishing effects of structural relaxation due to thermal effects with the depth from the surface.

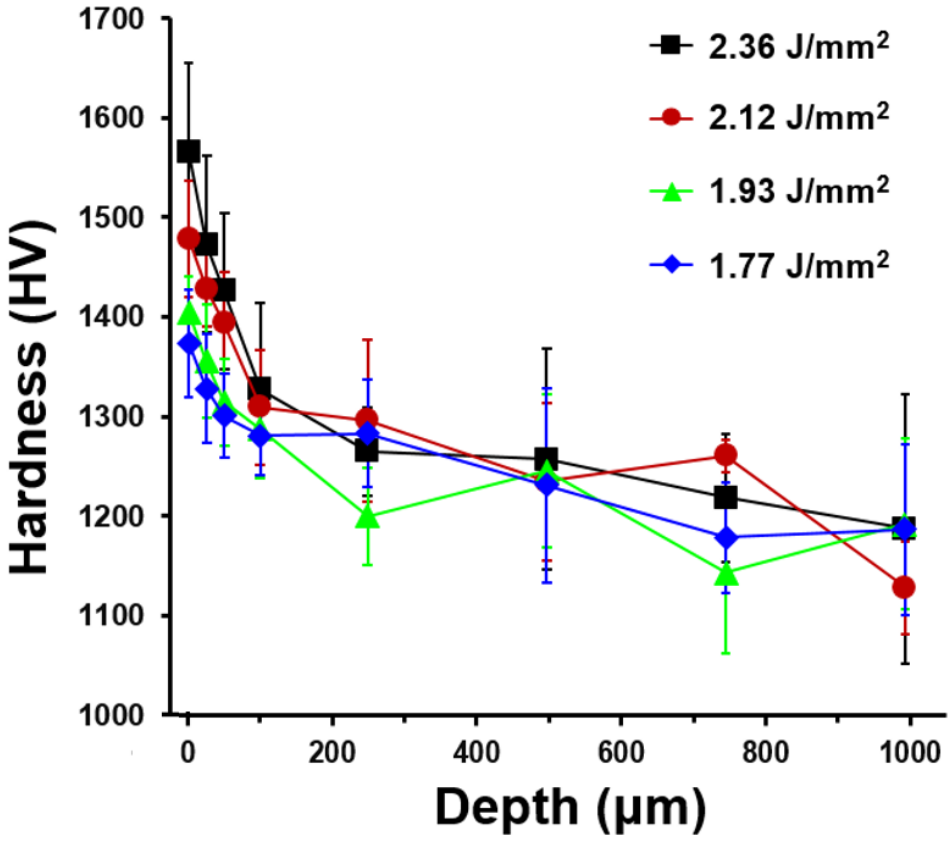

Fig.4.43 Microhardness along the depth of Fe-based bulk amorphous alloy compacts irradiated with laser fluences of 1.77, 1.93, 2.12, and 2.36 J/mm^2 [101].

The microhardness of the surfaces irradiated with higher laser fluences (1.93, 2.12, and 2.36 J/mm^2) was significantly higher than that for samples irradiated with laser fluence of 1.77 J/mm^2. In general, the surface hardness increased with the increasing laser fluence at the given laser power of 100 W. The highest surface hardness of about 1560 HV was observed for the samples irradiated with the highest laser fluence (2.36 J/mm^2). The average surface hardness was about 1480 and 1400 HV for the samples irradiated with laser fluence of 2.12 and 1.93 J/mm^2, respectively. The higher hardness of the samples irradiated with these higher laser fluences is primarily due to the formation of nanocrystals of the $M_{23}(CB)_6$ phase and possibly the M_7C_3 hard phases in the amorphous

matrix [48, 87]. The formation of such hard phases in the amorphous matrix is expected to increase the hardness of the material by offering enhanced resistance to the propagation of shear bands. The increasing surface microhardness seems to be primarily due to the increasing degree of nanocrystallization with increasing laser fluence. This is consistent with the XRD analysis indicating a higher degree of crystallinity with increasing laser fluence. The microhardness also decreases with depth from the surface of the samples and approaches the hardness of the as-sintered samples at about 250-500 μm. It seems that the extent of nanocrystallization as defined by the size and volume fraction of the nanoparticles is highest at the surface and progressively decreases with depth, establishing an observed hardness profile. Note that the design of most of the wear resistant steels such as high speed steels includes the selection of alloy chemistry that allows formation $M_{23}C_6$ and M_7C_3 type carbides[106]. These are some of the hardest carbides and impart exceptional hardness and wear resistance to these steels.

4.5.3 Thermal modeling and temperature distribution

The evolution of microstructure and associated development of mechanical properties in the laser irradiated amorphous alloys are the direct results of the thermal effects of the laser-material interactions.

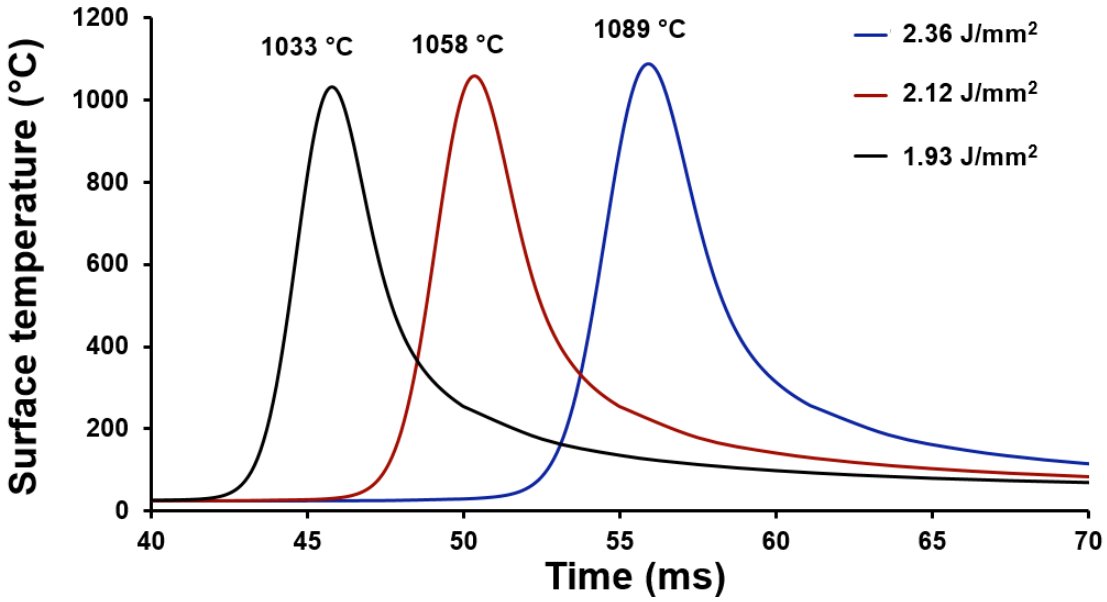

Fig.4.44 Surface temperature with time for the Fe-based amorphous alloys irradiated with laser fluences of 1.93, 2.12, and 2.36 J/mm^2 [101].

In the present case, the laser fluence of 1.77 J/mm^2 was selected to cause structural relaxation and nanocrystallization of the amorphous samples without any surface melting. After laser irradiation with the given processing parameters, no surface melting was observed. It is very difficult to experimentally characterize the thermal effects of laser-material interactions due to the extremely short interaction time. To investigate the thermal effects associated with laser interaction with the amorphous alloy under the given laser processing parameters, finite element modeling was conducted. Fig. 4.44 presents the variation of surface temperature during laser surface processing with laser fluence of 1.93, 2.12, and 2.36 J/mm^2. The reported crystallization temperature for the $Fe_{48}Cr_{15}Mo_{14}Y_2C_{15}B_6$ amorphous alloy is 653 °C [87]. For laser fluence, the surface temperature at any point rapidly increases, reaches maximum, and then starts decreasing as the laser beam scans over the point. The maximum surface temperatures of 1033,

1058, and 1089 °C were predicted for the laser fluences of 1.93, 2.12, and 2.36 J/mm^2, respectively. While the maximum surface temperature increases with increasing laser fluence, this temperature is well above the crystallization temperature of the alloy. The temperature distribution at different depths for the laser fluence of 2.36 J/mm^2 is shown in Fig. 4.45 (a). By tracing the crystallization temperature in temperature distributions at different depths, it can be observed that the maximum temperature is greater than crystallization temperature up to the depth of about 50 μm below the surface. It can also be observed that the time interval over which the temperature remains above the crystallization temperature also decreases with depth below the surface. At surface, this time interval is about 3.2 ms. Fig. 4.45 (b) shows the heating and cooling rates at the crystallization temperature for different depths. The heating and cooling rates are of the order of 3-5 × 10^5 °C/s at the surface. These rates decrease with depth below the surface. At the depth of about 50 μm, the heating and cooling rates are of the order of about 0.5-1 × 10^5 °C/s. While the heating and cooling rates are faster at the surface of the samples, the surfaces have a higher maximum temperature and a longer crystallization time interval. The enhanced surface nanocrystallization and higher surface microhardness in the samples laser irradiated with higher laser fluences seem to be the result of relatively higher maximum surface temperature and longer crystallization interval time.

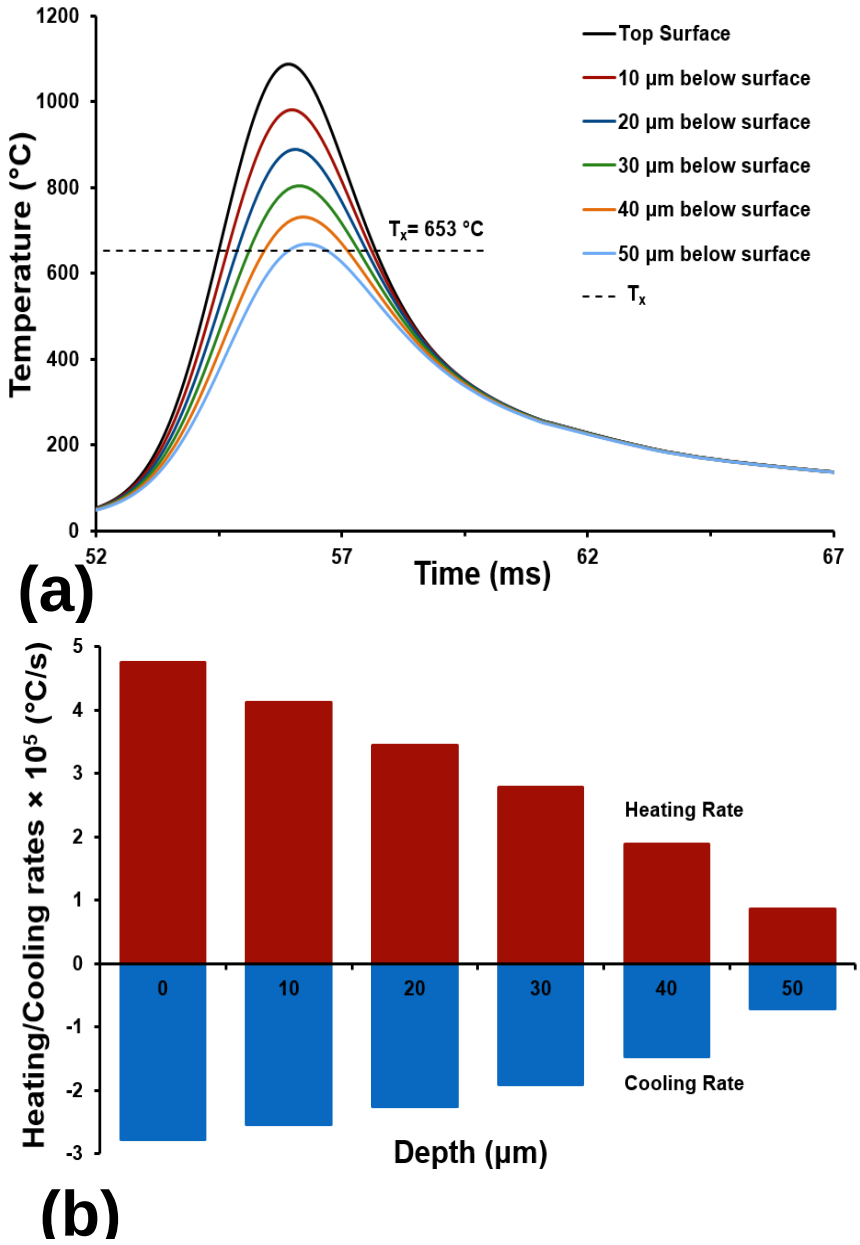

Fig.4.45 a) Temperature distributions, and b) heating and cooling rates at crystallization temperature at different depths for the Fe-based amorphous alloys irradiated with laser fluence of 2.36 J/mm^2 [101].

The depth of crystallization can also be estimated by tracing the crystallization temperature in the temperature distributions during heating and cooling times (as the laser beam passes over any point on the surface).

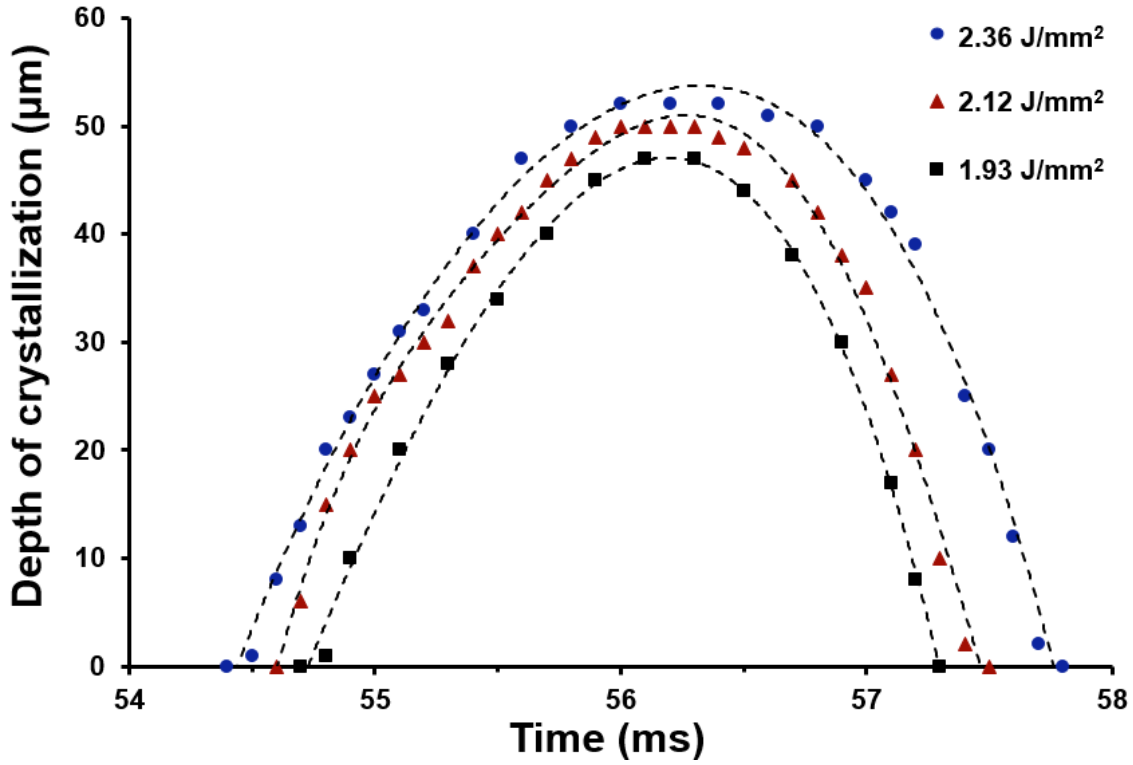

Fig.4.46 Depth of crystallization (position of isotherm corresponding to crystallization temperature) with time for the Fe-based amorphous alloys irradiated with laser fluences of 1.93, 2.12, and 2.36 J/mm^2 [101].

Fig. 4.46 shows the variation of depth of crystallization (depth at which the temperature has reached crystallization temperature) during laser interaction time for different laser fluences. For each laser fluence, the depth of crystallization increases, reaches maximum, and then decreases *i.e.*, the isotherm corresponding to crystallization temperature initiates at the surface and moves to certain depth during heating before returning back to the surface during the cooling region. The maximum depths of crystallization are about 47, 50, and 52 μm for the laser fluences of 1.93, 2.12, and 2.36 J/mm^2, respectively. Due to significant scatter in the data (Fig. 4.43), it is difficult to determine the depth of hardening based on experimental hardness measurements. Also,

the hardening due to structural relaxation at depths below the crystallization temperature isotherm cannot be included in the thermal model. The surface hardness in the amorphous alloys irradiated with lowest laser fluence (1.77 J/mm^2) is 1360 HV. These processing conditions seem to have resulted in structural relaxation without any surface crystallization based on XRD analysis.

Considering 1360 HV as the hardness limit for defining the depth of crystallization, the experimental data yields the depth of crystallization in the range of 35-80 μm, which is relatively closer to the predicted depths. Clearly, the structural relaxation (medium-range ordering and/or annihilation of free volume) and formation of hard carbides at nano-scale particle size (typically less than 25 nm) in the amorphous matrix using laser surface irradiation presents an interesting possibility for relatively shallow surface hardening of these Fe-based amorphous alloys with multi-functional properties.

CHAPTER V

CONCLUSIONS

Spark plasma sintering of amorphous powder ($Fe_{48}Cr_{15}Mo_{14}Y_2C_{15}B_6$) at sintering temperature of about 100 ºC lower than the crystallization temperature resulted in highly dense (~95%) fully amorphous compacts. Formation of crystalline $Fe_{23}(C, B)_6$ phases within a near-fully dense (~99%) amorphous matrix was observed at a sintering temperature close to glass transition temperature (which is significantly less than crystallization temperatures: T_{x1} and T_{x2}). The near-full densification of the amorphous alloy powder was observed during the heating stage of the sintering cycle. Microstructure evolution in the sintered compacts indicated that density, degree of crystallinity, and mechanical properties can be effectively controlled by optimizing SPS processing parameters. Spark plasma sintering of Fe-based amorphous alloys in the supercooled region (630 ºC) resulted in near full densification of alloys (98.5% relative density). SPS, thus, presents tremendous potential for fabrication of 'bulk' amorphous and amorphous matrix composites at significantly lower temperatures and shorter times.

The SPS process can be effectively used for processing of multi-component Fe-based bulk amorphous alloys and there *in situ* nano composites with controlled primary nano crystallization. EQ-SANS experiments showed significant scattering for the samples

sintered in supercooled region indicating local structural/compositional changes associated with the profuse nucleation of nano clusters (~4 nm). For the spark plasma sintered samples near and above crystallization temperature, the SANS data showed formation of interference maximum, which shifted to lower Q-range with increasing sintering temperature due to the formation and growth of $(Fe,Cr)_{23}C_6$ crystallites. The SANS data also indicated evolution of bimodal crystallite distribution at sintering temperatures above crystallization temperature possibly due to simultaneous nucleation of new crystals and growth of the existing nanocrystallites or the second crystallization event (T_{x2}, 683°C). It seems that the growth of primary nanocrystallites ceases due to the impingement of concentration gradient fields (soft impingement effect), leading to non-random nucleation of crystallites near the primary crystallites.

Annealing of sintered samples above crystallization temperatures (700 ºC and 800 ºC) resulted in partial devitrification, forming complex carbides of chromium and iron. The partial devitrification resulted in an increase in microhardness and wear resistance. The as-sintered (amorphous) and partially devitrified (annealed) samples exhibited strong indentation size effects, possibly due to combination of a various mechanisms, including non-crystalline flow defects (shear bands, free volume), strain softening, and surface effects (residual stresses).

Surface hardening of spark plasma sintered $Fe_{48}Cr_{15}Mo_{14}Y_2C_{15}B_6$ bulk amorphous alloys using a continuous-wave Nd:YAG laser is reported. The extent of hardening (surface hardness and depth) depends on the nature of structural changes from the thermal effects of laser–material interactions. For the laser fluence of 1.77 J/mm^2, the general amorphous structure was retained (based on XRD analysis) after laser treatment.

The increase in hardness from about 1200 HV to 1360 HV (13% increase) in these samples is likely caused by structural relaxation (enhanced medium-range ordering or annihilation of excess free volume). At higher laser fluences (1.93 J/mm^2, 2.12 J/ mm^2, and 2.36 J/mm^2), nanocrystallization forming $M_{23}C_6$- and M7C3-type hard carbides was observed, resulting in enhanced surface hardening. An about 30% increase in hardness (from 1200 HV to 1560 HV) is recorded for the samples irradiated with laser fluence of 2.36 J/mm^2. With the depth of hardening in the sub millimeter range, the laser surface processing presents an interesting possibility of relatively shallow hardening of Fe-based amorphous alloys with improved surface properties.

CHAPTER VI

FUTURE WORK

Efforts are required to process and characterize Fe-based bulk amorphous alloy composites. As we have observed plasticity couldn't be induced after reinforcing Fe-based amorphous alloys with *in situ* composites, *ex situ* Fe-based amorphous alloys should be processed and characterized in order to induce plasticity. Efforts should also be made to scale up the processing of Fe-based amorphous alloys in order to investigate the largest possible size that can be made using SPS technique. Formation of clusters (less than 5 nm) was observed in the supercooled region during SANS of SPS-sintered Fe-based amorphous alloys. Preliminary TEM results shows formation of nanocrystallites and a concentric residual amorphous phase around these nanocrystals in the amorphous matrix. We have performed size distribution analysis using SANS considering crystallites as $Fe_{23}(C,B)_6$ and rest as amorphous phase. Exact composition of the crystallites and the residual amorphous phase is required to perform detailed analysis of distribution of crystallites and the residual amorphous phase in amorphous matrix which can be obtained using atom probe tomography (APT). Detailed TEM/EDS and APT is required to characterize the compositional variation in the crystallization behavior during SPS sintering of amorphous alloys. During SPS sintering, high density direct current passes

through the surface of the powder at the contact points leading to localized overheating/melting [24]. This highly confined temperature rise leads to a temperature gradient from the surface towards the center of the powder. Few efforts are made to characterize the contact points/necking regions of SPS sintered amorphous alloys. Investigations which involve highly localized nanoscale/sub-micron regions should be performed using APT, TEM, and EDS analysis.

REFERENCES

1. Wang, W.H., C. Dong, and C.H. Shek, *Bulk metallic glasses.* Materials Science and Engineering: R: Reports, 2004. **44**(2–3): p. 45-89.
2. W. Klement, R.W., and P. Duwez, *Non-crystalline structure in solidified gold-silicon alloys.* Nature, 1960. **187**: p. 869–870.
3. Schroers, J., *The superplastic forming of bulk metallic glasses.* JOM, 2005. **57**(5): p. 35-39.
4. Choi-Yim, H. and W.L. Johnson, *Bulk metallic glass matrix composites.* Applied Physics Letters, 1997. **71**(26): p. 3808-3810.
5. J. Eckert, M.S., N. Schlorke, A. Kübler, L. Schultz, *Solid State Processing of Bulk Metallic Glass Forming Alloys.* Materials Science Forum 1997. **235 - 238**: p. 23-28.
6. Inoue, A., *High strength bulk amorphous alloys with low critical cooling rates.* Material transactions 1995. **36**(36): p. 866-875.
7. Hays, C.C., C.P. Kim, and W.L. Johnson, *Large supercooled liquid region and phase separation in the Zr--Ti--Ni--Cu--Be bulk metallic glasses.* Applied Physics Letters, 1999. **75**(8): p. 1089-1091.
8. Foley, J.C., D.J. Sordelet, and T.A. Lograsso, *Characterization of Gas Atomized Cu48Ti34Zr10Ni8 Amorphous Metal Powder.* MRS Online Proceedings Library, 1998. **554**: p. null-null.
9. Branagan, D.J., et al., *A new generation of gas atomized powder with improved levels of energy product and processability.* Magnetics, IEEE Transactions on, 1996. **32**(5): p. 5097-5099.
10. Cardoso, K.R., et al., *Amorphous and nanostructured Al–Fe–Nd powders obtained by gas atomization.* Materials Science and Engineering: A, 2001. **315**(1–2): p. 89-97.
11. Inoue, A., et al., *Al-Y-Ni amorphous powders prepared by high-pressure gas atomization.* Journal of Materials Science Letters, 1988. **7**(12): p. 1287-1290.
12. Pavuna, D., *Production of metallic glass ribbons by the chill-block melt-spinning technique in stabilized laboratory conditions.* Journal of Materials Science, 1981. **16**(9): p. 2419-2433.
13. Wang, Y., K. Xu, and Q. Li, *Comparative study of non-isothermal crystallization kinetics between Fe80P13C7 bulk metallic glass and melt-spun glassy ribbon.* Journal of Alloys and Compounds, 2012. **540**(0): p. 6-15.
14. Tkatch, V.I., et al., *The effect of the melt-spinning processing parameters on the rate of cooling.* Materials Science and Engineering: A, 2002. **323**(1–2): p. 91-96.
15. Ishihara, S., W. Zhang, and A. Inoue, *Hot pressing of Fe–Co–Nd–Dy–B glassy powders in supercooled liquid state and hard magnetic properties of the consolidated alloys.* Scripta Materialia, 2002. **47**(4): p. 231-235.

16. Dougherty, G.M., G.J. Shiflet, and S.J. Poon, *Synthesis and microstructural evolution of Al□Ni□Fe□Gd metallic glass by mechanical alloying.* Acta Metallurgica et Materialia, 1994. **42**(7): p. 2275-2283.
17. Yagi, M., et al., *Magnetic properties of Fe-based amorphous powder cores produced by a hot-pressing method.* Journal of Magnetism and Magnetic Materials, 2000. **215–216**(0): p. 284-287.
18. Kang, E.Y., et al., *Vacuum hot pressing of Fe–Si–B–Nb-based amorphous powder cores and their high-frequency magnetic properties.* Journal of Applied Physics, 2006. **99**(8): p. -.
19. Munir, Z.A., D.V. Quach, and M. Ohyanagi, *Electric Current Activation of Sintering: A Review of the Pulsed Electric Current Sintering Process.* Journal of the American Ceramic Society, 2011. **94**(1): p. 1-19.
20. Garay, J.E., *Current-Activated, Pressure-Assisted Densification of Materials.* Annual Review of Materials Research, 2010. **40**(1): p. 445-468.
21. Diouf, S. and A. Molinari, *Densification mechanisms in spark plasma sintering: Effect of particle size and pressure.* Powder Technology, 2012. **221**(0): p. 220-227.
22. Tokita, M., *Mechanisms of spark plasma sintering.* Proceedings of the 2000 Powder Metallurgy World Congress, 2000: p. 729–732.
23. Song, X., X. Liu, and J. Zhang, *Neck Formation and Self-Adjusting Mechanism of Neck Growth of Conducting Powders in Spark Plasma Sintering.* Journal of the American Ceramic Society, 2006. **89**(2): p. 494-500.
24. Perrière, L., et al., *Spark plasma sintering for metallic glasses processing.* Revue de Métallurgie, 2012. **109**(01): p. 5-10.
25. Hulbert, D.M., et al., *A discussion on the absence of plasma in spark plasma sintering.* Scripta Materialia, 2009. **60**(10): p. 835-838.
26. Anselmi-Tamburini, U., et al., *Fundamental investigations on the spark plasma sintering/synthesis process: II. Modeling of current and temperature distributions.* Materials Science and Engineering: A, 2005. **394**(1–2): p. 139-148.
27. Wang, C., L. Cheng, and Z. Zhao, *FEM analysis of the temperature and stress distribution in spark plasma sintering: Modelling and experimental validation.* Computational Materials Science, 2010. **49**(2): p. 351-362.
28. Olevsky, E. and L. Froyen, *Constitutive modeling of spark-plasma sintering of conductive materials.* Scripta Materialia, 2006. **55**(12): p. 1175-1178.
29. G.Mol´enat, L.D., J. Galy, and A. Couret, *Temperature control in spark plasma sintering: An FEM approach.* Journal of Metallurgy, 2010. **2010**: p. 1-9.
30. Kim, T.-S., et al., *Consolidation of Cu54Ni6Zr22Ti18 bulk amorphous alloy powders.* Materials Science and Engineering: A, 2005. **402**(1–2): p. 228-233.
31. Ozaki, K., et al., *Preparing Mg–Ni–Si amorphous powders by mechanical alloying and consolidation by pulsed current sintering.* Materials Science and Engineering: A, 2004. **375–377**(0): p. 857-860.
32. Francoois O. Mear, G.X., Dmitri V. Louzguine-Luzgin and Akihisa Inoue, *Spark plasma sintering of Mg-based amorphous ball milled powders.* Materials Transactions, 2009. **50**(3): p. 588-591.

33. Li, Q., et al., *Ti50Cu23Ni20Sn7 bulk metallic glasses prepared by mechanical alloying and spark-plasma sintering.* Journal of Materials Processing Technology, 2009. **209**(7): p. 3285-3288.
34. Kim, C.K., et al., *Microstructure and mechanical properties of Cu-based bulk amorphous alloy billets fabricated by spark plasma sintering.* Materials Science and Engineering: A, 2005. **406**(1–2): p. 293-299.
35. Xie, G., et al., *Fabrication of porous Zr–Cu–Al–Ni bulk metallic glass by spark plasma sintering process.* Scripta Materialia, 2006. **55**(8): p. 687-690.
36. Wang, D.J., et al., *Temperature influence on sintering with concurrent crystallization behavior in Ti-based metallic glassy powders.* Materials Science and Engineering: A, 2010. **527**(10–11): p. 2662-2668.
37. Pan, D.G., et al., *Enhanced plasticity in Mg-based bulk metallic glass composite reinforced with ductile Nb particles.* Applied Physics Letters, 2006. **89**(26): p. 261904.
38. Hays, C.C., C.P. Kim, and W.L. Johnson, *Microstructure Controlled Shear Band Pattern Formation and Enhanced Plasticity of Bulk Metallic Glasses Containing in situ Formed Ductile Phase Dendrite Dispersions.* Physical Review Letters, 2000. **84**(13): p. 2901-2904.
39. Wei, Q., et al., *Evolution and microstructure of shear bands in nanostructured Fe.* Applied Physics Letters, 2002. **81**(7): p. 1240-1242.
40. Lee, J.-C., et al., *Enhanced plasticity in a bulk amorphous matrix composite: macroscopic and microscopic viewpoint studies.* Acta Materialia, 2005. **53**(1): p. 129-139.
41. Maddala, D.R., A. Mubarok, and R.J. Hebert, *Sliding wear behavior of Cu50Hf41.5Al8.5 bulk metallic glass.* Wear, 2010. **269**(7–8): p. 572-580.
42. Gloriant, T., *Microhardness and abrasive wear resistance of metallic glasses and nanostructured composite materials.* Journal of Non-Crystalline Solids, 2003. **316**(1): p. 96-103.
43. Li, G., et al., *Wear behavior of bulk Zr41Ti14Cu12.5Ni10Be22.5 metallic glasses.* Journal of Materials Research, 2002. **17**(08): p. 1877-1880.
44. Gu, X.J., S.J. Poon, and G.J. Shiflet, *Mechanical properties of iron-based bulk metallic glasses.* Journal of Materials Research, 2007. **22**(02): p. 344-351.
45. Ponnambalam, V., S.J. Poon, and G.J. Shiflet, *Fe-based bulk metallic glasses with diameter thickness larger than one centimeter.* Journal of Materials Research, 2004. **19**(05): p. 1320-1323.
46. Kawamura, Y., et al., *Superplasticity in Fe-based metallic glass with wide supercooled liquid region.* Materials Science and Engineering: A, 2001. **304–306**(0): p. 735-739.
47. Stoica, M., et al., *Mechanical behavior of Fe65.5Cr4Mo4Ga4P12C5B5.5 bulk metallic glass.* Intermetallics, 2005. **13**(7): p. 764-769.
48. Singh, A., et al., *Densification Behavior and Wear Response of Spark Plasma Sintered Iron-Based Bulk Amorphous Alloys.* Advanced Engineering Materials, 2012. **14**(6): p. 400-407.
49. Harimkar, S.P., et al., *Microstructure and properties of spark plasma sintered Fe–Cr–Mo–Y–B–C bulk metallic glass.* Journal of Non-Crystalline Solids, 2009. **355**(43–44): p. 2179-2182.

50. Zhang, C., Y. Wu, and L. Liu, *Robust hydrophobic Fe-based amorphous coating by thermal spraying.* Applied Physics Letters, 2012. **101**(12): p. 121603-4.
51. Yang, Q., et al., *Compositional dependence of microstructure and tribological properties of plasma sprayed Fe-based metallic glass coatings.* Science China Technological Sciences, 2012. **55**(5): p. 1335-1342.
52. Basu, A., et al., *Laser surface coating of Fe–Cr–Mo–Y–B–C bulk metallic glass composition on AISI 4140 steel.* Surface and Coatings Technology, 2008. **202**(12): p. 2623-2631.
53. Guo, F., S.J. Poon, and G.J. Shiflet, *Metallic glass ingots based on yttrium.* Applied Physics Letters, 2003. **83**(13): p. 2575-2577.
54. Lu, Z.P., C.T. Liu, and W.D. Porter, *Role of yttrium in glass formation of Fe-based bulk metallic glasses.* Applied Physics Letters, 2003. **83**(13): p. 2581-2583.
55. J. Blink, J.F., J. Choi, and C. Saw, *Applications in the nuclear industry for thermal spray amorphous metal and ceramic coatings.* Metallurgical and Materials Transactions A, 2009. **40 A**: p. 1344-1354.
56. Lamparter, P. and S. Steeb, *Small angle x-ray and neutron scattering for the investigation of the medium-range structure of metallic glasses.* Journal of Non-Crystalline Solids, 1988. **106**(1–3): p. 137-146.
57. Fratzl, P., *Small-angle scattering in materials science - a short review of applications in alloys, ceramics and composite materials.* Journal of Applied Crystallography, 2003. **36**(3 Part 1): p. 397-404.
58. Pekarskaya, E., J.F. Löffler, and W.L. Johnson, *Microstructural studies of crystallization of a Zr-based bulk metallic glass.* Acta Materialia, 2003. **51**(14): p. 4045-4057.
59. Loffler, J.F., et al., *Crystallization of bulk amorphous Zr--Ti(Nb)--Cu--Ni--Al.* Applied Physics Letters, 2000. **77**(4): p. 525-527.
60. Holland, T.B., J.F. Loffler, and Z.A. Munir, *Crystallization of metallic glasses under the influence of high density dc currents.* Journal of Applied Physics, 2004. **95**(5): p. 2896-2899.
61. Bhardwaj, V.R., et al., *Femtosecond laser-induced refractive index modification in multicomponent glasses.* Journal of Applied Physics, 2005. **97**(8): p. 083102-9.
62. Banas, G., et al., *Laser shock-induced mechanical and microstructural modification of welded maraging steel.* Journal of Applied Physics, 1990. **67**(5): p. 2380-2384.
63. Matthews, D.T.A., V. Ocelík, and J.T.M. de Hosson, *Tribological and mechanical properties of high power laser surface-treated metallic glasses.* Materials Science and Engineering: A, 2007. **471**(1–2): p. 155-164.
64. Chen, B., et al., *Improvement in mechanical properties of a Zr-based bulk metallic glass by laser surface treatment.* Journal of Alloys and Compounds, 2010. **504, Supplement 1**(0): p. S45-S47.
65. Hoekstra, J.G., et al., *Laser Surface Modification of a Crystalline Al-Co-Ce Alloy for Enhanced Corrosion Resistance.* Advanced Engineering Materials, 2005. **7**(9): p. 805-809.
66. JING Qin, Z.L., YUAN Hui, ZHANG Bing, NIU RunBing, ZHANG Jin, LI Gong, MA MingZhen & LIU RiPing, *Crystallization and thermal fatigue of*

ZrTiCuNiBe bulk amorphous alloys heated by laser pulses. SCIENCE CHINA Physics,Mechanics & Astronomy, 2010. **53**(3): p. 419-423.

67. Chu, Z.H., et al., *Consolidation and mechanical properties of Cu46Zr42Al7Y5 metallic glass by spark plasma sintering.* Journal of Non-Crystalline Solids, 2012. **358**(10): p. 1263-1267.
68. Liu, Y., et al., *The Soret effect in bulk metallic glasses.* Intermetallics, 2007. **15**(4): p. 557-563.
69. Ponnambalam, V., et al., *Synthesis of iron-based bulk metallic glasses as nonferromagnetic amorphous steel alloys.* Applied Physics Letters, 2003. **83**(6): p. 1131-1133.
70. Burton, A.W., et al., *On the estimation of average crystallite size of zeolites from the Scherrer equation: A critical evaluation of its application to zeolites with one-dimensional pore systems.* Microporous and Mesoporous Materials, 2009. **117**(1–2): p. 75-90.
71. Ilavsky, J. and P.R. Jemian, *Irena: tool suite for modeling and analysis of small-angle scattering.* Journal of Applied Crystallography, 2009. **42**(2): p. 347-353.
72. Khalil, K.A. and S.W. Kim, *Effect of Processing Parameters on the Mechanical and Microstructural Behavior of Ultra-Fine Al2O3– (ZrO2+8%Mol Y2O3) Bioceramic, Densified By High-Frequency Induction Heat Sintering.* International Journal of Applied Ceramic Technology, 2006. **3**(4): p. 322-330.
73. German, R.M., *Sintering densification for powder mixtures of varying distribution widths.* Acta Metallurgica et Materialia, 1992. **40**(9): p. 2085-2089.
74. Singh, A. and S.P. Harimkar, *Spark plasma sintering of in situ and ex situ iron-based amorphous matrix composites.* Journal of Alloys and Compounds, 2010. **497**(1–2): p. 121-126.
75. Shin, S., M.-S. Song, and T.-S. Kim, *Synthesis of diamond-reinforced Zr65Al10Ni10Cu15 metallic glass composites by pulsed current sintering.* Materials Science and Engineering: A, 2009. **499**(1–2): p. 525-528.
76. Singh, A., et al., *Microstructure and tribological behavior of spark plasma sintered iron-based amorphous coatings.* Materials Science and Engineering: A, 2010. **527**(18–19): p. 5000-5007.
77. Bakkal, M., et al., *Oxidation and crystallization of Zr-based bulk metallic glass due to machining.* Intermetallics, 2004. **12**(2): p. 195-204.
78. Tang, X.P., et al., *Devitrification of the Zr41.2Ti13.8Cu12.5Ni10.0Be22.5 bulk metallic glass studied by XRD, SANS, and NMR.* Journal of Non-Crystalline Solids, 2003. **317**(1–2): p. 118-122.
79. Faupel, F., et al., *Diffusion in metallic glasses and supercooled melts.* Reviews of Modern Physics, 2003. **75**(1): p. 237-280.
80. Ehmler, H., et al., *Mass Dependence of Diffusion in a Supercooled Metallic Melt.* Physical Review Letters, 1998. **80**(22): p. 4919-4922.
81. N. Yodoshi, R.Y., A. Kawasaki and R. Watanabe, *Consolidation of [(Fe0:5Co0:5)0:75Si0:05B0:2]96Nb4 metallic glassy powder by SPS method.* Materials Transactions, 2009. **50**(9): p. 2264-2269.

82. Tiwari, D., B. Basu, and K. Biswas, *Simulation of thermal and electric field evolution during spark plasma sintering.* Ceramics International, 2009. **35**(2): p. 699-708.
83. Vanmeensel, K., et al., *Modelling of the temperature distribution during field assisted sintering.* Acta Materialia, 2005. **53**(16): p. 4379-4388.
84. Yucheng, W. and F. Zhengyi, *Study of temperature field in spark plasma sintering.* Materials Science and Engineering: B, 2002. **90**(1–2): p. 34-37.
85. Maizza, G., et al., *Relation between microstructure, properties and spark plasma sintering (SPS) parameters of pure ultrafine WC powder.* Science and Technology of Advanced Materials, 2007. **8**(7–8): p. 644-654.
86. Carroll, K.G., et al., *A New Iron Boro-carbide.* Nature, 1954. **174**(4438): p. 978-979.
87. Singh, A., et al., *Nanocrystallization in spark plasma sintered Fe48Cr15Mo14Y2C15B6 bulk amorphous alloy.* Journal of Applied Physics, 2013. **114**(5): p. -.
88. Ha, H. and J. Payer, *Devitrification of Fe-Based Amorphous Metal SAM 1651: A Structural and Compositional Study.* Metallurgical and Materials Transactions A, 2009. **40**(11): p. 2519-2529.
89. Zhang, Z., et al., *Structural evolution and property changes in Nd[sub 60]Al[sub 10]Fe[sub 20]Co[sub 10] bulk metallic glass during crystallization.* Applied Physics Letters, 2002. **81**(23): p. 4371-4373.
90. Shamimi Nouri, A., Y. Liu, and J.J. Lewandowski, *Effects of Thermal Exposure and Test Temperature on Structure Evolution and Hardness/Viscosity of an Iron-Based Metallic Glass.* Metallurgical and Materials Transactions A, 2009. **40**(6): p. 1314-1323.
91. Antonowicz, J., et al., *Small-angle X-ray scattering from phase-separating amorphous metallic alloys undergoing nanocrystallization.* Journal of Alloys and Compounds, 2009. **483**(1–2): p. 116-119.
92. Ashtekar, S., et al., *Direct Visualization of Two-State Dynamics on Metallic Glass Surfaces Well Below Tg.* The Journal of Physical Chemistry Letters, 2010. **1**(13): p. 1941-1945.
93. Bruna, P., et al., *Phase-field modelling of microstructural evolution in primary crystallization.* Journal of Alloys and Compounds, 2009. **483**(1–2): p. 645-649.
94. Imhoff, S.D., et al., *Kinetic transition in the growth of Al nanocrystals in Al-Sm alloys.* Journal of Applied Physics, 2012. **111**(6): p. 063525.
95. Manika, I. and J. Maniks, *Size effects in micro- and nanoscale indentation.* Acta Materialia, 2006. **54**(8): p. 2049-2056.
96. Nix, W.D. and H. Gao, *Indentation size effects in crystalline materials: A law for strain gradient plasticity.* Journal of the Mechanics and Physics of Solids, 1998. **46**(3): p. 411-425.
97. Jang, J.-i., et al., *Indentation size effect in bulk metallic glass.* Scripta Materialia, 2011. **64**(8): p. 753-756.
98. Dahotre, N.B. and S.P. Harimkar, *Laser Fabrication and Machining of Materials*. 2008, Boston, MA: Springer Science + Business Media, LLC.

99. Gleiter, H., *Our thoughts are ours, their ends none of our own: Are there ways to synthesize materials beyond the limitations of today?* Acta Materialia, 2008. **56**(19): p. 5875-5893.
100. Slipenyuk, A. and J. Eckert, *Correlation between enthalpy change and free volume reduction during structural relaxation of Zr55Cu30Al10Ni5 metallic glass.* Scripta Materialia, 2004. **50**(1): p. 39-44.
101. Singh, A., et al., *Structural Relaxation and Nanocrystallization-Induced Laser Surface Hardening of Fe-Based Bulk Amorphous Alloys.* JOM, 2014. **66**(6): p. 1080-1087.
102. Yavari, A.R., et al., *Excess free volume in metallic glasses measured by X-ray diffraction.* Acta Materialia, 2005. **53**(6): p. 1611-1619.
103. Murali, P. and U. Ramamurty, *Embrittlement of a bulk metallic glass due to sub-Tg annealing.* Acta Materialia, 2005. **53**(5): p. 1467-1478.
104. Chou, H.S., et al., *Structural relaxation and nanoindentation response in Zr–Cu–Ti amorphous thin films.* Applied Physics Letters, 2008. **93**(19): p. -.
105. Spaepen, F., *A microscopic mechanism for steady state inhomogeneous flow in metallic glasses.* Acta Metallurgica, 1977. **25**(4): p. 407-415.
106. Roberts, G.A., J.C. Hamaker, and A.R. Johnson, *Tool Steels*. 1971: American Society for Metals.

VITA

Ashish Kumar Singh

Candidate for the Degree of

Doctor of Philosophy

Thesis: DENSIFICATION BEHAVIOR, NANOCRYSTALLIZATION, AND MECHANICAL PROPERTIES OF SPARK PLASMA SINTERED Fe-BASED BULK AMORPHOUS ALLOYS

Major Field: Mechanical and Aerospace Engineering

Biographical:

Education:

Completed the requirements for the Doctor of Philosophy/Education in Mechanical and Aerospace Engineering at Oklahoma State University, Stillwater, Oklahoma in July, 2014.

Completed the requirements for the Master of Science in Mechanical and Aerospace Engineering at Oklahoma State University, Stillwater, Oklahoma in July, 2010.

Completed the requirements for the Bachelor of Science in Mechanical Engineering at Osmania University, Hyderabad, Andhra Pradesh, India, 2007 .

Experience: Currently working as Metallurgist at Welspun Pipes Inc., Little Rock, AR.

Professional Memberships: TMS, ACERS, AWS,